TRABECULAR BONE STRUCTURE AND CELLULAR MORPHOLOGY IN THE PRIMATE CRANIOFACIAL SKELETON

A Dissertation

by

LESLIE CLAIRE PRYOR

Submitted to the Office of Graduate and Professional Studies of
Texas A&M University
in partial fulfillment of the requirements for the degree of

DOCTOR OF PHILOSOPHY

Chair of Committee,	Paul C. Dechow
Committee Members,	Jian Q. Feng
	Elias Kontigiorgos
	Lynne A. Opperman
	Emet Schneiderman
	David Strait
Head of Department,	Paul C. Dechow

August 2015

Major Subject: Biomedical Sciences

ABSTRACT

The primate craniofacial skeleton is complex and highly variable across species. Assessing the variation of gross bone morphometry and orientation and cell microstructure in the low strain browridge and the high strain zygoma between species can aid in our understanding of craniofacial adaptation and evolution. In this study, μCT was used to characterize the trabecular bone morphology and primary trabecular orientation in the browridge of 8 humans, 5 *Pan*, 7 *Cebus*, 4 *Papio*, and 1 *Gorilla* and the zygoma of 10 humans and 5 *Pan*. Orientation of trabeculae in each region were compared to primary strain orientations in browridge and zygoma trabecular regions of 4 *Pan* finite element cranial models. Three dimensional images of the osteocytic network within high strain (anterior zygomatic root) and low strain (supraorbit) cortical regions of human and chimpanzee bone study were created using FITC staining and confocal microscopy. Quantification of osteonal osteocyte cell body shape and was carried out using Imaris Software. It was hypothesized that trabecular orientation and morphometry would be reflective of strain patters observed in *Pan* finite element models during premolar and molar biting. The results found that trabecular bone in the supraorbital browridge does not lie along primary strain orientations, but instead is composed of dense, sagittally oriented plates, that may serve to protect the eyes and brain from facial assaults. Trabecular bone morphometry in the body of the zygoma was orthotropic and primarily oriented in a medio-lateral direction, demonstrating a more predictable pattern of trabecular bone morphometry, anisotropy, and orientation. It was predicted that

osteocytes in the supraorbital regions of both species will be significantly more oblate, spherically shaped, and smaller with shorter, thicker dendritic processes relative to osteocytes in the zygoma. Imaris analysis of osteocyte shape in the anterior root of the zygoma and the supraorbit found that human osteocytes in the supraorbit are significantly less oblate and spherical than those in the robust *Pan* supraorbital region and osteocytes in the *Pan* supraorbit are significantly more oblate than osteocytes in the *Pan* zygoma. In addition to offering a mechanistic explanation for systemic differences between humans and *Pan*, these results provide a mechanism of bone adaption that is consistent with studies that show that the low strained supraorbital region demonstrates greater sensitivity to changes in orofacial function.

DEDICATION

I dedicate this work to my darling daughter Rita, who is my greatest accomplishment.

ACKNOWLEDGEMENTS

I thank my committee chair, Dr. Paul C. Dechow for all of the mentorship he provided me during this project and in my career. Throughout the time I have known him, from becoming his research technician to his mentee as both a master's and Ph.D. student, Paul has afforded me many opportunities that in addition to building my career, built my confidence as a student, scientist and teacher. I have also thoroughly enjoyed being mentored by someone with his collegiality, curiosity, knowledge, and passion in the field of bone biology and biomechanics. To my committee member, Dr. Lynne Opperman, thank you for the guidance and feedback you have given me in this project and throughout my time at Baylor College of Dentistry. I appreciate the expertise of my committee member, Dr. Jian Feng in bone cellular biology and the hard work of many people in his lab, especially Ying Liu and Dr. Yinshi Ren, which inspired the third part of this project. I feel this will make a novel contribution to the field of biological anthropology. I thank Dr. Emet Schneiderman for his guidance in the biostatistical analysis of this project and also in the gross anatomy lab. Thank you Dr. Elias Kontigiorgos, who was once a fellow graduate student in Paul's lab with me and is now my committee member. In addition to his friendship, he has given helpful advice regarding the use of the microCT.

This project began when I was working as a research technician for the NSF HOMINID grant (NSF BCS 0725141). I thank the many individuals that I had the opportunity to work with on this project, particularly my committee member Dr. David

Strait, and his two graduate students, Amanda Smith and Justin Ledogar. I would also like to thank the other PIs on this grant: Dr. Qian Wang, Dr. Callum Ross, Dr. Ian Grosse, Dr. Craig Byron, and Dr. Stephano Benazzi. All of these individuals have contributed to the development of this project through engaging discussions, by sharing their research, and by providing feedback on my manuscripts. Dr. Strait, Amanda Smith and Justin Ledogar helped more particularly in the construction and use of the *Pan* finite element analysis, from which I obtained the strain tensor results I used in chapters two and three of this work. I appreciate Dr. Tim Ryan and Dr. Richard Ketcham, who have given me expert council on trabecular bone morphological analysis. Dr. Shelley Smith was the committee chair of my master's thesis and I thank her for her thorough guidance during the formative stages of this project.

The *Pan tryglodytes* specimens were provided by the Southwest National Primate Research Center (supported by NIH-NCRR grant P51 RR013986) and the Yerkes National Primate Research Center at Emory University in Atlanta, Georgia (supported by NIH Base Grant RR00165). I acknowledge the Wild Animal Park Planckendael (Muizen, Belgium) and the Royal Zoological Society of Antwerp for providing the bonobo specimen. Thank you to Dr. Francis Vercammen and Maj Deckx for aiding in the transport of the bonobo specimen.

Lastly, I appreciate the steadfast support of my entire family: in particular, my father and stepmother, mother and stepfather, and brother who have always encouraged me and believed in me, and my three year old daughter, Rita, for giving up time with her mommy. I thank my Aunt Becky for always being so enthusiastically supportive of me.

I am grateful for all of my fellow graduate students at Baylor College of Dentistry, most especially Drs. Poorva Gharpure, Maria Serrano, Monica Prasad-Gibson, and Isra Ibrahim, and Ms. Katrina Mills for giving me support through camaraderie. I thank Andrew McIntosh, almost PhD, for his support in the final weeks.

TABLE OF CONTENTS

Page

ABSTRACT ii

DEDICATION iv

ACKNOWLEDGEMENTS v

TABLE OF CONTENTS viii

LIST OF FIGURES xi

LIST OF TABLES xiii

CHAPTER I INTRODUCTION 1

Primate Craniofacial Biomechanics 2
Cortical and Trabecular Bone Biomechanics 6
The Mechanostat 11
The Central Role of the Osteocyte in Bone Remodeling 12
Bone Structure and Physiology 13
cAMP/PKA and Wnt/β-catenin 17
DMP-1 and FGF23 18
RANKL and Osteoclast Formation 21
Mechanism of Osteocyte Mechanosensitivity 22
Osteocyte Morphology 23
Conclusion 25
Conclusion 26

CHAPTER II INTERNAL BONE ARCHITECTURE IN THE SUPRAORBITAL REGION OF FIVE PRIMATES. 28

Synopsis 28
Introduction 29
Materials and Methods 33
Volumes of Interest 34
Segmentation 36
MicroCT Analysis 36
Statistical Analysis 38
FEA of the *Pan* Browridge 38

Page

Results....39
µCT Visualization of the Primate Browridge....39
Whole Bone Analysis....40
Trabecular Bone Analysis....41
FEA of the Internal Browridge of *Pan*....45
Discussion....46
Summary of Results....46
Interspecific Trabecular Differences....48
Intraspecific Trabecular Differences....51
The Biomechanical Significance of the Primate Browridge....56
Limitations....65

CHAPTER III INTERNAL BONE ARCHITECTURE IN THE ZYGOMA OF HUMAN AND *PAN*....67

Synopsis....67
Introduction....67
Materials and Methods....71
Volumes of Interest....71
Trabecular Bone....72
Segmentation....72
MicroCT Analysis....73
Statistical Analysis....73
FEA of the *Pan* Zygoma....74
Results....74
MicroCT Visualization....74
Whole Bone Analysis....76
Trabecular Bone Analysis....76
FEA of the Internal *Pan* Zygoma....78
Discussion....79
Summary of Results....79
Inter and Intraspecific Differences in Trabecular Morphometry....82
Material Orientation and Strain....83
Limitations.....86

CHAPTER IV OSTEOCYTE MORPHOLOGY IN HIGH AND LOW STRAIN REGIONS OF THE HUMAN AND *PAN* CRANIOFACIAL SKELETON....88

Synopsis....88
Introduction....89
Materials and Methods....92
Three Dimensional Analysis of Osteocytes....93

Page

Results....94
MicroCT Analysis....94
Imaris Analysis of Cell Bodies....95
Imaris Analysis of Dendrites....97
Discussion....98
Summary of Results....98
Function of the Supraorbit and Zygoma....99
Conclusion....101

CHAPTER V SUMMARY....103

REFERENCES....108

APPENDIX A FIGURES....131

APPENDIX B TABLES....159

LIST OF FIGURES

Page

Figure 1-1 Interspecific strain in *Pan*. 131

Figure 1-2 The relationship between stress and strain 132

Figure 1-3 The central role of the osteocyte in bone remodeling. 133

Figure 1-4 Three-dimensional analysis of osteocytes. 134

Figure 2-1 Subregions of supraorbital analysis 135

Figure 2-2 Trabecular region of interest in the human and *Pan* browridge. 136

Figure 2-3 µCT renderings of whole extracted browridges. 137

Figure 2-4 µCT renderings of *Cebus* browridges. 138

Figure 2-5 Mean BVF, mean apparent density, and mean material density. 139

Figure 2-6 µCT renderings of browridge trabecular sub-volumes. 140

Figure 2-7 Mean BVF and structure model index. 141

Figure 2-8 Correlation matrix of browridge morphometry. 142

Figure 2-9 Supraorbital degree of anisotropy. 143

Figure 2-10 Trabecular orientation in the browridge. 144

Figure 2-11 Primary and secondary supraorbital strain tensors. 145

Figure 2-12 Superior view of supraorbital strain vectors. 146

Figure 3-1 µCT rendering of human zygomatic regions of analysis. 147

Figure 3-2 Rectangular sub-regions of zygomatic trabecular bone; transverse sections of µCT scans. 148

Figure 3-3 Degree of anisotropy in the zygoma. 149

Figure 3-4 Trabecular orientation in the human zygoma. 150

Figure 3-5 Strain tensors in the zygoma. 151

Figure 4-1 Confocal images of human osteocytes 152

Figure 4-2 Confocal images of *Pan* osteocytes 153

Figure 4-3 Confocal images of *Pan* osteocytes demonstrating periosteal fibers. 154

Figure 4-4 Osteocyte cell body surface area and volume. 155

Figure 4-5 Osteocyte degree of sphericity. 156

Figure 4-6 Human confocal images alongside cell body and dendrite renderings 157

Figure 4-7 *Pan* confocal images alongside cell body and dendrite renderings 158

LIST OF TABLES

Page

Table 2.1 Species, body mass, and trabecular VOI in the browridge.....159

Table 2.2 Bone volume fraction, apparent and material density of whole supraorbital bone regions.....160

Table 2.3 Interspecific differences in density 161

Table 2.4 Trabecular bone morphometry of postorbit and browridge regions.....162

Table 2.5 Trabecular bone morphometry of postorbit and browridge subregions 163

Table 2.6 Interspecific differences of supraorbital trabecular bone morphology 164

Table 2.7 Intraspecific differences of supraorbital trabecular bone morphometry 165

Table 2.8 Mean angle orientation of supraorbital primary eigenvectors 166

Table 2.9 Mean angle orientation of supraorbital secondary eigenvectors.....167

Table 2.10 Mean angle orientation of supraorbital tertiary eigenvectors..... 168

Table 2.11 Mean angle orientation of supraorbital superoinferior eigenvectors.....169

Table 2.12 Mean angle orientation of supraorbital anteroposterior eigenvectors.....170

Table 2.13 Mean angle orientation of supraorbital mediolateral eigenvectors.....171

Table 2.14 Trabecular bone morphometry across the post-cranial skeleton.....172

Table 3.1 Species, body mass, and trabecular VOI in the zygoma 173

Table 3.2 Bone volume fraction, apparent density, and material density of the upper zygoma 174

Table 3.3 Trabecular bone morphometry of upper and lower zygoma regions 175

Table 3.4 Interspecific differences of trabecular bone morphometry between *Homo* and *Pan* 176

Table 3.5 Intraspecific differences of trabecular bone morphometry between zygomatic regions 177

Table 3.6 Mean angle orientation of zygomatic primary eigenvectors.....178

Table 3.7 Mean angle orientation of zygomatic secondary eigenvectors.....179

Table 3.8 Mean angle orientation of zygomatic tertiary eigenvectors.....180

Table 4.1 Mean BVF, and apparent and material density of cortical bone of the supraorbital and zygomatic regions 181

Table 4.2 Mean osteocyte cell body shape and size.....182

Table 4.3 Mean dendrite surface area, length, volume, and diameter.....183

CHAPTER I

INTRODUCTION

There are many unanswered questions regarding the biomechanical nature of derived cranial features in hominin species. In recent literature, questions about the adaptational significance of the craniofacial morphology of *Australopithecus africanus* and *Paranthropus bosei* have been addressed through finite element analysis (FEA) (1,2). This technique models gross structure and incorporates material properties, such as elastic modulus, muscle fiber orientation, and masticatory or incisal loading to look at deformation patterns and draw conclusions about the adaptational significance of derived craniofacial features. Models are more accurate when they incorporate realistic values of cortical bone mechanical properties, which show species and location-specific differences in density, thickness, anisotropy, and elasticity (3-7). Currently, trabecular regions of primate craniofacial bone are modeled as solids with elastic properties obtained from trabecular bone within the human tibia (8). It is unknown to what extent the mechanical properties of subcortical or trabecular structure in primate craniofacial bone differ from post cranial regions and to what extent these differences may affect the outcome of FEA. The incorporation of more realistic values of mechanical properties data obtained from subcortical structure may improve the accuracy of finite element models, but these have yet to be described.

In addition, such descriptions may offer a unique insight into the bone remodeling process. Very little is known about the relationship between the structural hierarchies of bone tissue, such as how variation at the cellular level affects bone

remodeling mechanisms, and in turn gross morphological structure. The osteocyte, the most populated cell in bone, is likely the key player in mechanosensation and transduction of strain (9). Still, very little is known about how species and location-specific variation in osteocyte morphology is affected by local strain patterns and affects mechanosensation. Assessment of the osteocytic network within primate craniofacial bone will aid in formulating the right questions regarding the relationship of osteocytic organization, behavior, and the mechanosensory mechanisms that affect the region as well as species-specific differences in the remodeling response. Furthermore, the characterization of the osteocytic network may lead to a better understanding of how the degree of phenotypic plasticity underlying the remodeling response varies across species and craniofacial locations.

Primate Craniofacial Biomechanics

Finite element analysis (FEA), is a valuable method employed by functional morphologists to explore the relationship between bone form and function in extant and extinct animal species in regions that are highly complex in shape, such as the craniofacial skeleton (1). In this process, a geometric computer model of the structure representing the animal's gross morphology is created from a computed tomography scan of a specimen, and can be converted to a mesh, or a structure made of a finite number of smaller elements (such as triangles), which are connected by nodes. After mesh creation, values which can be obtained from in vivo or vitro experimentation, such as Poisson's Ratio and elastic modulus, muscle force, are incorporated into the model (1). The model is constrained at certain points representing real-life constraints. For

example, a craniofacial model is constrained at the foramen magnum and the temporomandibular joint. Once an analysis is run on the finite element model, the results are validated using in vivo or in vitro strain gage analysis. This method has been used to explore the adaptational significance of the often confounding variation observed in the cranial morphology among various primates, and particularly in the family *Hominidae* (7,8,10-12).

One of the most challenging aspects of this method is defining appropriate material properties of the mesh elements that represent bone (1). Bone is not isotropic, material properties vary from region to region, and different bones have macro and microstructural variations that are not easily quantified. Using accurate regional orthotropic mechanical property data derived from cortical bone studies yields more accurate results (7). Trabecular bone is typically modeled as a continuum, or cellular solid. This means that the material properties across the region are averaged to produce a single value that represents the whole structure. In the models created by Strait et al. (8), trabecular bone within the supraorbital and postorbital regions, and the zygomatic body and arch are modeled as solid regions using isotropic elastic properties that differ from the surrounding cortical bone. These values (E=637 GPa, v=0.28) are obtained from a study by Ashman (13) that determined the elastic properties for trabecular bone in the human tibia. Heterogeneity of the elastic properties of trabecular bone, especially in craniofacial regions has not been studied. However, it has been suggested that this averaging is problematic at cortical and trabecular bone interfaces and where there are large stress gradients (15). Given the large variation in trabecular bone structure across

the primate skeleton, the impact that trabecular bone variation by location and species might have on whole bone responses to orofacial function is unknown.

A finite element model of *Macaca fascicularis* created by Ross et al. (16) shows that during mastication, masseter muscle forces induce bending and twisting of the zygomatic arch around an antero-posterior axis, applying infero-laterally directed tension on the lateral region of the inner orbital wall, the infraorbital plate, and the anterior arch. Tension applied to the lateral inner orbital wall causes it to straighten, creating compressive forces along the superior surface of the browridge and tensile forces on the inferior surface. Comparisons between these deformations and strain data collected by Endo (17) suggests that *Homo* and *Gorilla* undergo a similar pattern of deformation as the macaque crania (16). Furthermore, the anterior root of the zygomatic arch of *Macaca fascicularis*, which sits medial to the masseter muscle and superior to the tooth row, is subjected to high compressive and tensile forces, which would create high shear strain, likely making the structure of this region a significant feeding adaptation. In the macaque model, chewing side did not have a significant effect on strain magnitude and orientation. This suggests that in the supraorbital and zygomatic regions the primary source of strain originates from muscle forces, not bite forces. The macaque FEM predicted that the postorbital bar endures a greater magnitude of strain relative to the browridge during orofacial function (16).

Recently finite element analysis was employed to look at the effects of intraspecific variation across 6 *Pan* crania that fell along extremes of a structural principle components analysis, finding that while magnitude of strain varies greatly

intraspecifically, strain patterns are fairly consistent across morphological extremes (Figure 1-1) (18). Looking at interspecific variation found among the 6 *Pan* crania, *Paranthropus boisei (OH 5) and Australopithecus africanus* (STS 5) showed that strain pattern differs between species(19). Furthermore, this study showed that the robust craniofacial skeleton of *P. boisei* is structurally strong and capable of producing high bite force, lending support to the hypothesis that many of the derived hominin craniofacial features were adaptations to hard object feeding and changes in diet caused by an extreme shift of available vegetation in the Early Pleistocene.

The extensive variation observed in extant and extinct primate craniofacial forms have primarily been attributed to biomechanical, or orofacial (incisal and masticatory) function (1). However, both spatial and biomechanical models have been used to explain variation in supraorbital robusticity. The robust or projecting browridge observed in living apes and Pleistocene *Homo* is hypothesized to be a product of sphenoid length, an adaptation to protect the face and brain from external forces, or is a systemic consequence of overall facial robusticity (20-23). Ravosa (24) found that the main determinate of browridge morphology is facial size and that browridge antero-posterior length is strongly correlated with neuro-orbital disjunction, while supero-inferior length is related to masticatory muscle size and craniofacial torsion during mastication. Most of these explanations however, do not provide a mechanism behind browridge development. The masticatory stress hypothesis posits that browridge robusticity is an adaptation to counter large bending stresses induced by anterior tooth loading. This hypothesis does attempt to provide a mechanism driving browridge form,

but has been weakened by strain gage experimentation performed by Hylander and colleagues (25-29). These experiments show that the supraorbital region experiences significantly less strain compared to the zygoma and zygomatic arch. Relatively low strain implies that the browridge is "overbuilt" relative to other craniofacial regions.

Cortical and Trabecular Bone Biomechanics

The formation and remodeling of bone is highly dependent on epigenetic, hormonal, and mechanical stimuli (30,31). Throughout growth and adulthood, bones are subjected to forces such as compression, tension, torsion, and shear. Compression occurs when there is a negative change in the dimension of the object. Conversely, an object under tension undergoes a positive change in dimension. Torsion occurs when an object is twisted around an axis, and a shear force is one in which parallel forces are imposed on the object in opposite directions. Stress is defined as force per unit area, or

$$\sigma = \text{Force/Area}$$

and results in strain (ε): a measure of deformation.

$$\varepsilon = \text{change in length/ length}$$

$$\text{shear } \varepsilon = \text{change in angle}$$

Poisson's ratio is defined as the ratio between strain perpendicular to the direction of applied load to the strain in the direction of the applied load (31,32).

The slope of the relationship between stress and strain before permanent deformation or failure is defined as the material's stiffness or elasticity (Figure 1-2). Under tension and compression, a material's stiffness is called its elastic modulus while under shear loading it is described as the shear modulus. In elastic solids, shear and elastic modulus are measured in pascals (Pa). The area under the plastic region of the stress-strain curve provides a measure of the toughness of the material and is represented in units of work energy per unit volume (reviewed by 31,reviewed by 32). Standard methods used for obtaining the mechanical properties of trabecular bone include uniaxial tensile testing, bending tests, ultrasonic techniques, and micro and nano-indentation methods (reviewed by 33).

Degree of anisotropy of cortical bone is the ratio of the greatest elastic modulus to the least elastic modulus in a direction orthogonal to it (anisotropy increases as the value moves away from one). In trabecular bone, anisotropy is a ratio of orientation in the direction in which the trabeculae are most oriented to that in which they are least oriented (anisotropy increases as the value exceeds one). Bone is most often transversely isotropic at a tissue level of organization, in that elastic moduli or directional prominence is equal or similar in two orthogonal directions and different in a third orthogonal direction. However, bone can also be orthotropic, differing in elastic modulus in all three orthogonal directions, or can have a structure that cannot be easily modeled as orthotropic (reviewed by 31,reviewed by 32).

Studies by Dechow et al. (1993), Schwartz-Dabney and Dechow (2003), Peterson and Dechow (2002, 2003b), Peterson et al. (Peterson et al., 2006), and Wang et al.

(2006b) characterize the variation in material properties of primate craniofacial cortical bone, showing that such properties vary significantly by region and species and these differences are often easily relatable to differences in function. These studies employ wet weight, dry weight and thickness measurements, and ultrasonic wave techniques to determine the density and material properties such as elastic modulus and Poisson's ratio of specific craniofacial sites.

Mechanical and material properties of cortical bone obtained from the human supraorbital region and the buccal mandibular bone differ significantly from one another (Dechow et al., 1992; Dechow et al., 1993). Mandibular bone is stiffer than supraorbital bone, supporting the hypothesis that the elastic properties of cortical bone vary in function by region. Determination of the material properties of the outer and inner tables of human parietal bone found higher densities in the outer table, and significant differences in anisotropy between regions. In the human craniofacial region, nine out of thirty-six locations sampled within the parietal, frontal, temporal, occipital, and zygomatic bones possessed significant mean directions of maximum stiffness (4). Five of the nine locations with significant orientations are muscle attachment sites. They include one on the zygomatic arch, one between the temporal line and the sagittal suture of the temporal bone, and three on the parietal bone. At the site of the masseter muscle attachment on the zygomatic process of the zygomatic bone, Peterson and Dechow (4) observed the greatest anisotropy and a significant mean direction of stiffness across individuals in the sample group. Studies of cortical bone have demonstrated that orofacial function has an effect on the material properties of cortical bone in the

supraorbital region (34). Edentulous individuals were found to have similar or greater values of density in the frontal bone, greater values of density in the zygomatic region, and lower density in the maxillary region compared to dentate individuals. The elastic and shear moduli, which varied significantly by region, indicate that there is significant complexity in bone remodeling by region (Dechow et al., 2010). A particularly interesting finding from this study is that the low strain supraorbital region is responsive to changes in orofacial function.

Wang and Dechow (35) found significant differences cortical elastic properties between comparable locations in rhesus and human crania. Furthermore, cortical density, thickness, shear and elastic moduli, and anisotropy vary by primate species such that patterns of density, thickness, shear and elastic moduli, and anisotropy are more similar in closely related species *Papio* and *Macaca*, which differ from the pattern observed in human crania (6).

Trabecular bone elastic modulus in postcranial human and bovine bone ranges from 0.76 to 20 GPa (reviewed by 33). Bone mineral density (BMD), or material density, and apparent density are reliable estimators of trabecular bone stiffness and strength (36-38), but this relationship is site dependent and prediction error can increase by as much as 60% if site is ignored (38,39). Anisotropy of trabecular bone also has a significant influence on overall bone strength, and differences in trabecular orientation affect the behavior of bone under differing stress conditions.

There are many studies that look at the structure of trabecular bone in primate species to determine the significance of derived features in the post cranial skeleton and

many studies which investigate the complex properties behind bone development and remodeling that analyze trabecular bone structure in wild type and transgenic lab animals such as mice or sheep. The most popular method for assessing trabecular bone structure is through micro-computed tomography scanning and analysis. A trabecular structural analysis method pioneered by Feldkamp and colleagues (40), microcomputed tomography has many advantages over other methods (40: 3,41). Most importantly, it is non-destructive and allows for visualization and testing of trabecular bone as a three-dimensional structure (38,42,43). In this technique, high resolution x-ray tomographic scans are reconstructed and mathematical methods are used to calculate various structural properties such as average trabecular thickness, separation, material and apparent densities, degree of anisotropy, and primary angle of orientation.

Studies of trabecular bone using μCT in primate post-cranial regions have demonstrated the complexity of the relationship between trabecular bone structure and function. *Galago* and *Perodicticus* femoral head specimens displayed no significant differences in femoral head trabecular BVF (both around 0.51), but did possess significant differences in femoral neck BVF (averaging 0.247 and 0.449, respectively). Degree of anisotropy differed significantly in both regions averaging 1.364 (*Galago*) and 1.228 (*Perodicticus*) in the femoral head and 1.746 (*Galago*) and 1.354 (*Perodicticus*) in the femoral neck (44). However, in a 2007 study on femoral neck trabecular structure in anthropoids, Fajardo and colleagues (45) found that neither DA nor BVF is significantly different between climbing/suspensory and quadrupedal species. Griffin et al. (46) found no significant difference in BVF between ape and human metarsal trabecular bone, but

did show that humans possess greater anisotropy in this region compared to other great apes, a possible consequence of bipedalism. Ryan and Ketcham (47) found that trabeculae in the femoral head of leaping primates are more strongly oriented (supero-anteriorly) and display different primary orientations compared to non-leaping primates.

The Mechanostat

Differences at the cellular level may help explain the inconsistency between regional variations in strain magnitude observed in the primate craniofacial skeleton. The bone remodeling response can be described as a "mechanostat," in which bone mass is determined through a mechanical feedback system that has a minimum effective strain (MES) required to initiate bone remodeling (48). If strain goes above the MES, bone formation is initiated and if it goes below the MES, then bone loss occurs. Furthermore, the minimum effective strain (MES), which is regulated by hormones, signaling factors and differences in cellular or lacunar morphology, may vary regionally and by species. Frost (48) suggested that, during normal activity, most vertebrate bone remodels to maintain strain levels between 100 and 1500 microstrain. The typical range of peak strains for vertebrate long bones during vigorous activity is between 2000 and 3000 microstrain (31,49).

In addition to differences in MES, bone remodeling sensitivity is affected by the temporal sequence of bone loading during the individual's development. The theory of cellular accommodation proposes that bone cells react strongly to initial changes in mechanical environment, yet the reaction slows down or stops once the cells accommodate to change (50). This mechanism has been observed in trabecular bone and

in rat tibia where there is a greater bone remodeling response to an initially large mechanical load which trails off compared to an initially small load which grows in magnitude (51,52). Kupczik et al. (10) showed that strains are not high enough in the supraorbital region of the crab-eating macaque bone modeling or remodeling response that would explain the overbuilt browridge. However, the supraorbital region may adapt so rapidly that high strains are not observable: the highly strained zygoma undergoes very slow growth relative to the low strained browridge, which grows rather rapidly in development. There are other possible explanations for browridge development based on Frost's mechanostat (1987) and Turner's theory of cellular accommodation (50). MES is site and age dependent and could be lower in the supraorbital region as an adaptive response to maintain a certain amount of bone in the region for either orofacial function or other purposes, such as protection or support of the brain, eyes and musculature (16). The supraorbital region may have a lower threshold for strain than other high strain regions in the craniofacial complex in order to produce greater relative robusticity. High strain regions, such as the zygoma may have a greater threshold for strain because it withstands more frequent loading of a greater magnitude (10,50,51).

The Central Role of the Osteocyte in Bone Remodeling

Bone remodeling is the process by which physiological changes occur in bone tissue to repair damage due to stress induced micro-fractures, while simultaneously maintaining mineral homeostasis (53,54). It is accomplished through the strategic deposition and removal of bone tissue by osteoblasts and osteoclasts, respectively. Osteocytes play a major role in bone remodeling by activating Wnt/β-catenin and

cAMP/PKA pathways and expressing dentin matrix protein (DMP-1), FGF23, RANKL and various circulating factors, including prostaglandins and nitric oxide, both in response to mechanical loading that produces shear strains (Figure 1-2). Osteocyte morphology is both affected by the local strain environment and also affects the mechanosensitivity of the cell.

Bone Structure and Physiology

Mammalian bone (cortical and trabecular) is a dynamic tissue. Its formation and remodeling are highly coordinated with epigenetic hormonal and mechanical stimuli, which occur during development and adulthood (55).

At the microscopic level, bone consists of a mixture of collagen, calcium phosphate, water, polysaccharides, proteins, cells, and blood vessels. Collagen is composed of fibrous proteins. It forms a variety of connective tissues and it undergoes mineralization in vertebrate animals to form the skeletal system. In bone formation, type 1 collagen consists of fibrils arranged both randomly, as in woven bone, or in sheets, as in lamellar bone. Fibrils are composed of microfibrils, or structures made from the stacking of triple helices of tropocollagen proteins linked by hydrogen bonds. The length of the polypeptides that make up tropocollagen, along with its particular molecular composition of amino acids (which prevent rotation) and nitrogen (which prevents hydrogen bonding) allow it to maintain its flexibility as a molecule. After formation, the collagen may eventually undergo mineralization, in which minuscule crystal structures formed of calcium phosphate embed within it. The bonding mechanism and organization

of the mineral component and collagen fibers of bone is not fully understood, however, cellular activity is likely responsible (reviewed by 30,reviewed by 31).

The microstructural organization of bone varies among vertebrate species, and by age and location. Three basic types of primary bone are found in mammals: woven, parallel-fibered bone, and lamellar bone. Woven bone forms quickly and is disorganized; in humans, it is found in infants and children and is used in the bone fracture healing process. Lamellar bone forms slowly and is more organized. This type of bone characterizes the outer layer of a bone shaft, for example.

The macrostructure of bone is often categorized into two different types: cortical and trabecular. Cortical bone is relatively dense bone that houses vasculature (Haversian systems), resorption cavities, canaliculi, and lacunae that contain osteocytes. Trabecular bone is consists of larger, visible openings, and is found branching off of cortical bone into marrow filled cavities. Both cortical and trabecular bone in young mammals is made up of woven bone, but in older mammals trabecular bone can be made of primary lamellar bone, or carved out of secondary bone. In trabecular bone, lamellae run perpendicular or oblique to its struts. This creates jagged surfaces that can be observed through magnification. Trabecular bone consists of plates and rods. Rods are cylindrical struts of around 0.1 mm in diameter and 1.0 mm in length that typically form right angles in connection to other struts (30,56). Plates are sheet-like and organized together in a parallel fashion. While the gross structure of bone is separated into primarily two types of bone, cortical and trabecular, in many locations of the vertebrate skeleton bone type is not very easily classified, such as the craniofacial skeleton. The variation in gross

bone morphology may be better understood by looking at variations in cellular activity and even cellular morphology.

There are four main types of living cells found in bone and these, directly or indirectly are responsible for the building up and breaking down of bone. During bone modeling Haversian bone is formed from lamellar bone when osteoblasts and osteoclasts work together to build osteons: highly organized structures that consist of a large canal surrounded by concentric layering of lamellae connected by smaller canals. Osteons are connected to one another by Volkmann's canals. Haversian canals, which are found at the center of each osteon, and Volkmans's canals encase vascular networks within cortical bone, enclosing nerves and vessels and allowing for circulation of nutrients. The process of Haversian bone remodeling begins primarily with two types of cells, osteoblasts and osteoclasts. Osteoblasts and osteoclasts are located only on bone surfaces. Osteoclasts form resorption cavities, which initiates Haversian remodeling. The osteoclast is a macrophage derived cell which functions by clinging to a ruffled surface and breaking up and filtering bone mineral through its multinucleated cell body (reviewed by 30,reviewed by 31).

After the osteoclast has removed bone, osteoblasts may migrate to the region to lay down new osteoid on the surface of the bone. As they do so they are pushed away from the surface. Each osteoblast produces osteoid at a different interval. When an osteoblast ceases to produce osteoid, it will no longer be able to perform protein synthesis; it will flatten out, and subsequently become embedded in the bony matrix. Current conventional wisdom of the bone modeling and remodeling process holds that

osteoblasts are primarily responsible for the subsequent mineralization of osteoid. Once embedded, osteoblasts undergo a transformation, and turn into osteocytes. Osteocytes maintain contact with the surface of bone and with other embedded osteocytes via cells processes. When the surrounding osteoid mineralizes, these projections, along with a thin layer surrounding the osteocyte, resist mineralization, and are preserved in the form of canaliculi and lacunae, respectively. Osteoblasts can also mature to become bone lining cells, which are present on all bone surfaces, except for regions of osteoblastic and osteoclastic activity. Conventionally it is believed that bone lining cells form from osteoblasts when they are no longer producing osteoid (when the amount of bone present is determined adequate) and they form a thin layer of quiescent cells along the out layer of bone. Cell processes from these cells remain in contact with embedded osteocytes. As would be suspected, osteocytes and bone-lining cells make up the majority of bone cells (reviewed by 30,reviewed by 31).

While there is still a lot of mystery surrounding the mechanisms behind bone remodeling, recent attention to mechanisms guiding osteocyte formation and function has moved the field by tremendous strides. We now understand that osteocytes function in bone remodeling, activating cAMP/PKA and indirectly Wnt/β-catenin pathways by releasing prostaglandin2 in response to mechanical stress and that Wnt/ β-catenin pathway controls osteoclast differentiation and osteoblast and osteocyte apoptosis. We also know that dentin matrix protein (DMP-1) is crucial to the differentiation of osteocytes from osteoblasts and the proper mineralization of the ECM, and that it regulates FGF23 levels to control phosphate homeostasis. Receptor activator for nuclear

factor kB ligand RANKL is highly expressed by osteocytes and is positively related to the maturation of osteoclasts from hematopoietic precursor cells.

cAMP/PKA and Wnt/β-catenin

It has been shown that a mechanical load (in the form of shear strain) promotes the release of prostaglandin E2 (PGE2). An increase in PGE2 stimulates an increase Cx43 expression causing the formation of hemichannels, which increase gap junction communication between osteocytes (57). Elevated levels of PGE2 cause EP2 levels rise triggering the cAMP/PKA pathway, which leads to inhibition of the phosphorylation of β-catenin. β-catenin can then collect in the cytoplasm and can cross the nuclear membrane to activate the transcription of various genes (9,58). It is also proposed that mechanical load triggers the expression of the genes DKK1 and SOST, perhaps enabling cross talk between Wnt/ β-catenin and cAMP/PKA pathways.

Wnts are glycoproteins that attain an active form after undergoing post-translational modification with the addition of the lipid, palmitate. The canonical Wnt pathway and the one that is most relevant to bone remodeling, is also known as the Wnt/β-catenin pathway. It is one of four known Wnt pathways. There are 10 known Wnt proteins that are capable of acting through the four pathways. The Wnt/β-catenin pathway is activated when the corresponding Wnt protein binds to a co-receptor made of either Lrp5 or Lrp6 (low density lipo-protein) and a frizzled family protein. The binding of Wnt to the co-receptor leads to the phosphorylation of Dishevelled (Dsh), which in turn leads to the phosphorylation of GSK-3β, or Glycogen Synthase Kinase-3β. Inhibition of the phosphorylation of β-catenin, resulting from that of GSK-3β, and

allows it to accumulate and enter the nucleus of the cell, regulating the transcription of genes that are important for cell differentiation, apoptosis, proliferation, and bone function (58).

Studies have shown that canonical Wnt/β-catenin signaling induces osteoblastogenesis and controls osteoclast differentiation, as well as bone homeostasis (59-61). These studies found that mice with osteoblast deleted β-catenin showed an increase in osteoclastic activity due to a decrease in osteoprotegerin, or OPG (discussed below), resulting in lowered bone mass. The precise mechanistic origin of this defect could not be isolated, as osteocytes are derived from osteoblasts. However, Wnt/β-catenin is activated in osteocytes under mechanical loading, suggesting that the pathway is important in bone remodeling through its function in the osteocyte (reviewed by 58).

Kramer (62) produced osteocyte specific β-catenin deficient mice in order to understand the importance of Wnt/β-catenin signaling, independent of osteoblasts. They found that this pathway is specifically crucial in osteocytes, as the resulting phenotype resembled the osteoblast-specific β-catenin knockouts and was attributed to a decrease in OPG and an increase in osteoclastic activity.

DMP-1 and FGF23

The gene for DMP-1 is located near others in the SIBLING family, at 4q21 in humans and 5q21 in mice (63,64). While DMP-1 is expressed in multiple soft tissues (brain, kidney, and pancreas) and dentin, its role in bone is central to this review (65,66). DMP-1 is a non-collagenous protein found in the extracellular matrix of bone and is part of the Small Integrin-Binding Ligand, N-Linked Glycoprotein, or SIBLING, family (66).

The full length version of the protein is found in two cleaved forms within the extracellular matrix of bone (a 37kDa N terminal fragment) and dentin (57kDa C terminal fragment) (67) . Lu and colleagues (68) determined that it is the 57-kDa C-terminal fragment of DMP-1 that is responsible for maintaining phosphate homeostasis and that it aids in osteocyte maturation. In bone, it has been shown to regulate phosphate homeostasis through its effect on the level of fibroblast growth factor 23 (FGF23). As a component of the ECM of bone, it is believed to play a crucial role in mineralization (reviewed by 69).

Using whole-mount X-gal staining of DMP-1 lacZ knock-in mouse embryos and pups, Feng et al. (70) demonstrated that DMP-1 is expressed during both embryonic development, primarily in osteoblasts, and postnatally, primarily in osteocytes. More specifically, DMP-1 expression is found to be highly concentrated in the dendritic processes of osteocytes in 8 day old mouse pups. In order to gain a greater understanding of the role of DMP-1 in bone mineralization and homeostasis, Feng et al. (71), assessed the expression of FGF23, a transcription factor that regulates phosphate homeostasis, in DMP-1 null mice to determine the association between mineralization defects and renal phosphate wasting. They also treated DMP-1 mice with a high phosphate diet to rescue the DMP-1 null phenotype. DMP-1 null mice had elevated levels of FGF23, rickets and osteomalacia (71,72). DMP-1 null mice on a high phosphate diet showed some improvement in osteomalacia, mineralization, and the rate of bone formation. Abnormal osteocyte morphology was also observed in these mice (Figure 1) with a lack of mineralization surrounding osteocytes as well as defective dendritic morphology and

lacuna-canalicular systems. Feng et al. (71) demonstrated the importance of DMP-1 in the process of osteoblast maturation and differentiation into osteocytes by its down-regulation of osteoblasts markers. Both the changes in FGF23 serum levels and osteocyte morphology indicate a causal relationship between DMP-1 and the severe rickets-like bone defects, severe hypophosphatamea, and mild hypocalcemea observed in these mice. Collectively, the results indicate that DMP-1affects bone mineralization directly (by inducing osteocyte maturation and function) and indirectly (via phosphate homeostasis, or the renal excretion of phosphate through its effects on FGF23 levels).

Zhang et al. (73) further explored the mechanisms behind the effects of DMP-1 on bone remodeling, finding that the abnormalities in bone remodeling observed in DMP-1 null mice result from a decrease in receptor activator of nuclear factor-kB ligand, or RANKL expression relative to OPG. This decrease caused a decrease in osteoclast number. Furthermore, they demonstrated that phosphate plays a critical role in many bone remodeling processes surrounding the osteoblast function, including the formation of secondary ossification centers, the maturation of long bone growth plates, the mineralization of the ECM and osteoblasts differentiation into osteocytes. Based on their findings, they produced a working hypothesis that pieces together the interaction between phosphate, DMP-1 and osteocytes (Figure 2). The hypothesis proposes that as osteoblasts are embedded in osteoid, DMP-1 and phosphate encourage the mineralization of the osteoid and the maturation of the newly formed osteocyte. However, defects in the osteocyte maturation process, as is observed in DMP-1 null mice cause serum FGF23 to increase, leading to a decrease in phosphate. The process

then becomes cyclical as a decrease in phosphate will have an inhibitory effect on the maturation of embedded osteocytes. Gluhak-Heinrich et al. (74) demonstrated an increase in DMP-1 in osteocytes, resulting from an increase in mechanical loading, a result that is consistent with Zhang et al.'s (2011) findings and hypothesis. Given the central role osteocytes play in what Bonucci (9) terms "the bone orchestra," if DMP-1 is responsible for osteocyte formation, bone mineralization, FGF23 expression and phosphate homeostasis, and osteoclast recruitment, it follows logically that DMP-1 levels are influenced by mechanical loading.

RANKL and Osteoclast Formation

As described above, osteoclasts are derived from hematopoietic cells. Receptor activator of nuclear factor-kB ligand, or RANKL, is a membrane bound factor that is known to encourage osteoclasts differentiation, or osteoclastogenesis by direct cell to cell contact with pre-osteoblastic stromal cells (75,76). There is also a soluble version of RANKL, termed sRANKL. While Hikita et al. (77) showed that osteoblasts do secrete the soluble form of RANKL, they found that the membrane form was much more efficient at inducing osteoclastogenesis. In the process of osteoclastogenesis, RANKL binds to the RANKL receptor, RANK, on the surface of the osteoclast precursor cell. Osteoprotegerin, or OPG, is a decoy receptor that will bind to RANK (the RANKL receptor) to inhibit this process.

By looking at the response of osteocyte-like MLO-Y4 cells to mechanical stimulation, You et al. (78) found that mechanical loading effected osteoclast differentiation via cell to cell contact. While mechanical loading of MLO-Y4 cells

caused a decrease in sRANKL, it is unclear whether the osteocytes can induce osteoclastogenesis through the more likely mechanism of cell to cell contact via the RANKL. Furthermore, the mechanically stimulated osteocyte-like cells were shown to release more OPG, decreasing the RANKL to OPG ratio, further inciting a hindrance to osteoclastogenesis.

More recently, Nakashima et al. (2011) found that purified osteocytes produce a significant amount more RANKL than osteoblasts and stromal cells, and are more likely to be the primary source of osteoclastogenesis inducing membrane bound RANKL, a hypothesis consistent with the observation that a decrease in DMP-1 affects levels of RANKL. They, along with others propose that osteocytes maintain contact with osteoclasts precursors for cell to cell interactions via their long dendritic processes, which extend throughout and beyond the bony matrix into marrow spaces where these cells are found.

Mechanism of Osteocyte Mechanosensitivity

Frost (48) proposed that bone mass is determined through a mechanical feedback system which is regulated by hormones and biochemical agents. Strain gage studies suggest that bone remodels to optimize its performance relative to strain. It is its structural organization that is theorized to play a primary role in the cellular mechanosensory mechanisms of bone tissue. In the lacuno-canalicular network and bone remodeling theory, the positioning of osteocytes within lacunae embedded in the mineral matrix, which are connected by canaliculi, allows for a strain dependent communication system between bone cells. It is hypothesized that strain derived canalicular flow of fluid

(consisting of wastes and nutrients) stimulates osteocytes, triggering the production of anabolic factors. These anabolic factors, including prostaglandins and nitric oxide (NO), act as messengers in the bone remodeling process. They either travel via the lacuno-canalicular route, or by gap junctions in intracellular transport (or both), to reach the periosteum or bone marrow to signal to the bone lining cells to produce osteoblasts. The relationship between bone remodeling and basal level activity and under stimulation of bone tissue can also be explained using the lacuno-canalicular network and bone remodeling theory (LCT). Under physiologically "normal" strain conditions, nutrients and waste continue to circulate, and osteocytes are maintained. However, if strain levels fall below the MES, vital circulation of nutrients and wastes decreases, osteocytes are starved and may undergo apoptosis (79).

Osteocyte Morphology

Osteocyte morphology varies based on anatomical location and bone type. Osteocyte shape, orientation, surface area, and volume; and dendritic process number, surface area and volume differs significantly by anatomical location, and likely function (80-82). For example, in mice, calvarial osteocytes are more spherical, while fibular osteocytes are more oblong and aligned along orientations of primary strain throughout the entire fibula (Figure 1-4). This observation is consistent with what might be expected as the calvarial region of the skeleton is subjected to very little loading relative to the tibia. Furthermore, the more spherical morphology of murine calvarial osteocytes suggests that they are more sensitive to strain than are the elongated fibular osteocytes; it could be that osteocyte shape is one mechanism by which regions can adjust their

minimum effective strain level (82). Calvarial osteocytes have lower surface area and volume compared to fibular osteocytes. The greater surface area and volume that characterizes fibular osteocytes is possibly related to their metabolic activity: larger cells accommodate larger organelles that are responsible for many bone metabolic processes (80). Murine fibular osteocyte dendritic processes are more numerous, but smaller in width, relative to calvarial osteocytes.

Within 6 weeks of development, embryonic murine femoral osteocytes change from being randomly oriented and irregularly shaped to becoming aligned with the major axis of strain orientation within the bone (longitudinally). Osteocytes from femora that developed without mechanical loading maintained random orientation and were more spherical in shape, contrasting with the flatter more spindle shaped osteocytes in murine femora that experienced normal loading conditions. This finding further supports the hypothesis that osteocyte morphology is reflective of mechanical loading history. Cortical and cancellous bone morphology are both affected by mechanical loading. However, each experience differences in the extent of network formation with regard to orientation, nuclear shape and branch formation. The number of osteocyte cell processes in cancellous bone is not affected by mechanical loading. However, the elongation of cell processes, which is encouraged by mechanical loading was less extreme for trabecular bone than for cortical (81). Osteocyte morphology may also be affected by pathologies. For example, osteocytes in osteopenic bone are relatively large and round, in osteoarthritic bone are large and elongated, and in ostepetrotic bone are small and discoid.

While there have been many encouraging findings regarding the morphological variation in osteocytes and dendrite formation, many more studies that describe variations in osteocyte and dendrite morphology across various species and in different pathologies are needed to gain a complete picture of the function of osteocyte.

Conclusion

Taken together, recent discoveries regarding the mechanisms behind osteoblast, osteocyte, and osteoclast formation, as well as phosphate homeostasis provide strong support for the centrality of the osteocyte in bone remodeling. Kramer (2010) determined that the Wnt/β-catenin pathway is crucial to proper osteocytic function, controlling not only osteoblasts differentiation, but also OPG levels and osteoclastic activity. DMP-1 has both direct and indirect effects on bone remodeling and mineralization. It affects bone mineralization directly, by inducing osteocyte maturation, and indirectly by regulating phosphate homeostasis through its effects on FGF23 levels (71). Furthermore, DMP-1 null mice abnormalities in bone remodeling result from a decrease in the ratio of RANKL to OPG, which causes a decrease in osteoclasts (73). Additionally, Nakashima et al. (2011) showed that osteocytes produce membrane bound RANKL and are likely to be the primary source of osteoclastogenesis. Although it is not clear how cell to cell contact is achieved between embedded osteocytes and osteoclasts, it is suggested that osteocytes maintain contact with osteoclasts precursors through dendritic contact.

There are many gaps in our understanding behind these mechanisms, such as the process by which β-catenin activates genes within the nucleus of the osteocyte, whether

SIBLING proteins communicate with one another, and how DMP-1 regulates FGF23 (58,69). Tremendous progress has been made in recent decades in understanding how the osteocyte is central to the bone remodeling process, both via strain detection and signaling to other bone cells and through maintaining mineral homeostasis of the ECM.

Furthermore, studies that explore variations in osteocyte shape and organization and dendrite thickness have found significant differences across anatomical locations and within various pathologies. While this area of exploration is not yet robust, it holds great promise for understanding the functional significance of the osteocyte in bone modeling and remodeling. The future of the osteocyte's leading role in bone remodeling is highly promising and there is no doubt that research in this area will continue to flourish and lead to exciting new discoveries about the mechanistic workings of the bone tissue.

Conclusion

Interpreting the functional significance of variation among both extant and extinct primate craniofacial morphology has proven challenging for many reasons. A great deal of interspecific and intraspecific structural variation exists in the craniofacial skeleton of primates. FEA is a useful method for testing hypothesis about the adaptational significance of overall shape as well as isolated derived traits. Addressing particular gaps in our knowledge of macroscopic variation of trabecular bone structure in the craniofacial region may help strengthen these studies as well as help test hypotheses about the significance of more confounding structural adaptations, such as the robust browridge. The following work aims to quantify the variation in trabecular structure

(including bone volume fraction, material density, trabecular thickness, number and separation, connectivity density, structure model index, degree of anisotropy and trabecular orientation) in the low strain supraorbital region of *Homo, Pan, Gorilla, Papio,* and *Cebus* and the high strain zygomatic region of *Homo* and *Pan* using microcomputed tomography. Primary orientation of trabecular bone will be compared to primary strain tensors in the supraorbital and zygomatic regions of 4 *Pan* finite element models undergoing premolar three and molar one bite force.

Because much of the interspecific variation observed may be systemic, interpreting the significance of gross morphologies at the macroscopic level require a deeper look at the cellular mechanisms behind systemic and individual differences. In order to understand the mechanistic principles behind the observed variation, the third aim of this project is to characterize the shape and size of bone mechanosensory cells, or osteocytes, as well as the volume of their dendritic processes across *Homo* and *Pan* using confocal microscopy and Imaris software.

CHAPTER II

INTERNAL BONE ARCHITECTURE IN THE SUPRAORBITAL REGION OF FIVE PRIMATES

Synopsis

Inconsistencies in primate browridge robusticity and relative strain magnitudes across the craniofacial skeleton have led to many quandaries regarding the functional significance of the browridge. Assessing the variation of trabecular bone morphometry and orientation in the browridge across regions and species can aid in our understanding of craniofacial adaptation. Also, quantifying species and region specific variation may serve to improve the accuracy of finite element models. In this study, μCT was used to characterize the trabecular bone morphology and primary trabecular orientation in the browridge of 8 humans, 5 *Pan*, 7 *Cebus,* 4 *Papio*, and 1 *Gorilla*. Orientation of trabeculae were compared to primary strain orientations in the browridge trabecular regions of 4 *Pan* finite element cranial models.

Our findings suggest that trabecular bone morphometry differs in the supraorbital region relative to postcranial regions, but trabecular bone characteristics maintain similar species-specific relationships to those in the postcranial skeleton. Furthermore, our results suggest that the dense sagittally oriented plates of trabecular bone found within the supraorbital region may be more reflective of an adaptation to protect the face and brain case from assaults, although patterns of trabecular orientation and anisotropy do not rule out the possibility that orofacial function has an effect on browridge morphology.

Introduction

The browridge is a prominent structure in primate and hominin craniofacial skeletons. Its structural variation throughout the course of human evolution is remarkable. (Weidenrich, 1943; Wolpoff, 1995). This variation has been explained as functional adaption to mastication, allometry, and social behavior (24,83,84). Strain gage experimentation supports the hypothesis that the browridge of apes, humans and hominin species is overbuilt for solely resisting the forces of mastication (10,28). However, a study by Dechow et al. (2010) found that browridge cortical density is significantly greater and thickness is significantly lower in edentulous humans, suggesting that this region does adapt to altered function. Material differences in supraorbital cortical bone in these individuals suggest that although there is low deformation or strain in the region during orofacial function, the region might be more sensitive to strain, or have a lower minimum effect strain, than other areas of the craniofacial skeleton (10,48,50). While studies of primate craniofacial cortical bone have shown regional and species-specific variation, very little is known about subcortical or trabecular structure in primate craniofacial regions (3-6).

Trabecular bone strength and stiffness, which contribute to whole bone strength, are highly dependent on apparent density and fabric anisotropy (85-90). The density of trabecular bone, as a component of total bone mass, is important in the assessment of aging or menopause related osteopenia and osteoporosis. A recent study on fossil and modern human samples by Chirchir et al. (91)reveals that trabecular bone density in hominins has remained stable for several million years before decreasing significantly in

recent modern humans, a possible consequence of increasing sedentism. Strain gage experimentation has supported the observation that trabecular orientation in post-cranial bones is significantly correlated with principle tensile and compressive strain orientations. In addition, greater trabecular density is found in regions that experience greater stress (85,89,90,92), indicating that both trabecular bone and cortical bone are subject to functional adaptations. Thus the structure of trabecular bone at both organ and tissue levels carries important yet little understood developmental and functional significance.

In recent years, a number of studies have used micro-computed tomography to characterize trabecular bone architecture in order to investigate its relationship with bone function in the primate post-cranial skeleton (45,46,93-103) and mandible (104-107). Quantifying the structural characteristics (for example, bone volume fraction and trabecular thickness) and orientation of trabecular bone in the primate craniofacial skeleton is essential for building our understanding of the relationship between regional responses to varying loading patterns and the role of tissue adaptation in shaping the supraorbital region.

Additionally, knowledge of the extent of region and species-specific variations in subcortical bone in craniofacial regions may help improve the outcomes of finite element modeling of the primate craniofacial skeleton. Finite element (FE) analysis of the primate craniofacial skeleton has been conducted on models of human, chimpanzee and macaque crania as well as fossil crania including *Australopithecus africanus, Paranthropus bosei,* and *Australopithecus sediba* to test hypotheses regarding the

evolution of various craniofacial features (1,2,8,10,11,16,18,19,108-113). If the trabecular bone were modeled with structural detail, the complexity of the model would be beyond that which can be solved with most available computers. Therefore, trabecular bone is typically modeled as a continuum, or cellular solid, in which the material properties across the region are averaged throughout the whole structure.

In most primate craniofacial FE models, trabecular bone within orbital and zygomatic regions are modeled as solid regions using isotropic elastic properties (E=637 MPa, v=0.28) obtained from trabecular bone within the human tibia (8,13). Strait et al. (7) showed that the precision of FE modeling and analysis is improved by the incorporation of region-specific orthotropic elastic properties of cortical bone (Strait et al. 2005). In light of the potential significant contributions of trabecular bone in bone strength and health, the possibility of variation in trabecular structure cannot simply be ignored in studies of craniofacial skeletal function. Currently there are no data on variation in material properties of trabecular bone in this region at any level that are available for incorporation into FE models of primate craniofacial structures. This study serves as an initial step towards obtaining mechanical properties of trabecular bone in the craniofacial regions of primates. It is necessary to characterize the morphology, variability, and primary orientation of trabeculae in order to efficiently and properly test its mechanical properties.

The objective of this study is to describe the density of whole supraorbital regions (including both cortical and trabecular bone) and trabecular (subcortical) bone architecture and fabric anisotropy in the supraorbital region of humans and select

primates using micro-computed tomography. Micro-CT analysis provides structural descriptions, such as the average separation between and thickness of individual trabeculae, the degree of orientation of trabeculae (degree of anisotropy or DA), and the bone volume fraction (BVF) of trabecular bone. Variations in trabecular bone architecture parameters such as BVF, trabecular separation, number, thickness, and DA are compared, as well as primary orientations of trabeculae in orthogonal planes. Strain orientation and magnitude along the surface of the supraorbital region has been described previously, but there is no data on strain orientations and magnitudes within the internal body of the supraorbital region (16). In this paper we describe internal strain orientations and relative magnitudes in the supraorbital region of four *Pan* FE models of molar and premolar biting (18). These observations are compared to our findings of trabecular orientation eigenvectors and relative densities across the supraorbital region in humans, *Pan*, *Papio*, and *Cebus*. We hypothesize that if supraorbital morphology is sensitive to mastication, then trabeculae should be oriented along the primary strain orientations in these models and density patterns across the supraorbit should mirror relative strain magnitudes.

Furthermore, we expect to find species-specific differences in trabecular bone structure similar to those found in primate femoral and humeral head specimens, where absolute values of BVF, trabecular thickness and trabecular separation will be greater in larger species, and trabecular number, connectivity density and bone volume to bone surface volume will be greater in smaller species (114). This finding will add to the discussion of allometric relationships of trabecular bone properties and give insight into

how the adaptational behavior of trabecular bone may differ across anatomically and phylogentically.

Materials and Methods

The study sample, including humans, *Pan,* and *Gorilla,* were selected to observe what kind of differences exist between apes and humans and therefore to see what type of differences may exist among fossil hominids. Two additional species served as outgroups: an old world species of monkey, *Papio,* and a new world species of monkey, *Cebus*. Both have been subject to morphofunctional studies, the former in the study of chewing behavior and bone elastic properties (6,115) the latter used as a model for studying fallback feeding in hominid evolution (116), and in *in vivo* strain measurements as well (117). . Bony supraorbital regions, extending from the lateral orbit to the glabellar region, were extracted from 8 human, 5 *Pan,* 7 *Cebus,* 4 *Papio,* and 1 *Gorilla* cadavers using a Stryker bone saw (for larger specimens) and a Dremel tool (for smaller samples) and stored in equal amounts of isotonic saline and 95% ethanol. The humans came from the willed body program at the University of Texas Southwestern Medical Center (2 females, 6 males, mean age ± SD: 54.4 ± 19.63). All *Papio* (*hamadryas anubis*) specimens came from the Southwest National Primate Research Center and included 2 adult males and 2 adult females. The *Gorilla* (1 adult female) came from the Chicago Zoo. *Pan* specimens included 4 *tryglodytes* (2 adult females and 2 adult males), which came from Southwest National Primate Center, and one adult female *paniscus,* which came from the Antwerp Zoo. *Cebus* specimens (2 *apella* males, *2 albifrons* males, 2 *albifrons* females, and 1 male of an unknown species)

were captive animals from Dr. Callum Ross' Laboratory in the Department of Organismal Biology and Anatomy at the University of Chicago.

Once extracted from their respective crania, all specimens were scanned at Baylor College of Dentistry in Dallas, Texas using a Scanco Medical µCT 35 (Scanco Medical, Basserdorf, Switzerland) at a resolution of 37 µm, an energy of 70 kVp, and an angulation of 114 µA, with an integration time of 400 milliseconds. Specimens were scanned in a vertical orientation and scanned in the saline ethanol mixture described above.

Volumes of Interest

Medio-Lateral Boundaries

Moving medio-laterally across the supraorbital region, 5 volumes were analyzed: a post orbital (PO) region, a browridge region (BR), and 3 regions within the browridge (Figure 2-1). The PO region extended from temporal surface (where the orbital ridge begins to separate from the frontal bone) to the zygomatico-frontal suture. In specimens lacking the zygomatico-frontal suture, a point was estimated based on the gross morphology of the specimen and by comparing to other specimens from the same species. The BR region (extending mediolaterally from the supraorbital notch or foramen to the temporal surface or termination of the brain case) was divided equally (based on total width) into medial (Me), middle (Mi) and lateral (La) ridge regions. In specimens lacking a notch or foramen, a point was chosen similar to specimens of the other species.

Antero-Posterior and Supero-Inferior Boundaries

In humans and *Cebus*, supraorbital regions were shorter (less protruded) relative to *Pan*, *Gorilla*, and *Papio*. Additionally, the browridges of humans and *Cebus* are oriented in a supero-inferior direction, whereas those in the apes and *Papio* are oriented in a more antero-posterior direction. In specimens with greater posterior extension, it was difficult to determine a common anatomical marker for demarcating regions of interest in the posterior of the bone (where trabeculae morph into the diploe of the skull) due to the extreme variation in supraorbital morphology between the species. In all species, the ridge served as the anterior point of termination. In humans and *Cebus*, regions were terminated infero-posteriorly (where the orbital plate branches off) by a plane running along the cranial base. Regions in these species where terminated superiorly by a point along the cranial cavity wall that hits the plane perpendicular to the plane of the cranial base. In species (*Pan*, *Gorilla*, *Papio*) with highly projecting ridges, regions were terminated posteriorly at the point midway over the orbit. Analysis of the whole bone (cortical and trabecular) and trabecular only regions were performed (Figure 2-2).

Trabecular Bone

All trabecular bone within the aforementioned boundaries was included in each volume of interest. Average body mass of each species is provided along with the average trabecular bone volume that was analyzed (Table 2.1). Regions of trabecular bone were first outlined, or contoured, by hand every 10^{th} slice (37 μm in width) and then an analysis function was applied to morph the contour on slices between each hand

drawn contour. After morphing the contour around the general region of trabecular bone, an automatic contouring function was used to more systematically specify each trabecular region. By allowing the user to set an inner and outer (inside the contour and outside the contour) value of mg of HA per cubic centimeter, the function uses the existing contour and the specified inner and outer values to approximate a new contour. The specified inner and outer values aided in excluding most of the voxels along the endochondral surface of the cortical bone, while including the greatest area of trabecular structure. The same inner and outer value was used for each specimen. These contours were then visually inspected for accuracy.

Segmentation

Once volumes of interest were contoured, a threshold was used to extract the mineralized bone phase. The threshold was determined for each specimen separately using the iteration method defined by Riddler and Calvard (118) and Trussel (96,119,120). This algorithm is provided as an image processing language (IPL) script by Scanco Medical.

MicroCT Analysis

Whole bone regions (including cortical and trabecular bone) were analyzed for bone volume fraction (BVF) and material and apparent density only. Bone volume fraction is a ratio of bone to total volume and is determined by the marching cubes method (121). Apparent and material densities are determined by measuring the grey values within the region of interest, which correspond to pre-calibrated grey levels of bone density. Apparent density is a measure of the mg of hydroxy apatite per cubic

centimeter that include bone material and voids. The material density is a measure of the mg of hydroxy apatite per cubic centimeter of the bone material excluding all voids, or non-bone material. A μCT technician at Baylor College of Dentistry conducts weekly scans using a phantom specimen to make sure the calibration is accurate. However, we have found density values calculated from μCT to be an underestimate of actual density; it should be noted that densities obtained in this study are more meaningful for relative sample comparisons (122).

After trabecular bone volumes were contoured and the threshold applied, a pre-written IPL script (Scanco Medical software) was applied to contoured trabecular regions to determine degree of anisotropy, using the mean intercept length method (123,124); structure model index by triangulation (97,125); trabecular separation, thickness, and number using the distance transformation method (97,125); connectivity density, using the Euler method (126); and bone volume fraction (BVF). Some have shown that it is best to use a spherical volume of interest when measuring anisotropy (127). However, the method used by the Scanco Medical μCT 35 system to calculate DA does not use test lines, but instead projects every triangle of the triangulated surface, making problems related to sampling error (128) and model based calculations used by others (127) irrelevant. Additionally, defining a region of interest produces artificial edges of individual trabeculae, but these edges are suppressed by Scanco Medical's bone morphometric script in the calculation for surface dependent parameters so that the shape of the region of interest does not affect the results (43).

Statistical Analysis

Mann-Whitney U tests were conducted with SPSS on resulting values to determine significant differences by region within each species and Wilcoxon sign test were used to test intraspecific differences between postorbital and browridge sub-regions for both whole bone and trabecular bone analysis. To determine the type of anisotropy, magnitudes for all three eigenvectors were tested for correlation. Primary, secondary and tertiary eigenvectors (H2, H3, and H1, respectively) were plotted relative to supero-inferior, antero-posterior, and medio-lateral anatomical axes using Origin Lab Pro. Mean angle and standard deviation was calculated for each eigenvector from each axis. Raleigh's test for uniformity was performed on each mean angle measurement to determine significance and Watson Williams F test for multiple comparisons was used to detect intra and interspecific differences between angles. All circular statistics were calculated using the software Oriana. Because eigenvectors tended to fall near or along primary anatomical axes, they were then grouped by their nearness to anatomical axes, providing supero-inferior, antero-posterior, and medio-lateral vectors. These anatomically grouped vector's mean angle and standard deviations were compared as described above, to test for correlation using regression analysis, and for uniformity using Raleigh's Test and compared across species and location using the Watson Williams F test. Differences were determined significant at $p \leq 0.05$.

FEA of the **Pan** *Browridge*

In order to obtain a better understanding of the internal strain patterns in the browridge during orofacial function, this study describes primary, secondary, and

tertiary strain tensors in supraorbital trabecular bone regions of 4 chimpanzee cranial FE models that were constructed in another study to determine intraspecific strain variations (18). The FE models, which represent morphological extremes of a CT collection of 19 cranial *Pan* specimens, were modeled using region-specific values of cortical bone properties and muscle force for the anterior temporalis, deep and superficial heads of the masseter and the medial pterygoid; these values were obtained from other *Pan* specimens. Crania were constrained at the TMJ and the foramen magnum. Trabecular regions were contoured as solid separate masses (or objects) and isotropic mechanical property values obtained from trabecular bone of the human tibia were applied to these objects (13). Once the FE analysis is run for both premolar 3 and molar 2 bite points, the cortical bone can be removed to show strain in trabecular objects alone. Voxels can be removed along the surface of the object to look along the internal aspect of the trabecular body as well. See Smith et al. (18) for more details regarding the construction of these models. Primary, secondary and tertiary strain orientations and relative magnitudes from these FE models are described in the results below, and are discussed relative to our findings for trabecular orientations and density.

Results

μCT Visualization of the Primate Browridge

Figure 2-3 shows a rendering of a supraorbital bone from each species and a cut plane demonstrating the extent of trabecular bone in the region. Figure 2-4 demonstrates the variability among the extent of trabecular bone in the *Cebus* browridge. The *Gorilla*

supraorbital region was analyzed as a whole region, but the subcortical bone was too dense for a trabecular bone analysis.

Whole Bone Analysis

Whole bone (including trabecular and cortical bone) analysis reveals some inter and intraspecific differences in all measures of density, including BVF (ratio of bone volume to total volume), apparent density (density of the bone material and voids) and material density (density of only bone material) (Tables 2.2 and 2.3). *Cebus* has a significantly greater BVF in the PO region compared to *Homo* and *Papio* ($p=0.046$ and $p=0.014$, respectively). Apparent density is also significantly higher in the PO region of *Cebus* relative to *Homo* and *Papio* ($p=0.027$ and $p=0.011$, respectively) and significantly lower in the BR compared to *Pan* ($p=0.013$). *Cebus* also has significantly less bone in the BR region compared to *Papio* ($p=0.042$). Also in the BR region, humans and *Cebus* have significantly less bone (characterized by BVF) than *Pan* (for both $p=0.003$). However, BVF is not significantly different in the postorbital region between humans and *Pan*, *Gorilla* and *Papio.* Material density differs significantly in *Papio*, where both PO and BR bone material is less dense than in humans ($p=0.017$, and $p=0.042$) and the postorbital region bone material is less dense than *Cebus* ($p=0.017$). The gorilla has a greater BVF across the entire supraorbital bone than all other species, a greater apparent density than all species except *Pan*, but a lower material density than all species; these differences were not determined to be significant by the Mann-Whitney U tests (Figure 2-5). The highest material density is observed in *Cebus* in both regions, which was also not determined significant by the Mann-Whitney testing (Figure 2-5).

In sum, *Cebus* has more bone of greater mineral density than *Papio* in the postorbital region, but less bone of greater mineral density in the BR. Humans have greater mineral density than *Papio* across the entire supraorbital region, and *Pan* has more bone in the BR than both *Homo* and *Cebus*.

All species except for *Papio*, display denser postorbital regions relative to BR regions. The only intraspecific differences found are between the PO and BR regions of *Homo* and *Cebus* in both BVF and apparent density (Table 2.3). Both human and *Cebus* PO regions have more bone within the volume of analysis (BVF at $p=0.036$, and $p=0.012$) and are denser overall (apparent density at $p=0.036$ and $p=0.012$) than the BRs in these species. Material density is consistent across regions in all species (Figure 2-5).

Trabecular Bone Analysis

Interspecific Comparisons of All Trabecular Bone Structural Characteristics

Figure 2-6 shows cubic renderings from random regions of trabecular bone from the BR showing the variability across species and between individuals. Means and standard deviations for all trabecular bone parameters are reported for all species and locations in Table 2.4 and 2.5, with the postorbital values duplicated for comparison among the whole BR region and sub-regions. Mann-Whitney U tests revealed significant differences in all trabecular bone descriptive variables and significant differences in at least one variable in pairwise comparisons of all species (Table 2.6). BVF of trabecular bone ranged from 0.11 (in the *Cebus* postorbit) to 0.87(in the *Pan* lateral ridge). BVF of PO and BR regions is significantly greater in *Pan* relative to *Homo, Papio,* and *Cebus* (Figure 2-7 and Table 2.5). The only other interspecific significant difference in BVF is

found between the BR of *Homo* and *Papio* (p=0.016), such that *Papio* have denser trabecular bone in BR regions. Degree of anisotropy (DA) ranged from 1.26 (*Homo* medial ridge) to 3.89 (*Papio* middle ridge). The BR region of *Pan* is significantly more oriented (higher DA) than the BR of both *Homo* and *Cebus* (p=0.045 and p=0.008 respectively). The PO region in *Papio* is significantly less oriented than the PO region in *Homo* (p=0.004). The type of trabecular bone (plate-like vs rod like vs concave) described by structure model index (SMI) is significantly different between the PO and BR regions of *Pan* relative to *Homo* (p=0.002 and p=0.006) and *Cebus* (p=0.003 and p=0.016) and the PO region of *Pan* relative to that of *Papio* (p=0.016). Trabecular structure in *Pan* is more concave (pores are concave and less connected) relative to *Homo* (p=0.002 and 0.006), *Cebus* (p=0.003 and p=0.016), and *Papio* (p=0.016 in the postorbit) and *Papio* is more concave and porous in structure relative to *Homo* (p=0.004, significant only in the postorbit) and *Cebus* (significant in both regions; p=0.003 and p=0.032). Human and *Cebus* trabeculae are relatively more plate-like (Figure 2-7). However, trabecular bone in the BR of *Cebus* is significantly more rod-like than that found in the BR of *Homo* (p=0.045).

Papio differs significantly from *Homo* in both regions in all of the remaining structural parameters including connectivity density, trabecular number, thickness, and separation. Notable differences are also seen in trabecular thickness between all species except *Papio* and *Cebus*. *Cebus* and *Papio* have the thinnest average trabeculae, followed by *Homo* and then *Pan* (see Table 2.5).

Figure 2-8 shows correlations between all parameters. BVF and SMI are the most strongly correlated variables in this sample, where Spearman's R^2 is 0.774 ($p \leq 0.001$).

Intraspecific Comparisons of Trabecular Bone Structural Characteristics

Intraspecific comparisons performed using Wilcoxon test revealed some significant differences between PO and BR sub-regions (La, Mi, and Me ridge) (Table 2.7). There is an increase in average BVF moving lateral to medial (from PO to BR) in humans and *Cebus*, but differences in BVF revealed by Wilcoxon tests are only significant between the PO region and the medial BR region in *Pan* (p=0.0043) and the PO and middle BR region of *Cebus* (p=0.043) (Table 2.7). DA tends to decrease from the PO region to the BR region in all species except *Papio*. *Homo* PO trabecular bone is significantly more oriented (higher DA) than La (p=0.012), Mi (p=0.012), and Me (p=0.012) regions and *Cebus* PO regions are significantly more oriented than La (p=0.028) and Mi (p=0.043) ridge regions (Table 2.7).

A measure of structure model index (SMI) shows that trabecular bone in all regions is closer to plate-like and concave/porous than rod-like (see Figure 2-7). SMI decreases moving lateral to medial (rod/plate-like to concave) in all species except for *Pan* (increase in SMI from very concave to less concave, closer to plate-like bone). The *Homo* postorbital region is characterized by significantly higher SMI relative to the medial ridge (p=0.036) and *Cebus* postorbital region has significantly higher SMI relative to the middle ridge (p=0.043) (Tables 2.5 and 2.6). The *Pan* PO trabecular bone has significantly lower SMI than both middle (p=0.043) and medial (p=0.043) BR regions (Tables 2.4 and 2.6).

Material Distribution and Angular Orientation

Comparison of eigenvector magnitudes suggests that trabecular bone in the supraorbital region is approximately transversely isotropic (See Figure 2-9). There is a strong correlation between the 2 largest vector magnitudes, H2 and H3, where R=0.976 and the mean ratio of H2 (largest vector) to H3 (the second largest vector, or secondary) is 1.209 (SD=±0.101). The correlation between both H2 and H3 with the smallest eigenvector, H1, are 0.760 and 0.0779, respectively. The mean ratio of H2 to H1 is 1.923 (SD =±0.570) and the mean ratio of H3 to H1 is 1.592 (SD=±0.453).

Both H2 (primary; Table 2.8) and H3 (secondary; Table 2.9) eigenvectors grouped primarily along anatomical axes, such that H2 was generally closer to the infero-superior anatomical axis and significantly uniform relative to this axis in orientation in all species and locations except in some regions of *Papio* and *Cebus* (see Table 2.8). H3 is significantly oriented and on average closer to the antero-posterior anatomical axis in all species except all *Papio* regions and 2 *Cebus* regions (see Table 2.9). The mean angle of the H1 (tertiary) vector was significantly oriented in all species in all regions against all axes (IS, AP, and ML) except for in the *Cebus* medial BR region against the AP and ML axes (Table 2.10). Figure 2-10 shows orientation of eigenvectors in the human browridge.

In all or most (4 or more) regions of 2 human individuals, most (3 or more) regions of 3 *Cebus* individuals, some (1 or 2) regions of 5 *Cebus* individuals, most (4) regions of one *Pan* individual and nearly half of the baboon (all regions of 2 individuals and 1 region of one individual) the primary eigenvector, H2, was closer to the antero-

posterior axis and H3 was closer to the infero-superior axis. When vectors were grouped by their relationship to anatomical axes, the correlation between the supero-inferior and antero-posterior vector is 0.884 with a mean ratio of 1.08 (SD=±0.199). The correlation between both SI vectors and AP vectors with the ML vector, H1, are 0.704 and 0.0767, respectively. The mean ratio of the SI vectors to the ML vectors is 1.834 (SD =±0.606) and the mean ratio of AP vectors to the ML vectors is 1.693 (SD=±0.488). Significance in uniformity increased when the vectors were grouped by anatomical axis *(*See Tables 2.11 and 2.12). For the H1 vector, only one adjustment was made to group vectors along their primary anatomical axes- the medial BR region in *Papio*, whose H3 (secondary) vector was around 10 degrees from the medio-lateral axis (See Table 2.13).

Watson Williams F Test for multi-wise comparisons found no significant intra or inter specific differences between primary, secondary and tertiary eigenvectors except for the relationship between H2 and the IS axis (p=0.018) and H3 and the AP axis (p=0.021) in only the middle BR region between species. There were no significant inter or intra specific differences between anatomically grouped vectors.

***FEA of the Internal Browridge of* Pan**

Differences in strain magnitude and orientation were not apparent between *Pan* crania or between PM3 and M2 biting. Differences were apparent between working and balancing sides. During biting, the internal layers of brow ridge trabecular bone appear to undergo tension in the inferolateral-superomedial direction on both resting and working sides. The secondary strain tensor, which describes compression, appears to be oriented in the inferomedial-superolateral direction on resting side, and the tertiary strain

vector, which also describes compression, is in the postero-anterior direction. However, along the body of the brow ridge and exclusive of the glabella and PO region of the working side, this secondary strain tensor appears to switch orientations with the tertiary strain tensor, being oriented primarily in the postero-anterior direction. Figure 2-11 shows primary and secondary strain in the post orbital and browridge regions on the working side. This pattern is consistent across the sample of chimps. Both primary and secondary tensors have a slight antero-posterior tilt (from inferior to superior) and the tertiary antero-posterior, or tertiary tensor has a slight infero-superior tilt. Tensor orientations on the resting side can be more easily visualized by imagining a "V" in the coronal plane, where both limbs sit at a 90 degree angle to one another. This "V" is slightly oriented backwards. The tension side of the "V" is always on the glabellar side, whereas the compression side is always lateral. The smaller compressive tensor is orthogonal to these, placing it in the antero-posterior direction, tilted upwards. On the working side, a similar pattern emerges except that the smaller of the compressive tensors makes up one limb of the "V" and the larger of the compressive forces lies in the antero-posterior direction (See Figure 2-12).

Discussion

Summary of Results

This study used μCT to characterize the whole bone density and trabecular bone morphometry and orientation in the supraorbital region of 5 primate species, including 8 humans, 5 *Pan*, 8 *Cebus*, 4 *Papio*, and 1 *Gorilla*. We hypothesized that if trabecular bone in the supraorbital region is sensitive to mastication, trabecular bone orientation

and relative density within the supraorbital region should be similar to strain orientations and relative strain magnitudes, respectively in the supraorbital trabecular regions of 4 FE models of chimpanzee crania during biting. Based on the relative strain magnitudes in the supraorbital region of the 4 FE models, more lateral (more uni-directionally and higher strained regions) should be denser (have higher BVF) and exhibit a higher degree of anisotropy. Our results were largely consistent with this hypothesis. In *Pan*, trabecular BVF was higher in more lateral regions, but this finding was only significant between the postorbital and middle regions. In humans, *Cebus* and *Papio*, mean BVF increased moving lateral to medial. Degree of anisotropy declined from lateral to medial in all species except *Papio*.

Five chimpanzee crania finite element models were used to predict the magnitude and orientation of strain in the BR during mastication. We expected to find that primary orientation of trabeculae in the BR would be biomechanically consistent with strain orientations observed in the models. Trabecular bone in the supraorbital region in all 4 species analyzed was found to be transversely anisotropic, consisting of relatively dense sagittally oriented plates (Figures 2-9 and 2-10), and did not fall along primary and secondary strain orientations in our chimp FEMs. While trabecular bone was not aligned along primary and secondary strain orientations, its alignment may be predicted by combining strains from working and balancing sides.

Additionally, we predicted that species-specific differences in trabecular bone structure would exist similar to those uncovered by Ryan and Shaw (114) in primate femoral and humeral head specimens: specifically, that BVF, trabecular thickness, and

separation would be absolutely greater in larger species and that trabecular number, connectivity density and BS/BV will be absolutely greater in smaller species. The results of this study found that the allometric relationships in the supraorbital region are consistent with those in postcranial regions in all except the *Gorilla* specimen.

Furthermore, finite element analysis is improved when realistic values for cortical bone stiffness are incorporated (7). These values have been determined for the regions across the craniofacial skeletons in *Papio*, *Homo*, *Macaca*, *Cebus*, and *Pan* (4,6,35). In these models, trabecular bone within the craniofacial skeleton, such as the supraorbital and zygomatic regions, are modeled as solid regions using isotropic elastic properties obtained from the human tibia (E=637 MPa, v=0.28) (13). The elastic modulus of trabecular bone is highly dependent on its structural characteristics, particularly the BVF, SMI, and DA (129-132). However, trabecular bone type can vary dramatically across subcranial regions and it is unknown the degree to which trabecular bone morphometry varies between craniofacial and postcranial regions as well as between different primate species (56,97). The findings of this study suggest that these regions do vary greatly in morphology across species and between some locations within the supraorbit and also are different than that of postcranial trabecular bone (See Table 2.14). Exploring and determining these differences would strengthen our ability to appraise the primate craniofacial skeleton both theoretically and experimentally.

Interspecific Trabecular Differences

Many studies that have attempted to link function of trabecular bone density and morphometric properties have been unsuccessful (103). For this reason, Ryan and Shaw

(103) took a holistic approach to interpreting trabecular bone morphometry by using discriminate function analysis to investigate the relationship among different trabecular bone structural characteristics in the primate femoral and humeral head. It was discovered that locomotor habits are more predictable when trabecular bone features are considered together. For example, the human femoral head differs from the femoral head of *Pan* due to a having a combination of relatively low number of thin, highly anisotropic plate-like trabeculae. Therefore, caution must be used when trying to interpret trabecular bone morphometric values in isolation. While trabecular bone adaptation cannot be reduced to simple differences in isolated trabecular bone variables, isolated features also correlate strongly with body size and to a small degree, phylogeny. Trabecular BVF, thickness, and separation increase with increasing body size, while trabecular number, connectivity density and bone surface area to bone volume decrease with an increase in body size. However, the increase in certain parameters, like trabecular thickness and separation, is not proportionate to the increase in body mass, giving the variable negative allometry. Ryan and Shaw (114) found that old world monkeys have relatively high numbers of trabeculae which are spaced relatively far apart. On the other hand, apes have by comparison very thin trabeculae, which are greater in number and clustered more tightly together in the case of *Pan*, which has relatively high BVF. *Pongo* and *Gorilla* have relatively low BVF, which the authors propose is due to higher trabecular spacing.

There appeared to be no measureable trabecular bone region, just porous cortical like bone, within the gorilla postorbital and BR regions (although there was some near

and around the frontal sinus) and the gorilla whole bone analysis had the highest BVF at 0.92. Having one *Gorilla* sample limits the ability to draw a substantial conclusions about the difference observed, but if the specimen is representative of the mean of the species, then the results of this study suggest that patterns of trabecular bone morphometry related to body mass and phylogeny found within the humerus and femur of apes may differ from that observed in the supraorbital region. We found that trabecular bone in the *Pan* browridge, relative to *Papio,* is absolutely denser (higher BVF), consisting of absolutely larger, well-spaced trabecular that are fewer in number. This finding is consistent with that of Ryan and Shaw (114). Furthermore, *Cebus* have the lowest mean BVF. While this parameter differs significantly, Ryan and Shaw (114) found that in primate humeri and femora, trabecular BVF scales positively with body size, but with negative allometry. In other words, while larger primates have on average greater BVF relative to smaller primates, the increase in BVF is not proportionate to their increase in body size. The relatively small BVF observed in humans is consistent with other regions of the body where human trabecular bone is approximately 50-75% the BVF of *Pan (91)*.

All animals differed significantly in trabecular bone thickness, with the exception of *Papio* and *Cebus*. All animals differed significantly in structure model index in at least one location. Like BVF, trabecular thickness has a positive relationship with body mass, but scales with negative allometry. The results of this study are consistent with the pattern observed by Ryan and Shaw (114) for the primate femur and humerus, such that the *Pan* sample has the largest mean trabecular thickness, followed by humans,

Papio and then *Cebus*. While the absolute values differ significantly, these differences may be primarily caused by body mass and are not an indication of an adaptational response. They may also support that while *Pan* has absolutely greater trabecular thickness compared to smaller taxa in this study, it has very thin trabeculae relative to its own body size.

Intraspecific Trabecular Differences

Intraspecific differences across the postcranial skeleton and the mandible are summarized in Table 2.14.

Bone Volume Fraction

BVF is generally greater in the supraorbital region compared to many postcranial regions of the same or like species and in the supraorbital region, BVF differs significantly across species (Table 2.14). Normal human trabecular bone from the proximal medial region of the tibia is less dense (mean BVF=0.21) than it is in the supraorbital region of humans, *Pan*, *Papio*, and *Cebus* (133). Trabecular bone is also less dense throughout other human postcranial regions. Hildebrand et al. (97) described the architectural characteristics of trabecular bone within the human spine, femur, iliac crest, and calcaneus. Mean bone volume fraction within these sites ranged from 0.083 (lumbar vertebrae) to 0.261(femoral head), whereas the mean BVF for the human postorbital and BR was 0.354 and 0.377, respectively. Trabecular BVF in T8 vertebrae of *Homo*, *Pan*, *Gorilla*, *Pongo*, *Hylobates* displayed average BVFs between 0.2863 (*Homo*) and 0.39 (*Hylobates*) (93), but differences between species were not determined significant. BVF in the supraorbital region showed a much larger range of variation (mean values ranging

from 0.295 in the postorbit of the *Cebus* to 0.746 in the post orbit of *Pan*) but were overall higher. Trabecular BVF in the humeral head of *Pan* was 0.407 and 0.569 in the head of the femur (101). In *Papio anubis*, a mean BVF of 0.64 has been reported for trabecular bone in the proximal femur, and 0.35 in the proximal humerus of by Fajardo and Muller (98)and 0.516 for the head of the femur and 0.382 for the humeral head of *Papio* species by Ryan and Walker (101). Trabecular BVF from the femur is higher or comparable to that in the supraorbital region observed from this sample of *Papio* (0.46 in the postorbital region and 0.52 in the BR). In the small bodied New World Primate *Ateles paniscus*, mean BVF is 0.29 in the humerus, and 0.46 in the femur. Again, trabecular BVF in the femur of *Ateles paniscus* is higher than in the supraorbital region of *Cebus*, but trabecular BVF in the humerus of *Ateles paniscus* is the same or lower than that observed in the supraorbital region of *Cebus* (postorbital=0.295; BR=0.321) (98). The human supraorbital region has comparable BVF relative to the first and second metatarsal, but *Pan* and the *Gorilla* has much greater BVF in the supraorbital region compared to regions within the first and second metatarsal (134). Mean BVF of the trabecular bone within the mandibular condyle of *Callithirx jacchus* is 0.364, 0.507 in *Saguinus fuscicollis*, and 0.395 in *Saimiri sciureus (105)*. The average BVF in the human mandibular condyle was 0.17 (135), which is lower than the average BVF of the supraorbital region.

Degree of Anisotropy

Relative to postcranial regions, trabecular bone in the supraorbital region shows low to moderate anisotropy. Normal human tibial trabecular bone is more oriented than

it is in the supraorbital region of humans, *Pan*, *Papio*, and *Cebus*, with a mean degree of anisotropy of 6.56 (determined by the star volume distribution method) (133). In the study by Hildebrand et al. (97), mean degree of anisotropy ranged from 1.42 (lumbar vertebrae) to 1.75 (calcaneus). A study of trabecular bone within the T8 vertebrae across hominoid species (*Homo*, *Pan*, *Gorilla*, *Pongo*, *Hylobates*) ranged from 1.32 (*Pan*) and 1.45 (*Hylobates*) but displayed no significant differences in degree of anisotropy across species (93). While Griffin et al. (46) found no significant difference in BVF between ape and human metarsal trabecular bone, they did show that humans possess greater anisotropy in this region compared to other great apes, a possible consequence of bipedalism. Degree of anisotropy of trabecular bone in the BR is comparable to that in the humerus of *Papio* (1.78) and *Pan* (1.59), but low relative to the femur of *Papio* (2.52) and *Pan* (2.43) (101). Degree of anisotropy in the humerus and femur of *Ateles paniscus* is lower than that of the postorbital region of *Cebus*, but comparable to the BR region (DA=2.327 and 1.474); however, there was an unusually high standard deviation in the degree of anisotropy of the postorbital region of the postorbit of *Cebus*. This study by Fajardo and Muller (98) was from one animal. Degree of anisotropy in the mandibular condyle of humans (1.51) is lower than that of the human postorbital region (2.401), but comparable to the DA of the BR (1.64) (135). Compared to all species, DA in the mandibular condyles of *Callithrix jacchus*, *Saguinus fusciollis*, and *Saimiri sciureus* were comparably much higher (ranging from 5.34 to 10.29), relative to the supraorbital region, but with no significant differences found between gouging and non-gouging species (105).

Structure Model Index

Overall, trabecular bone in the supraorbital region of *Homo*, *Pan*, and *Papio* is more plate-like/ honeycomb-like relative to postcranial regions. Mean structure model index of normal human trabecular bone in the medio-proximal end of the tibia is 1.31, or plate-like, but more rod like relative to that found for supraorbital region in all species. The structure of trabecular bone in the human tibia is closest to that in the postorbital and lateral BR regions of *Cebus* (133). Type (rod or plate-like) of trabecular bone, described by structure model index varies greatly between individuals and location (97). More rod-like trabeculae are found in the lumbar spine (SMI=2.12) while more plate-like trabeculae are found in the iliac crest (SMI=1.15) and the femoral head (SMI=0.41). Hominoid thoracic vertebrae in the study by Cotter et al. (93), are characterized as plate-like bone, with an SMI of 0.428 in *Pan*, 0.1583 in *Gorilla*, and 0.7050 in humans. SMI in the superior and inferior femoral neck of *Ateles geoffroyi* was -0.507 and -0.761, respectively (45). Giesen and van Eijden (135) describe trabecular bone in the human mandibular condyle as being made up of parallel trabecular plates, which they assess through visualization of 3D renderings.

Trabecular Thickness

In both human and *Pan*, trabecular thickness is much higher in the supraorbital region than in postcranial regions. In humans, trabecular thickness is generally similar across all regions considered by Hildebrand et al. (97) ranging from 0.122 mm (lumbar vertebrae) to 0.194 mm (femoral head). The human mandibular condyle had an average trabecular thickness of 0.10 mm (135). Values of trabecular thickness in the BR are

around 2 times greater than in the post cranial skeleton and three times greater than the mandibular condyle, ranging from 0.288 mm to 0.300 mm. Trabecular thickness in the thoracic vertebrae of *Pan* is 0.174, and of *Gorilla* is 0.217 (93). . In the humeral head of *Pan*, trabecular thickness is 0.173 mm and in the head of the femur of *Pan* is 0.251 mm (101). *Pan* supraorbital bone mean trabecular thickness ranges from 0.346-0.401 mm. *Cebus* and *Papio* trabecular bone in the supraorbital region is conversely more similar or lesser in thickness to that found in post cranial regions. In *Papio* trabecular thickness is around 0.2 mm across the supraorbital region. Trabecular thickness in the humerus of *Papio* is 0.157 mm and in the femur of *Papio* is 0.256 mm (101). In *Papio anubis*, trabecular thickness measured 0.167 mm in the head of the humerus and 0.400 mm in the head of the femur (98). In *Cebus*, trabecular thickness across the supraorbital region ranges between 0.187 to 0.208 mm. Trabecular thickness of *Ateles paniscus* is 0.182 mm in the humeral head and 0.339 mm in the femoral head. Trabecular thickness in superior and inferior regions of the femoral neck of *Ateles geoffroyi* were 0.265 mm and 0.277 mm, respectively (45).

The differences observed suggest that elastic properties obtained from the human tibia, other long bones, or the mandibular condyle may not accurately describe the supraorbital region. More realistic elastic values in these regions will likely improve the accuracy of FEMs in predicting the deformation of the craniofacial skeleton during various types of loading. New studies are currently underway to determine the elastic properties of this region in each species and other craniofacial regions and to investigate the relationship between density and structure of trabecular bone and the elastic

modulus. In some measures, humans and *Pan* seem more similar and in other measures humans seem more similar to *Cebus*. Differences between humans and *Pan* highlight the difficulty in determining the type of properties that should be used to model human ancestors. However, trabecular properties could be obtained from fossil scans and compared to the values reported here in order to make a prediction about the elastic properties of the supraorbital region of our human ancestors. These questions would likely benefit from determining the role that body mass, phylogeny, and bone shape play in influencing trabecular bone parameters and modulus in craniofacial regions, which could be achieved not only through principle components analysis, or discriminate function analysis, but also by comparing the microstructural organization of trabecular regions.

The Biomechanical Significance of the Primate Browridge

Although DA scales inversely with increasing body mass in the study by Ryan and Shaw (114), the authors conclude that the weak correlation is an indication that DA is essentially unrelated to primate body size. Significant differences in DA between *Homo* and *Pan*, *Homo* and *Papio*, and *Pan* and *Cebus*, suggest that there are two groups: a group that includes *Homo* and *Cebus* and a group that includes *Pan* and *Papio*. These results suggest that DA is related possibly to the shape of the supraorbital region and therefore to differences in function between these groups, in spite of phylogenetic relationships. Higher anisotropy in *Pan* and *Papio* suggests that the region may be adapted to a more unidirectional force, a slight difference that could be related to differences in shape or function or both.

The extensive variation observed in extant and extinct primate craniofacial form and robusticity have been attributed to biomechanical, or orofacial (incisal and masticatory) function (1). However, both spatial and biomechanical models have been used to explain variation in supraorbital robusticity. Particularly, it is has been hypothesized that the robust or projecting browridge observed in living apes and Pleistocene *Homo* is a product of sphenoid length, is an adaptation of protective buttressing, or is a consequence of overall facial robusticity (20-23,136). Ravosa (24) found that the main determinate of browridge morphology is facial size and that browridge antero-posterior length is strongly correlated with neuro-orbital disjunction, while supero-inferior length is correlated with masticatory muscle size and craniofacial torsion during mastication. Most of these explanations aren't satisfactory in explaining the variation among browridge morphologies because they fail to suggest a mechanism of browridge growth. The masticatory stress hypothesis, which partly posits that browridge robusticity is an adaptation to counter bending stresses induced by anterior tooth loading, does attempt to identify the mechanism driving browridge form, but has been weakened by strain gage experimentation performed by Hylander and colleagues (25-29). These experiments show that the supraorbital region experiences significantly less strain compared to the zygoma and zygomatic arch, suggesting that it is "overbuilt" relative to other craniofacial regions, and therefore its structure may be of lesser mechanical significance for resisting masticatory loading.

While the disparity in relative strain and the robust morphology that characterizes many primate species suggests that in some species this region may be "overbuilt" for

orofacial function, cortical bone mechanical studies show that material bone properties in this region are sensitive to orofacial function. Cortical bone in the supraorbital region is significantly ($p=0.001$) thinner and denser in edentulous individuals compared to dentate individuals (34). Therefore, even though the browridge region undergoes markedly less strain than the zygomatic region during molar and incisal loading, its cortical structure and thus its material properties appear to be responsive to changes in masticatory forces. These results challenge the assumption that supraorbital and zygomatic regions respond equally to peak strains induced by mastication. Additionally, cortical bone elastic properties in the supraorbital region have been investigated in several primate species, including baboons, macaques, humans, (3,4,6,35) and in chimps and capuchins (in progress). These studies show some unexpected patterns in cortical thickness and density such that bone tissue in the supraorbital region is thicker than other regions of the human craniofacial skeleton, like the zygoma, which undergoes relatively higher strains during orofacial function. Cortical bone in the supraorbital region is transversely isotropic and therefore possibly adapted to resist loads in the frontal or coronal plane.

The inconsistency between regional strain magnitude and adaptive remodeling in primate upper and mid-craniofacial regions may be caused by differences at the cellular level. Frost (48) proposed that the bone remodeling response can be described as a "mechanostat," in which bone mass is determined through a mechanical feedback system regulated by hormones and biochemical agents. Furthermore, these hormones and biochemical agents can regulate the remodeling response by adjusting the minimum

effective strain (MES) required to incite a remodeling response. If strain goes below the MES, then bone loss occurs. Frost (48) suggested that, during normal activity, most vertebrate bone remodels to maintain strain levels between 100 and 1500 microstrain. The typical range of peak strains for vertebrate long bones during vigorous activity is between 2000 and 3000 microstrain (31,49).

The bone remodeling response is complicated by the "theory of cellular accommodation" (50). This theory proposes that bone cells react strongly to initial changes in mechanical environment, yet the reaction slows down or stops once the cells accommodate to change. Terminal bone mass is then not only a product of the local strain environment, but also is affected by the temporal sequence of loading. This mechanism has been observed in rat tibia where there is a greater bone remodeling response to an initially large mechanical load which trails off compared to an initially small load which grows in magnitude (51). This has also been observed in trabecular bone (52). Kupczik et al. (10) tested the theory of cellular accommodation in the supraorbital region of the crab-eating macaque finding that supraorbital strains are not high enough to warrant a bone modeling or remodeling response that results in a robust browridge. The supraorbital region may adapt so rapidly that high strains are not observable: the highly strained zygoma undergoes very slow growth relative to the low strained browridge, which grows rather rapidly in development. While their study does not support the modeling of a robust browridge due to an initially large strain, there are other possible explanations for browridge development based on Frost's (1987) and Turner's theories (50). MES is site and age dependent and could be lower in the

supraorbital region as an adaptive response to maintain a certain amount of bone in the region for either orofacial function or other purposes, such as protection or support of the brain, eyes and musculature (16). In other words, the browridge may have a lower threshold for strain, demonstrating a greater bone remodeling response than the zygomatic region, which must have a greater strain threshold in order to withstand more frequent loading of a greater magnitude (10,50,51). Also, it could serve the purpose of diffusion of stress during mastication. The role of minimum effective strain and cellular accommodation in the browridge cannot be assessed without observing variations across the craniofacial skeleton at the cellular level. Studies have been conducted comparing osteocytes across cranial and post-cranial regions in mice, finding the osteocyte cell bodies in the cranium are rounder as opposed to more oblong osteocytes in the tibia (82). In vitro experimentation has found that rounder osteocytes are more sensitive to fluid shear stress, producing more nitric oxide than more oblong osteocytes. Nitric oxide is a major signaling molecule involved in bone remodeling (137).

Ross et al. (16) found that during mastication in the macaque crania, masseter muscle forces induce twisting and bending in the zygomatic arches around an axis drawn from the anterior and posterior attachment of the muscle to the bone. The twisting and bending of this region applies infero-laterally directed tension on the lateral region of the inner orbital wall, the infraorbital plate, and the anterior arch. This tension causes the curvature of the lateral orbital wall to bend outwards, or straighten, and this creates compressive forces along the superior surface of the browridge and tensile forces on the inferior surface of the ridge. Tension in the supero-lateral and infero-medial regions and

compression in the infero-lateral and supero-medial regions of the orbit was also observed. Ross et al. (16) compared the deformation regime observed in their macaque model to Endo's (29) data on stress and strain observed around the orbits in *Homo* and *Gorilla,* finding that all three species undergo a similar pattern of deformation in these regions. More laterally (near the post orbit and lateral browridge) it appears that tensile force is directed in the curved direction of the bone, but then as you move medially, this force becomes directed in the medio-lateral orientation. How these forces affect the browridge internally has never been investigated. In this study we characterized primary, secondary, and tertiary strain orientations in the browridge trabecular bone regions of 4 common chimp FE models. Four primary observations of the internal strain environment of the supraorbital region from these models are as follows:

1. Primary and secondary strain orientations show variability between working and resting sides, but do not show intraspecific variability (between the 4 chimp crania) or variability between premolar and molar biting.
2. Strain orientations on the resting side are more consistent across the whole browridge and include:
    a. A primary (tension) tensor in the inferolateral-superomedial direction.
    b. A secondary (compression) tensor in the superolateral-inferomedial direction.
    c. A tertiary (compression) tensor in the inferoposterior-superoanterior direction.

3. Strain orientations on the biting side are similar, but show greater directional variability in all three vectors, such that secondary strain orientation becomes tertiary (more antero-posteriorly oriented) and tertiary orientation becomes secondary.
4. PO regions contain more unidirectional vectors of higher magnitude.

Based on the primary and secondary strain patterns in the brow ridge, we would expect to see trabeculae aligned along the inferolateral-superomedial direction. Due to a lack of consistency in orientations across the whole region between resting and working sides, we would expect that bone will not be strongly anisotropic (indicated by having a low degree of anisotropy relative to postcranial regions). Differences between the brow ridge and postorbital region suggest that greater anisotropy should be observed in the postorbital region along with stronger bone (measured by higher BVF). Observations from the FE models suggest that if the browridge subcortical bone is sensitive to strains induced by orofacial function, trabecular bone in more lateral regions of the browridge, which experience more uni-directed strain of a higher magnitude should be characterized by significantly denser, more highly oriented (as described by degree of anisotropy) trabecular bone.

Our trabecular bone analysis found that only trabecular bone in the PO region of *Pan* is denser and that only the PO region of humans and *Cebus* is more anisotropic relative to the browridge. Trabeculae in the supraorbital regions lie in sagittally oriented plates and not along the primary strain orientations observed in the models. One might expect that trabecular bone oriented along the medio-lateral axis would be most efficient

at resisting bending along the medio-lateral axis of the bone. While there is less bone laid down in the medio-lateral direction relative to the antero-posterior and infero-superior directions, this orientation was the most consistent, suggesting that there may be a consistent load affecting it. The primary distribution of plate-like structures in the sagittal plane however, seems more likely to be an adaptation to provide protection to the orbit or anterior cranial cavity from extraneous forces, as is proposed by the protective facial buttressing hypothesis (136). This observed pattern may be controlled more so by heritability mediated by growth patterns. Higher interspecific variation represented by greater significant differences in BVF and SMI between species support the hypothesis that the dense plate-like formation of trabecular bone in the supraorbital region is a heritable or systemic adaptation. DA on the other hand varied less interspecifically relative to BVF and SMI and more intraspecifically relative to BVF, a result which supports what other studies on post cranial regions have shown: while differences in anisotropy are not always found between species due to overall similarities in gross bone morphologies and function, they are more indicative of functional adaptation. This is also supported by studies that find that changes in material orientation of bone occur secondarily to increases in BVF. For example, Tanck et al. (138) assessed proximal tibia and vertebra of female pigs, finding that during growth, bone volume fraction and stiffness increased at a rapid rate in the initial phase of growth, whereas trabecular morphometry tended to change and trabecular orientation tended to increase in later growth stages, after peak bone mass had been achieved.

The subcortical region of all animals in this study was found to contain honeycomb-like, or plate-like bone lying primarily in the sagittal plane. We see a similar pattern of trabeculae in the mandibular condyle, which is also composed of sagittally oriented trabecular plates, but is much less dense. Also similar is the variability of orientation in the primary and secondary eigenvectors, but consistency of orientation in the third eigenvector. In the supraorbital region, trabecular bone orientation is most consistent and uniform in the medio-lateral direction. It has been suggested by Giesen et al. (106) and others that the condyle is adapted to endure relatively low stress, but from many directions as opposed to cyclical, high magnitude unidirectional loads (107,139). It is possible to infer from this pattern that the antero-posterior and supero-inferior mass of trabecular bone is under greater genetic control and not influenced by loading. The pattern of trabecular orientation in the supraorbital region is most consistent with the hypothesis that the robust browridge is adaptation to resist blows directed at the brain case or eyes (136). While the medio-lateral direction contains the least amount of bone material relative to directions orthogonal to it, the consistency and significance of bone material in this direction is indicative of a more consistent loading pattern- perhaps a bending along the frontal plane. In conclusion, primary trabecular orientation in the supraorbital region does not support the hypothesis that the robust projecting browridge is an adaptation to masticatory loading, but greater trabecular bone density in the *Pan* PO region, greater anisotropy in the human and *Cebus* PO region, and greater whole bone density (trabecular and cortical bone together) in human, *Pan*, and *Cebus* PO

region do support the hypothesis that the bone in this region might be adapted to, or at least under the control of orofacial function to some extent.

Due to the number of factors that contribute to bone formation, more than one explanation could be jointly responsible for browridge morphology. Furthermore, it is difficult to deconstruct various roles of environmental stimuli, genetics, and development in forming the browridge without examining the microstructure and differences at the cellular level. We feel that our data support the facial buttressing hypothesis, but does not completely exclude the masticatory stress hypothesis. Indeed, strong genetic factors influencing the orientation of trabeculae in the browridge may override environmental signaling induced by orofacial function, which may be contributing more to the maintenance of the cortical bone density.

Limitations

Many studies have found that age, gender, and hormones have an effect on bone density in humans, but not a large effect on other trabecular bone morphometric properties; less is known about its effects on apes and monkey species (98,140-142). Our human sample contained at least 3 individuals over the age of 70 (one individual's age was unknown), and at least 1 adult under the age of 40. There were also more males than females. We did not test the effects that age or sex played on the BVF of our sample. It was difficult to tell if the data was normally distributed, so we performed parametric statistics to decrease the likelihood of type 1 error.

In general, finding comparable regions of analysis proved difficult due to morphological variation across individuals and especially between species. Some

samples lacked a zygomaticofacial suture (lateral landmark) and some lacked a supraorbital foramen or notch (medial landmark). Additionally, in the apes and baboons, the supraorbital region projects out, sitting more anterior to the braincase, whereas in capuchins and especially humans, the supraorbital region sits inferior relative to the braincase. While differences in morphology across species created challenges in determining comparable regions of interest, observing trabecular variation in this region across such species also helped shed light on how different the same region across various primate species can be. In trabecular bone analysis, due to oversampling error it is important to keep volumes of interest scaled to body size and locations of VOIs should represent biomechanically similar locations and dimensions (98). The limited regions of trabecular bone and variations in the amount of trabecular bone within the region across species made it impossible to obtain symmetrical volumes of interest scaled to body size. While this study did not scale volumes of interest to body size, it analyzed all trabecular bone within each region. Because of this, volumes of interest were determined by each individual and therefore influenced by differences in body size across the individual and species level (105,143). Furthermore, trabecular regions are restricted by the small height of the supraorbital regions and at times cortical and trabecular bone interfaces were difficult to discern. The authors coped with these limitations by creating a standard way of outlining trabecular regions which could be applied to all individuals and species as was described in the methods section of this paper.

CHAPTER III

INTERNAL BONE ARCHITECTURE IN THE ZYGOMA OF HUMAN AND *PAN*

Synopsis

The primate zygoma is a bone whose proper functioning is central to healthy orofacial function. The importance of the variability of its morphology observed across extinct and extant primate forms has been tested using finite element analysis, however, the internal structure of this bone has not yet been explored. In this study, μCT is used to characterize trabecular bone morphometry in two separate regions of the zygoma of humans and *Pan*. Trabecular anisotropy and orientation was compared with the strain observed in trabecular regions of finite element models of four *Pan* crania. The results of this study show that unlike other regions of the craniofacial skeleton, trabecular bone morphometry, anisotropy, and orientation are highly predictable based on strain orientation and magnitude in the finite element models. Trabecular bone in the zygoma is orthotropic and its orientation is primarily in the medio-lateral direction. In conclusion, trabecular bone in the zygomatic region appears to be highly influenced by the local strain environment, and is thus highly adaptable to orofacial function.

Introduction

The primate zygoma is highly variable in its gross anatomy. This variability is likely due to its importance as a load bearing bone. Serving as an attachment site for the masseter muscle, the zygoma is subjected to high strain brought about through the incision and mastication of food. The most superior projection of the primate zygoma forms the lower part of the post-orbital bar, an enigmatic and unique aspect of primate

craniofacial anatomy. In addition to benefiting our knowledge of craniofacial form, function and development for living humans, characterizing the gross and microscopic anatomy of this region is critical to interpreting the primate fossil record.

The robust zygomaticoalveolar region characterizing australopithecine crania was initially hypothesized to have served as a pillar of support during the mastication of hard food objects (144). It was also hypothesized that the lateral orbital wall was adapted to endure tensile strain induced by temporalis and masseter muscle usage, just as in *Homo* and *Gorilla*. More recently, finite element modeling of a macaque crania demonstrated the high concentration of compressive and tensile strain in the anterior root of the zygomatic arch, which is medially located relative to the masseter muscle and superior to the tooth row. High tensile and compressive strains observed in the anterior root of the zygoma suggest that the region undergoes high shear strain (16). It is argued that the region is a significant feeding adaptation because bone is weakest under shear strain. Because bite force does not have a significant effect on strain magnitude and orientation in zygomatic regions, there are few differences between working and balancing sides. The primary source of strain in the zygoma originates from masseter muscle force during chewing.

Trabecular orientation in the post-cranial skeleton is highly correlated with principle tensile and compressive strain orientations. Furthermore, regions with greater trabecular density correspond to regions that experience greater stress (85,89,90,92). Micro-computed tomography is a highly useful method of characterizing trabecular bone architecture and has been used extensively in the study of primate post-cranial bone

(45,46,93-103) and mandibular bone (104-107). Assessing the structural characteristics and variation of trabecular bone structure and orientation of trabecular bone in the primate zygoma is critical to the interpretation of the adaptational significance of the zygoma.

Finite element (FE) analysis is an engineering method used to test hypotheses regarding the structural significance of primate craniofacial form. It has been performed on models of human, chimpanzee and macaque crania as well as fossil crania including *Australopithecus africanus, Paranthropus bosei,* and *Australopithecus sediba* (1,2,8,10,11,16,18,19,108-113). Region and species-specific variations in subcortical craniofacial bone may affect the outcomes of finite element modeling of the primate craniofacial skeleton. In these models, trabecular bone is modeled as a continuum, in which the whole trabecular body is represented as an average of trabecular material properties across the region. Modeling the trabecular region as an average with an appropriate tissue modulus (1-2 GPa in the mandible) will produce an accurate FE model (14).

Currently, because we do not have tissue modulus data for primate craniofacial trabecular bone, trabecular volumes within orbital and zygomatic regions of primate craniofacial finite element models (FEMs) are modeled as solid regions using isotropic elastic properties (E=637 GPa, v=0.28) obtained from trabecular bone within the human tibia. (8,13). We know that the precision of FE modeling is improved when region-specific orthotropic elastic properties obtained from cortical bone is used (Dechow and Hylander 2000; Richmond et al. 2005; Strait et al. 2005), and this is likely also the case

for trabecular bone elastic properties. Possible variation between primate species and between regions of the craniofacial skeleton should not be ignored. One purpose of this study is to serve as a preliminary step towards determining the material properties of trabecular bone within the zygomatic region of *Pan* and humans for use in future finite element modeling.

In this study we describe the cortical and trabecular bone density, architecture and fabric anisotropy in the zygoma of humans and *Pan* using micro-computed tomography. We compare bone volume fraction (BVF), trabecular separation, thickness and degree of anisotropy (DA), along with primary orientations of trabeculae between two human zygomatic regions and between one human and the corresponding *Pan* zygomatic region. We describe strain orientation within the trabecular regions of four *Pan* FEMs in order to compare it with primary trabecular orientation (18). We expect to find that trabecular bone in the anterior root of the zygoma, which undergoes high shear strain will be denser and have higher anisotropy that trabecular bone in the lower postorbital wall. We hypothesize that if the zygoma is adapted in part to orofacial function, trabecular orientation, especially in our *Pan* specimens, will match primary and secondary strain orientations in the *Pan* FEMs. The gracile human craniofacial skeleton is likely adapted to processing softer foods than *Pan*, possessing smaller muscles of mastication, and also differs systemically, being characterized by relatively low bone volume fraction (91,145). We hypothesize that trabecular bone morphometry in the human zygoma will reflect these differences in diet, muscle morphology, and cranial robusticity found between humans and *Pan*. More specifically, we expect to find that

trabecular bone in the zygoma of *Pan* will reflect greater systemic cranial robusticity and greater muscle forces, having higher bone volume fraction, greater trabecular thickness, and greater anisotropy.

Materials and Methods

For this study we analyze trabecular bone in humans and the closest living relatives *Pan* in order to assess the differences that may have existed between humans and fossil hominids. Bony zygoma regions, extending from the lower zygomatic part of the postorbital wall to the lower border of the zygoma region, were obtained from 8 human (2 females, 6 males, mean age ± SD: 54.4 ± 19.63) and 4 *Pan tryglodytes* (2 adult females and 2 adult males) and 1 *Pan paniscus* (adult female) crania using a Stryker bone saw and stored in equal amounts of isotonic saline and 95% ethanol. Human crania were obtained from the willed body program at the University of Texas Southwestern Medical Center. *Pan* specimens were obtained from Yerkes Primate Center, the Southwest National Primate Center, and the Antwerp Zoo (the bonobo).

Specimens were scanned in the saline alcohol solution at Baylor College of Dentistry in Dallas, Texas using a Scanco Medical µCT 35 (Scanco Medical, Basserdorf, Switzerland) at a resolution of 37 µm, an energy of 70 kVp, an angulation of 114 µA, and an integration time of 400 milliseconds.

Volumes of Interest

Upper and lower zygomatic trabecular volumes were analyzed in the human specimens. Because lower zygomatic regions in four out of five of our *Pan* specimens contained dense cortical bone, with little to no trabecular bone, only an upper volume

was analyzed (Figure 3-1). The lower trabecular region consisted of the trabecular bone within the body of the zygoma, the region was demarcated inferiorly and superiorly by upper and lower boundaries of the temporal process of the zygoma. The upper region consisted of trabecular bone in the lower post orbital bar. The lower boundary was the lower corner of the orbit and the upper boundary was the mid-point of the post orbital wall. Trabecular bone regions were bounded posteriorly and anteriorly by the bony cortical wall of the zygoma.

Trabecular Bone

All trabecular bone lying within each volume of interest was analyzed. In Table 3.1, we provide the average body mass and trabecular bone volume that was analyzed for each species. Within each volume, regions of trabecular bone were contoured by hand on every 10^{th} slice (37 μm in width). An analysis function was used to morph this contour between every 10^{th} slice. An automatic contouring function was then applied to the existing contour to create a systematic result, by setting an inner and outer (inside the contour and outside the contour) value of mg of HA per cubic centimeter for the new contour to iterate. Each contour was inspected for accuracy.

Segmentation

We used the Riddler and Calvard (118) and Trussel (96,119,120) method, provided by Scanco Medical as an image processing language script (IPL), to extract the mineralized bone phase. The threshold for each specimen was therefore individualized to its density.

MicroCT Analysis

Bone volume fraction (BVF; marching cubes method), and material and apparent density was determined for whole bone regions (including cortical shell and trabecular bone; based on gray values defined by a phantom specimen) (121). Apparent density describes the mg of hydroxyapatite per cubic centimeter that include bone material and voids. The material density describes the mg of hydroxyapatite per cubic centimeter of the bone material excluding all voids, or non-bone material.

Once contoured and with a threshold applied, a pre-written IPL script (Scanco Medical software) was applied to determine degree of anisotropy (mean intercept length method (Whitehouse, 1974; Harrigan and Mann, 1984), structure model index (triangulation method (97,125), trabecular separation, thickness, and number (distance transformation method (97,125)) connectivity density (Euler method (126)), and bone volume fraction (BVF).

Statistical Analysis

Significant differences by region within each species were determined by Mann-Whitney U tests (SPSS). Intraspecific differences between the two human regions were explored using the Wilcoxon sign test (SPSS). Primary, secondary and tertiary eigenvectors (H2, H3, and H1, respectively) were tested for correlation with one another and were plotted relative to basic anatomical axes using Origin Lab Pro. Oriana was used to calculate mean angle and standard deviations for each eigenvector. Significance of each mean angle was tested using Raleigh's test for uniformity, intra and interspecific

significant differences were tested using Watson Williams F test for multiple comparisons ($p \leq 0.05$).

FEA of the Pan *Zygoma*

This study utilized 4 *Pan* cranial FEMs to capture the internal strain patterns in the zygoma during orofacial function, describing primary, secondary, and tertiary strain (18). The FE models were constructed from 4 CT scans representing the morphological extremes of a collection of 19 *Pan* cranial specimens. The models incorporated region-specific values of cortical bone properties and muscle force for the anterior temporalis, deep and superficial heads of the masseter and the medial pterygoid, all acquired from additional *Pan* specimens. Trabecular regions were represented as solid separate objects. Isotropic tissue modulus values obtained from human tibial trabecular bone were assigned to these objects (13). Finite element analysis was performed on each model, with constraints at the TMJ and the foramen magnum. Bite point forces were applied at the third premolar and the second molar. Once the analysis was complete, the cortical bone was hidden in order to observe strain in the trabecular objects (See Smith et al. (18)). In the results section, primary, secondary and tertiary strain orientations and relative magnitudes from these FE models are described and discussed relative to our μCT determinations for trabecular orientations and bone density.

Results

MicroCT Visualization

This study looked at two regions of the zygoma, an upper region, which was contained in the lower post-orbital bar, and a lower region, which lies directly medial to

the zygomatic arch. Before these regions were analyzed, there were visible differences in trabecular bone type and volumes observed in most individuals of the human sample across the zygomatic body and between humans and *Pan*. Figure 3-2A shows the range of variation in trabecular structure found among our human sample in the zygomatic body (congruent to the temporal process of the zygomatic bone). Furthermore, trabecular bone type appeared to differ across the human zygomatic body latero-medially, such that plate-like trabecular bone tends to lie parallel to the cortical surface in the lateral region of the zygomatic body, but tends to thin out and become more rod like in the medial region of the zygomatic body. Figure 3-2B1 and 3-2B2 not only show the relatively large region of trabecular bone found within the zygomatic body in two of our human specimens, but demonstrate this pattern of trabeculae. For our analysis, in spite of these observable differences, we analyzed the whole zygomatic body region because demarcation of each region between individuals in our sample was not discernable. However, qualitative observance of this pattern suggests that there are major differences in strain across the zygomatic body that may affect trabecular bone type and orientation. Additionally, large differences between the zygomatic body (lower region) between our human and *Pan* samples were observed. Lower zygomatic regions in *Pan* were for all but one specimen nearly filled in with dense bone, leaving no discernable trabecular region for analysis. Figure 3-2C1 is a cross section of the one *Pan* individual that contained trabecular bone within the body of the zygoma. Figure 3-2C2 is a cross section of the body of a *Pan* zygoma that is representative of the remainder of the sample. Both

human and *Pan* samples contained discernable trabecular bone regions in the upper zygoma/ lower post-orbital bar.

Whole Bone Analysis

Before analyzing the trabecular region, we conducted a whole bone analysis on both cortical and trabecular bone in the upper zygomatic region to look at differences in the overall density of the lower post-orbital region in humans and *Pan*. Density measures of combined trabecular and cortical bone regions of the upper zygoma found that BVF (ratio of bone volume to total volume) is significantly greater in *Pan* ($p=0.008$). While apparent density (density of the bone material and voids) is greater in *Pan* and material density (density of only bone material) is greater in humans, these differences were not statistically significant (Table 3.2). These results are comparable to that observed in the browridge, in which *Pan* has greater BVF and apparent density than humans (*Pryor et al. in prep*).

Trabecular Bone Analysis

Interspecific and Intraspecific Comparisons of Trabecular Bone Morphometry

Table 3.3 provides means and standard deviations of trabecular bone morphometric variables in the upper and lower human and upper *Pan* zygoma. Table 3.4 provides the results of the Mann-Whitney U significance tests. Upper *Pan* zygoma regions have greater BVF ($p=0.005$), trabecular number ($p=0.005$), and trabecular separation ($p=0.013$) relative to upper human zygoma regions. Furthermore, SMI ($p=0.055$) is trending towards significance, suggesting that *Pan* regions contain more plate-like trabecular bone than human regions.

Wilcoxon tests for intraspecific differences between upper and lower human zygoma regions found significant differences in degree of anisotropy ($p=0.015$), connectivity density ($p=0.021$), and material density ($p=0.015$). Lower human zygoma regions were more anisotropic, but less materially dense and with lower connectivity density (Table 3.5).

Material Distribution and Angular Orientation

Material orientation computed by our μCT analysis is expressed by three eigenvectors: H2, which provides direction and magnitude of the primary orientation of trabecular bone material (the direction in which most bone material is oriented); H3 which provides direction and magnitude of the secondary orientation of trabecular bone material; and H1, which provides direction and magnitude of the tertiary orientation of bone material. Comparing eigenvector magnitudes in each region shows that the lower zygoma is more anisotropic (strongly oriented) and orthotropic (magnitudes differ in three directions) than the upper zygoma, which is more transversely isotropic (two eigenvector magnitudes are very similar) (Figure 3-3). Eigenvector magnitudes in both upper and lower zygomatic regions are moderately to strongly correlated with one another, suggesting that relative magnitudes may allude to functional significance, possibly relating to relative strain magnitudes, or the nature of bone formation in the region. The strongest correlation was found between H3 (secondary) and H1 (tertiary) directions in the lower human zygoma ($R=0.96$) (Figure 3-3).

An important distinction between regions is that in the upper zygoma, primary and secondary vectors are closer in magnitude, while in the lower zygoma, secondary

and tertiary vectors are closer in magnitude. This means that in the upper zygoma, bone material is more strongly oriented in two directions, while in the lower zygoma, material is oriented more strongly in one primary direction. The primary vector, H2, was significantly oriented ($p<0.001$) against all anatomical axes in the lower human zygomatic region, lying along the medio-lateral axis, and nearly 90 degrees from AP and IS axes (Table 3.6; Figure 3-4). Secondary (H3) and tertiary (H1) eigenvectors in this region were only significantly oriented against the medio-lateral axis ($p< 0.001$), but varied greatly across the sagittal plane (Table 3.7 and 3.8; Figure 3-3 to 3-4). In the human upper zygomatic region, H2 was significantly oriented around 90 degrees from the antero-posterior axis, while in the *Pan* upper zygomatic region, H2 was significantly oriented around 70 degrees from the infero-superior axis. Both upper zygoma human and *Pan* H1 orientations were significantly oriented nearly 90 degrees from the medio-lateral axis and H3 was significantly oriented 106 and 99 degrees, respectively from the infero-superior axis.

Watson Williams F tests detected a significant difference in angular orientation between upper zygomatic regions of human and *Pan* for H2 ($p=0.003$) and H1 ($p<0.001$). Significant differences were found in H2 ($p<0.001$) and H1 ($p=0.02$) orientations between upper and lower human zygomatic regions.

FEA of the Internal* Pan *Zygoma

Overall patterning of strain orientation in the zygoma of our *Pan* finite element models did not differ much between individuals or between PM3 and M2 biting. In the zygomatic body of the *Pan* finite element models, there appears to be two patterns of

primary and secondary strain orientation on the biting side, differing laterally to medially. More laterally, near the temporal process of the zygomatic bone, primary and secondary strain tensors fall in a transverse plane. The primary tensor (tension) lies in the medio-lateral orientation with a slight antero-posterior tilt. The secondary tensor (compression) lies medio-lateral, with a superior tilt at its lateral end (Figure 3-5). Towards the medial border of the zygomatic body, the primary tensor (tension) lies mediolaterally, while the secondary tensor (compression) lies supero-inferiorly.

In the upper zygomatic region, or the lower post orbital bar of the biting side, both primary (Figure 3-5A) and secondary (Figure 3-5B) strain tensors undergo large changes in orientation moving infero-superiorly. At the lower end, tension is directed along an infero-superior axis and gradually changes to an inferomedial-superolateral orientation. Compression is found along a medio-lateral axis in the lower end of this region and it gradually shifts to an infero-lateral supero-medial direction (nearly supero-inferior). Additionally, vectors in this region are much smaller in magnitude compared to the zygomatic body (Figure 3-5).

Discussion

Summary of Results

In this study we used micro-computed tomography to characterize cortical and trabecular bone density, architecture and fabric anisotropy in the zygoma of humans and *Pan*. We hypothesized that trabecular bone in the anterior root of the zygoma (lower zygomatic region of our analysis), which undergoes high shear strain, will be denser and have higher anisotropy that trabecular bone in the lower postorbital wall (upper

zygomatic region of our analysis). Our results only partially support this hypothesis. Trabecular bone in the anterior root of the zygoma (lower zygoma region) is significantly more anisotropic than trabecular bone in the lower post-orbital bar. Trabecular bone in the human upper zygoma/lower post-orbital bar was significantly more materially dense (higher mg HA/ cm^3) and had significantly greater connectivity density compared to trabecular bone in the lower zygomatic region of humans. However, our qualitative findings suggest that in our chimp sample, lower zygomatic regions are denser overall than upper regions, containing virtually no trabecular bone in all but one *Pan*.

Additionally, we hypothesized that if the zygoma is functionally adapted to orofacial function, trabecular orientation, especially in our *Pan* specimens, should match primary and secondary strain orientations in the *Pan* FEMs. The results of this study are consistent with this hypothesis, finding that trabecular bone alignment is found to be significantly oriented in a medio-lateral direction, which corresponds to the primary (tension) strain tensor observed across the anterior root of the zygoma in our *Pan* FEMs. In the more lateral region, primary and secondary strain tensors form a transverse plate of shear strain, while more medially, secondary strain transitions from an antero-posterior orientation to an infero-superior orientation. The average trabecular bone material orientation across the region (lateral to medial) showed greater variability in secondary and tertiary material orientation eigenvectors. This finding would be expected based on the variability observed in the secondary strain tensor in our *Pan* FEMs. Material orientation in the lower post-orbital bar/ upper zygomatic region was also

consistent with strain orientation patterns in our *Pan* FEMs. We found little significance in trabecular material orientation: in *Pan*, primary orientation of trabecular bone was significantly oriented relative to the infero-superior axis, while in humans, primary trabecular orientation was significantly oriented 94 degrees from the antero-posterior axis. In our *Pan* FEMs, primary and secondary strain tensors appear to be undergoing a transition in orientation, which would predict greater variability of trabecular material orientation in this region. Furthermore, the greater anisotropy observed in the lower zygoma is consistent with a greater number of strain tensors with higher magnitudes of tension in this region compared to the upper zygoma.

Regarding interspecific difference in trabecular morphometry, we hypothesized that *Pan* zygomatic regions would be characterized by greater bone volume fraction, trabecular thickness, and high anisotropy. Our results support this hypothesis. We found that trabecular bone in the upper *Pan* zygoma is characterized by significantly higher bone volume fraction and trabecular thickness. Degree of anisotropy was higher in *Pan*, but this difference was not significant. The differences we observed between the lower zygomatic regions also support this hypothesis.

Currently, trabecular bone in the zygoma is being modeled as a solid region using isotropic elastic properties obtained from the human tibia (E=637 GPa, v=0.28) (13). The results of this study suggest that trabecular bone in the zygomatic region of humans and *Pan* differs drastically in bone type (as described by structure model index), density, trabecular thickness, and degree of anisotropy. Trabecular bone in the zygomatic region is more plate-like, has higher bone volume fraction, greater trabecular thickness, and

lower anisotropy (133). Determining the elastic properties of trabecular bone from the zygomatic region would be challenging, but replacing these values with more realistic ones would likely improve the reliability finite element analysis of the primate craniofacial skeleton. Furthermore, we found that 4 out of 5 of our *Pan* specimens did not have trabecular bone volumes in the zygomatic body. Zygomatic body trabecular regions in the four *Pan* finite element models were created from CT scans, however, the resolution of the CT scans may not have allowed proper determination of the size and extent of the trabecular region in the zygoma. It would be an important goal in the future to determine the extent of this variability across populations of *Pan*; perhaps, in *Pan* FEMs, the lower zygomatic body would be better modeled as a thick plate of bone with no trabecular volume.

Inter and Intraspecific Differences in Trabecular Morphometry

In primate postcranial regions, trabecular BVF, thickness, and separation increase with increasing body size, but with negative allometry (114). Patterns of trabecular bone morphometry were also observed to be related to taxonomic order, such that old world monkeys were found to have relatively thick and sparse trabeculae. Apes have a greater number of comparably thin, densely packed trabeculae. In this study, we found that some variables (BVF, trabecular number, and trabecular separation) differ significantly between species, while other variables (degree of anisotropy, connectivity density, and material density) differ significantly across anatomical locations. Consistent with previous studies, *Pan* had greater trabecular BVF, which was likely the result of a higher number of trabeculae with lower trabecular spacing. The statistically smaller BVF

found in our human sample is consistent with other human cranial and post-cranial regions where trabecular bone is approximately 50-75% the BVF of *Pan (91).*

Variables that were significantly different between species were not the same variables that we found to differ significantly between locations. Variables that differed significantly between human zygomatic locations included degree of anisotropy, connectivity density, and material density. This finding suggests that some morphometric variables are more likely influenced by systemic causes (like BVF), while others are more influenced by the local strain environment. This observation is useful for interpreting the meaning behind such variation. For example, if BVF is more of a systemic variable, then it may not be safe to assume that the resulting increase in strength due to increasing BVF is functionally significant. On the other hand, looking at changes in BVF of trabecular bone between regions of the same species may indicate that differences in BVF are perhaps related to function. In the case of the primate zygoma, increases in the BVF of trabecular bone regions in the lower zygoma that lead to completely dense zygomatic regions may allude to the functional need of the lower *Pan* zygoma to be stronger than the human zygoma, which has large, highly trabeculated lower zygomatic regions.

Material Orientation and Strain

Using finite element models of four *Pan* crania undergoing molar and premolar biting, we described primary, secondary, and tertiary strain orientations in upper and lower trabecular bone regions. We observed the following:

1. Working (biting) and resting (balancing) sides display differences in overall patterning of primary and secondary strain orientations.
2. Primary and secondary strain orientations on the working side are similar across all four models.
3. On the working side lower zygomatic region near the anterior root of the zygomatic arch we observed primary (tension) and secondary (compression) strain of a high magnitude lying in a transverse plane.
4. Moving laterally across the lower zygomatic region of the working side, primary and secondary strain tensors change such that primary strain is oriented in the medio-lateral direction and secondary strain is oriented in the supero-inferior direction and strain magnitudes decrease overall.
5. In the upper zygomatic region of the biting side, primary and secondary strain orientations are more variable. However, each lie nearly orthogonal to one another in the coronal plane, each approximately 45 degrees from the infero-superior axis.
6. The lower zygomatic body is characterized by strain of a higher magnitude compared to the upper zygomatic region. On the whole, this region has higher primary or tensile strain tensors than secondary or compressive strain tensors.

The relatively high degree and consistent medio-lateral orientation of tension across the lower zygoma would predict that this region of the zygoma should be characterized by higher anisotropy and that the primary eigenvector should lie in the medio-lateral direction and be much larger than secondary and tertiary eigenvectors. The results of our

μCT analysis are highly consistent with these predictions. One possible explanation for the thick cortical plate that characterized four out of five of our *Pan* specimens is that greater strain magnitudes that would be expected in *Pan* would lead to the filling in of bone in the coronal plane. Furthermore, we observed a transition in trabecular bone type moving latero-medially in most of our human sample, such that the thick coronally oriented plates found in the more lateral region of the zygomatic body thin out and become shorter in the more medial region of the zygomatic body. Compressive strain orientations in the supero-inferior direction forming in this region would predict this transition. The lack of significance in most of the angle orientations in the upper zygomatic region and the lack of consistency between human and *Pan* primary orientations would be predictable based on the variability of strain orientations in the *Pan* FEMs. Additionally, moderate and proportionate primary and secondary strain in this region predict that primary and secondary trabecular orientations would be similar in magnitude, as was observed.

Trabecular bone type in both upper and lower zygomatic regions was overall more plate-like. Plate-like trabecular bone structure has been observed in other regions of the primate craniofacial skeleton, including the mandibular condyle and the supraorbital region(135) (Pryor et al. in prep). In the supraorbital region and the mandibular condyle bony plates are oriented in the sagittal plane, whereas in the lower human zygomatic region, plates are observed in the medio-lateral direction, falling in the coronal plane. Furthermore, inconsistencies between the supraorbital and lower zygomatic region are found in the variability of each eigenvector. In the lower

zygomatic region, the primary eigenvector lying in the medio-lateral direction is the most consistent; in the supraorbital region, the medio-lateral eigenvector is also the most consistently oriented, however it comprised the tertiary eigenvector, which described the least amount of bony material. In both cases, the most consistent alignment occurs near to the direction of primary strain in the *Pan* FEMs. Giesen et al. (106) hypothesize that trabecular structure in the mandibular condyle, and inferably the supraorbital region, is adapted to endure low stress from multiple directions, as opposed to unidirectional loads of high magnitude as is observed in the zygoma (107,139). Our findings support this hypothesis, as we observed that trabecular bone orientation and anisotropy in the zygoma differs from that observed in the condyle and the supraorbital region.

Limitations

Our human sample contained more males than females and our chimp sample contained more females than males. We had at least three human individuals over the age of 70 (one individual's age was unknown), and one adult under the age of 40. We did not test the effects that age or sex played on the BVF of our sample (98,140-142). Because of our sample size, it was difficult to tell if the data was normally distributed. This led us to perform parametric statistics to decrease the likelihood of type 1 error.

Trabecular bone analysis is subject to oversampling error. Ideally, volumes of interest should therefore be scaled to body size (98). In this study, we were limited by small regions of trabecular bone and large interspecific variations in the amount of trabecular bone (such as between the lower human and *Pan* zygomatic regions). We therefore were not able to scale regions by body size, but instead analyzed all trabecular

bone within each region. While our volumes of interest were influenced by body size across the individual and species level (105,143), comparison of our trabecular VOIs and mean body size found large inconsistencies. This is likely attributable to differences in morphology between humans and *Pan:* for example, *Pan* upper zygoma regions were generally shorter than upper zygoma regions in humans. Trabecular volumes in the upper zygoma are fairly small and in some individuals it was difficult to determine the cortical and trabecular bone interface. We used a standard method of outlining trabecular regions, as described in our methods, to help cope with this limitation.

CHAPTER IV

OSTEOCYTE MORPHOLOGY IN HIGH AND LOW STRAIN REGIONS OF THE HUMAN AND *PAN* CRANIOFACIAL SKELETON

Synopsis

Differences in osteocyte morphology have been linked to mechanosensitivity in bone. This study used FITC staining and confocal microscopy to produce three-dimensional images of the osteocytic network within a high strain (anterior zygomatic root) and low strain (supraorbit) region of human and chimpanzee craniofacial bone. Osteonal osteocyte cell body surface area, volume, sphericity, and ellipsicity, and dendrite volume, length, diameter and branching point were characterized using Imaris. We hypothesized that low strain supraorbital regions of both species will contain more oblate, spherically shaped, smaller osteocytes with shorter, thicker dendritic processes relative to regions of higher strain (zygomatic). Our results found that human osteocytes in the supraorbit are significantly less oblate than those in the robust *Pan* supraorbital region and that osteocytes in the *Pan* supraorbital were significantly more oblate and spherical than in the zygoma. Also consistent with our hypothesis, we found that dendrites in the *Pan* supraorbit are significantly larger than those in the zygoma. Supraorbital osteocytes in both animals were larger in the supraorbital region compared to the zygoma. These results supply a possible mechanism of bone adaption that is consistent with studies that show that the low strained supraorbital region is sensitive to changes in orofacial function and offer a mechanistic explanation for systemic differences observed between humans and other primates.

Introduction

Osteocytes are the most abundant cells in bone. They are the terminal cells of osteoblastic differentiation; osteoblasts mature into osteocytes as they become embedded in the extracellular matrix during bone formation. Once the surrounding extracellular matrix mineralizes, osteocytes maintain an extensive network of connections, via their cell processes, called dendrites, to neighboring osteocytes, blood vessels, and bone lining cells. Osteocytes and their dendrites occupy un-mineralized cavities (lacunae) and canals (canaliculi) in the bone, which allow for nutrient exchange, movement of signaling factors, and interstitial fluid flow. It is the movement of interstitial fluid throughout these cavities and channels produced by strain that is believed to be the primary mechanism by which a mechanical stimulus is translated into a biological response via its effect on the osteocytic network (146). This living network encased in hard tissue enables osteocytes to be the orchestrators of bone remodeling, responsible for mechanosensation and transduction (9). Comparative morphological studies characterize variations in bone structure across individuals and species in order to understand functional adaptations. Since the mechanisms behind bone remodeling have not been well understood, little attention has been given to variations in bone at the cellular level that influence bone adaptation. By analyzing osteocyte density, cell body size and shape, and dendritic surface area, diameter, volume, length, size and branching, we can begin to address why species and location-specific differences exist systemically.

There seems to be a coupled relationship between strain environment and osteocyte morphology as mechanical loading has been related to osteocyte morphology

and osteocyte morphology has been related to its mechanosensitivity (147). Osteocyte shape, orientation, surface area, and volume; and dendritic process number, surface area and volume differ significantly by anatomical location and function (80-82). Fibular osteocytes are more aligned along orientations of primary strain throughout the entire fibula, which may be due to the ability of stress fibers to elongate in the direction of principle strains due to the application of tension on surface integrins (82). This observation is consistent with randomly oriented calvarial osteocytes, as this region of the skeleton is subjected to less direct loading, relative to the fibula. Furthermore, calvarial osteocytes in mice are more oblate and spherical, while long bone osteocytes are more oblong or prolate in shape. The multi-directional loading in the calvaria may lead to rounder, flatter osteocytes, while greater unidirectional loading in long bones may produce osteocytes elongated in one direction. Lending further support to the influence of mechanical loading on osteocyte morphology, 19 day old embryonic murine femoral osteocytes are more randomly oriented and irregularly shaped than osteocytes at 6 weeks of life, which become aligned with the major axis of strain orientation within the bone (longitudinally); likewise femora that developed without mechanical loading maintained random orientation and were more spherical in shape, contrasting with the flatter more spindle shaped osteocytes in murine femora under normal loading conditions (81). Cortical and cancellous bone, while both affected by mechanical loading, experience differences in the extent of network formation with regard to orientation, nuclear shape and branch formation, such that the number of cell processes of osteocytes in cancellous bone is not affected by mechanical loading, but the

elongation of cell processes, which is encouraged by mechanical loading was less extreme for trabecular bone than for cortical (81).

The relationship between osteocyte cellular morphology and mechanosensitivity has been studied in vitro. Along with prostaglandins, the endothelial isoform of nitric oxide synthase (eNOS) is a major regulator of bone formation; elevated levels of eNOS stimulate bone formation and suppress bone resorption (148). In vitro cells subjected to pulsating fluid flow released two times more nitric oxide and five times more prostaglandins than cells in a static environment (82,146,149). Furthermore, suspended round MLO-Y4 osteocytes, which are less stiff, under higher force produced more nitric oxide than flat osteocytes (137). The more spherical morphology of murine calvarial osteocytes then suggests that they are more sensitive to strain than the spindle-shaped fibular osteocytes. Greater sensitivity of calvarial osteocytes to strain would enable them to maintain a greater amount of bone in a low strain environment.

Calvarial osteocytes also possess lower surface area and volume relative to fibular osteocytes (80). The greater surface area and volume that characterizes fibular osteocytes is possibly related to their metabolic activity: larger cells accommodate larger organelles that are responsible for many bone metabolic processes (80). Dendritic processes in murine fibular osteocytes are longer than those in the calvaria, but are smaller in diameter and volume than calvarial osteocytes.

Primate craniofacial skeletal functional anatomy is one field in particular that could benefit from a greater understanding of variation at the cellular level. For example, strain gage analysis shows that during orofacial function, the supraorbital region in

primates endures less strain relative to other craniofacial regions, such as the zygoma and zygomatic arch (25). While the disparity in relative strain and the robust morphology that characterizes many primate species suggests that in some species this region may be "overbuilt" for orofacial function, cortical bone mechanical studies show that the bone material properties in this region are affected by orofacial function (34,150).

In this study, we characterize osteocyte morphology in Harversian bone, to include cell body surface area, volume, sphericity, and ellipsicity as well as dendrite process surface area, length, diameter, volume and branching number per cell in a high strain (anterior root of the zygoma) and a low strain (supraorbital) region of the craniofacial skeleton of five humans and five chimpanzees (including one bonobo). We analyzed 19-20 osteocytes per region, per sample, totaling approximately 200 chimpanzee osteocytes and 200 human osteocytes. We predict that supraorbital regions of both species will contain more spherically shaped, smaller osteocytes with thicker less oriented dendritic processes relative to regions of higher strain (zygomatic). We also predict that osteocytes in the chimpanzee, which are adapted to higher masticatory muscle force will display larger, less spherical osteocytes compared to comparable human regions.

Materials and Methods

Rectangular samples of cortical bone, measuring approximately one mm thick, four mm long, and three mm wide were cut using a Dremel hand piece in a transverse plane from the middle of the supraorbital region and the anterior root of the zygoma

from five humans and five *Pan*. Once cut, the five human samples (two females ages 21 and 39, three males ages 77, 54 and 1 of unknown age), four *Pan tryglodytes* (two adult females and two adult males) and one *Pan paniscus* (adult female) were kept in a solution of equal parts of isotonic saline and 95% ethanol. Our human sample came from the willed body program at the University of Texas Southwestern Medical Center. Our *Pan* sample were all captive animals and came from Yerkes Primate Center, the Southwest National Primate Center, and the Antwerp Zoo (the bonobo). We chose to use *Pan* as a comparison to humans due to their close genetic relationship and the potential for making deductions about fossil hominids.

Specimens were scanned at a resolution of 3.5 μm, an energy of 55 kVp, an angulation of 114 μA, and an integration time of 800 ms in solution at Baylor College of Dentistry in Dallas, Texas using a Scanco Medical μCT 35 (Scanco Medical, Basserdorf, Switzerland). For consistency, 1.5 mm regions along the long axis of each sample (along the transverse plane) were selected for scanning using a scoutview. Once scanned, circular regions of interest measuring 0.04 mm^2 were contoured on all 500 slices, 1.75 mm in length, within this selection, creating a cylindrical volume of interest. Analysis of this region produced bone volume fraction (BVF), and material and apparent density measured in mg of hydroxyapatite per mm^3.

Three-Dimensional Analysis of Osteocytes

Samples were dehydrated using increasing concentrations of ethanol, stained using fluorescein isothiocyanate isomer 1 (FITC) and embedded in methyl methacrylate. Once hardened, samples were cut into 100-200 micrometer thick sections using a slow

speed isomet saw and ground down to 40 to 70 micrometer thick sections. Sections were mounted on slides and observed and captured using our confocal microscopy system (Leica Microsystems). Captures consisting of osteonal osteocytes (osteocytes associated with an osteon, or Haversian canal) measured 0.228 by 0.228 by 0.49 (thickness) μm in resolution and consisted of approximately 70 to 100 slices (35-50 μm thick). Images were stored as .tiff files and imported into Imaris for segmentation and measurement.

Imaris software was used to render osteocytes and their dendritic processes and to characterize osteocyte cell body surface area, volume and shape and dendritic number, length, thickness, represented as an average per cell. Twenty cells were selected per sample for each analysis(151).

SPSS was used to test for significance in characteristics by region and species. Distribution of the data was observed along with the variation within each individual. We observed a non-normal distribution of data across some variables and when cells were averaged by individual. This led us to perform parametric statistics to decrease the likelihood of type 1 error. Mann-Whitney U tests were performed to look at both interspecific and intraspecific differences among cells. Cell body and dendrite measures were then averaged for each individual by region, producing a total of 20 values for each species and location. We compared average values by region.

Results

MicroCT Analysis

Table 4.1 provides the density results from the μCT analysis, including bone volume fraction, material density (measure of mg hydroxyapatite per mm^3 of only bone

voxels), and apparent density (measure of mg hydroxyapatite per mm^3 of bone and space voxels). Mann-Whitney-U tests found no significant differences between species and Wilcoxon tests found no significant differences between locations.

Imaris Analysis of Cell Bodies

We observed a lot of individual variation in bone quality among both our human and *Pan* samples, as is demonstrated by stacked confocal images in Figures 4-1 to 4-4. Some individuals had relatively dense osteocytic networks (Figure 4-1: A1, A2; Figure 4-2 A1 and A2), while others had sparse networks with seemingly little dendritic connection (Figure 4-3). These differences appeared to be consistent across both locations in these individuals. Figure 4-3 (A1 and A2) demonstrates the large periosteal fibers observed embedded in the osteons of several of the *Pan* individuals.

Analysis of osteocyte cell body size and shape produced values for each of 20 cells per region (2), per individual (10), totaling 200 measurements for the cell body surface area, cell body volume, cell body sphericity, and cell body ellipsicity, including a measure of ellipsicity, described as a degree of oblate and prolate (Table 4.2). An oblate ellipse is one in which the equatorial axis in longer than the polar axis, producing a disc-like shape. A prolate spheroid in one in which the polar axis is longer than the equatorial axis, producing a cigar-like shape. There was a large variation in cell body surface area and volume between individuals. Figure 4-4 shows box plot representations of mean values of cell body surface area (Figure 4A) and cell body volume (Figure 4-4B) averaged by individual. Mann-Whitney U tests performed on osteocyte cell body size and shape found that human supraorbital osteocytes have significantly greater surface

area ($p=0.015$), are less spherical ($p=0.001$) and more oblate ($p=0.005$) than osteocytes in the supraorbital region of *Pan* (Table 4.2). Osteocytes in the human zygoma compared to the human supraorbit were significantly larger (greater surface area ($p=0.005$) and volume ($p=0.010$)) and were significantly more oblate ($p\leq0.001$) and less prolate ($p=0.006$) (Table 4.2). When cells were averaged by individual, all *Pan* supraorbital regions contained more oblate cells relative to their zygomatic regions. Individual cell means for prolate were higher in one specimen and approximately equivalent in the remaining four.

We observed large variation in sphericity across the sample when cell values were average by individual (Figure 4-5A) and large individual cell variation of measure of sphericity, especially in *Pan* (Figure 4-5B). When cells were averaged by individual, sphericity was much greater in the supraorbit compared to the zygoma in two of the *Pan* individuals and approximately equivalent in the remaining three *Pan* individuals. Cells averaged by individual in the human sample revealed approximately equivalent values of sphericity across all individuals. Cells in both species and in both regions were mostly spherical in shape.

Mann-Whitney tests performed on osteocyte cell body size and shape between locations found significant differences between locations. In humans, osteocytes in the supraorbital region were significantly more oblate compared to those in the human zygoma ($p=0.021$) (Table 4.2). Osteocytes in the *Pan* supraorbital region were significantly larger (greater surface area $p=0.007$ and volume $p= 0.001$) and more oblate ($p\leq0.001$) than those in the *Pan* zygoma (Table 4.2). Homogeneity of shape between

human supraorbital and zygomatic osteocytes can be observed in Figure 4-6. More oblate, spherical osteocytes in the *Pan* supraorbital region are easily observable in Figure 4-7.

Imaris Analysis of Dendrites

Analysis of dendrites produced mean values for each of 20 cells per region (2), per individual (10), totaling 200 measurements for each value: mean dendrite surface area, mean dendrite length, mean dendrite diameter, mean dendrite volume, and mean dendrite branching number (Table 4.3). Most measures displayed close to a normal distribution, but some were skewed. Mann-Whitney U tests found that dendrites in the human supraorbit have a significantly greater average diameter ($p=0.003$) and average volume ($p=0.029$) (Table 4.3). Dendrites in the human zygoma differed significantly from dendrites in the *Pan* Zygoma in every measure of dendrite geometry ($p \leq 0.001$ for all) (Table 4.3). Human dendrites in the zygoma have greater mean surface area, length, diameter, and volume, and have less branching than dendrites in the *Pan* zygoma (Table 4.3).

Mann-Whitney tests between regions found no significant differences between the human supraorbit and zygoma, but did detect significant differences in all dendrite measures between the *Pan* supraorbit and zygoma (all p=0.000) (Table 4.3). Similar to the differences observed between the human and *Pan* zygomatic dendrites, *Pan* supraorbit dendrites are larger, with a greater surface area, diameter, length, and volume, but have less branching than *Pan* zygomatic dendrites (Table 4.3).

Discussion

Summary of Results

In this study, we used FITC staining and confocal microscopy to produce three-dimensional images of the osteocytic network within a high strain (anterior zygomatic root) and low strain (supraorbit) region of human and chimpanzee bone. We then characterized osteonal osteocyte morphology using Imaris, to include cell body surface area, volume, sphericity, and ellipsicity as well as dendrite process average number, length, diameter, and branching per cell. We hypothesized that supraorbital regions of both species will contain more oblate, spherically shaped, smaller osteocytes with shorter, thicker dendritic processes relative to regions of higher strain (zygomatic). We also predicted that osteocytes in the chimpanzee, which are adapted to higher masticatory muscle force will display larger, less spherical osteocytes compared to human regions. In summary, we found that osteocyte morphology differed significantly between species and between regions. Measures of cell body shape were consistent with our hypotheses: human osteocytes in the supraorbit are less spherical than those in the robust *Pan* supraorbital region, and although not found significant by our Mann-Whitney U test, osteocytes in the *Pan* supraorbital were on average more spherical than in the zygoma.

Osteocytes differed significantly in measures of ellipsicity. Osteocytes in the *Pan* supraorbit were significantly more oblate compared to those in the zygoma. Furthermore, cell averages for each *Pan* supraorbit were more oblate than osteocytes in the corresponding zygoma. Although, on the whole osteocytes in both regions and

species were more spherical, their tendency towards an oblate shape in the *Pan* supraorbit may cause them to be more mechanosensitive, and could also be influenced by low strains in this region.

We also found that osteocytes in the *Pan* supraorbital region have significantly larger diameters, and overall larger dendrites than those in the zygoma and that human supraorbital dendrites have a significantly larger diameters than human zygomatic dendrites.

Inconsistent with our predictions, osteocytes in the supraorbital region were larger than those in the zygoma and dendritic process were longer in the supraorbital region in both species (significantly longer in the *Pan* supraorbit). Furthermore, human osteocytes in both regions were larger than in corresponding *Pan* osteocytes. Studies that we reviewed in this paper that looked at osteocyte size found that high strained osteocytes in post cranial regions were larger than those in low strained calvarial regions in rats, suggesting that the larger post cranial cells are more metabolically active. From our results, it should be considered that human osteocytes and supraorbital osteocytes may be more metabolically active than their counterparts.

Function of the Supraorbit and Zygoma

The anterior root of the zygoma serves as an attachment site for the masseter muscle on its lower border and the temporalis fascia on its upper border. During incision and mastication, it is subjected to high strain, which is likely why there is high variability in its gross anatomy across primate species (16). The supraorbital region, or browridge is also highly variable in robusticity and projection across primate species, but

for less obvious reasons. Because the browridge endures relatively little strain during orofacial function, some have suggested that the browridge in many species is overbuilt for orofacial function (28). Others have lent strong support for browridge robusticity as an adaptation of protection against blows to the face (136), as a product of sphenoid length (21) and skull size (83). However, other studies suggest that cortical bone in the supraorbital region in humans is at least in part responsive to orofacial function (34,150). These studies call into question the assumption that supraorbital and zygomatic regions are equally responsive to peak strains induced by mastication.

Most vertebrate bone remodels to maintain strain levels between 100 and 1500 microstrain (48). Peak strains for vertebrate long bones during vigorous activity typically range between 2000 and 3000 microstrain (31,49). The bone remodeling response has been described as a "mechanostat," in which bone mass is determined through a mechanical feedback system under the regulation of hormones and other signaling molecules, suggesting that the minimum effective strain (MES) required to induce a remodeling response may be controlled at the cellular level. Terminal bone mass is not only a product of the local strain environment, but also affected by the temporal sequence of loading (50). This effect has been observed in rat tibia where there is a greater bone remodeling response to an initially large mechanical load which trails off compared to an initially small load which grows in magnitude (51). Therefore the MES required to incite remodeling in the supraorbital region could be lower than in the high strained zygoma in order to maintain a certain amount of bone in the region for either orofacial function or other purposes not even related to biting and mastication

(10,50,51). Recent studies on osteocyte morphology have found differences in osteocyte morphology between high and low strain regions in rats, suggesting a mechanism of control for MES that may underlie region and species-specific variations in the bone remodeling response and may explain the large variation in strain across the primate craniofacial skeleton (80,81).

The results of this study support the hypothesis that the supraorbital region is more sensitive to strain than the zygomatic region and that the robust *Pan* supraorbital region is more sensitive to strain than the human supraorbital region. These results are consistent with other studies that show a relationship between the strain environment and osteocyte shape: multi-directional low strains in the supraorbital region may produce rounder more oblate osteocytes with thicker dendritic processes. Furthermore, these results offer a possible mechanism of adaptation that are consistent with studies that show that the supraorbital region is sensitive to low strains produced by orofacial function, but does not eliminate alternative explanations of its adaptive significance. Differences in osteocyte morphology offer a mechanistic explanation for the robust supraorbital region in primates as well as a possible mechanistic explanation for the gracilization of the human skeleton.

Conclusion

Many studies compare differences in gross morphology to gain an understanding of the functional significance of morphological variation. We know that bone is a highly responsive living tissue, but little attention has been given to individual, regional, and species-specific variations that affect bone adaptation and the mechanisms that control

systemic differences. One such mechanism is the modification of the morphology of the mechanosensors of bone: the osteocyte. The method employed in this study allows for three-dimensional visualization of the osteocytic network without decalcification of the surrounding mineral. It is important that future studies characterize species and location-specific differences as well as observe sex and age related differences, in order that differences in gross morphology be interpreted with greater precision. Furthermore, this process has a lot to offer in studies of bone degeneration and disease. In conclusion, our results support the hypothesis that craniofacial adaption in humans, chimpanzees, and most likely extinct hominids is not simply reducible to a form equals function relationship, but influenced by systemic differences in cellular morphology, and more specifically, that differences in osteocyte cell body shape and dendritic processes have a direct effect on primate craniofacial adaptation.

CHAPTER V

SUMMARY

The complexity and variation observed among the primate craniofacial skeleton has perplexed functional morphologists and paleoanthropologists who wish to understand the adaptational significance of such variation. Some have turned to FEA (1,2,11,108,109,152-154) as a way to test hypotheses regarding the effect of morphological variation during orofacial function. Finite element analysis is an engineering method that allows for the modeling of complex shapes. It requires the input of realistic values of bone material properties, such as elastic modulus, as well as muscle fiber orientation and magnitude of muscle force (3-7). Finite element models of primate craniofacial bone model supraorbital and zygomatic trabecular regions as solid bodies with elastic properties obtained from trabecular bone within the human tibia (8). The results of this study found that cranial trabecular regions differ substantially in morphology from post-cranial regions, across species, and across subregions of the cranial skeleton. The incorporation of more realistic mechanical properties of trabecular bone may improve the accuracy of finite element models of the craniofacial skeleton. Determining the mechanical properties of trabecular bone in the craniofacial skeleton of primates has it challenges. This study found that trabecular regions are often very small, making it difficult to obtain samples of trabecular bone that are large enough to acquire reliable material properties.

A promising technique for the determination of the mechanical properties of trabecular bone is micro-computed tomography, which can now be used to acquire direct

three-dimensional visualization of bone under mechanical loading (150,151). This technique, called image guided failure assessment (IGFA) goes beyond micro-finite element modeling, which looks at bone behavior within the elastic region of deformation, by quantifying bone mechanical properties within the plastic region of deformation, allowing for visualization of trabecular bone under buckling and bending, fracture initiation and propagation, and damage accumulation. This micro-mechanical testing system was first developed by Muller et al. (152) and Nazarian and Muller (150) specifically for measuring loaded porous material using μCT. It is composed of a micro-compression devise (MCD) and a material testing and data acquisition (MTDAQ) system. In the pilot study by Muller et al. (152), the bone sample is first measured with a 10 N pre-load, applied by a servo-hydraulic testing machine that facilitates the application of fixed boundary conditions, serving as a time zero control measurement. Then, a load displacement curve is generated by measuring the distance between load platens from the scoutview from three loading steps at 1%, 2% and 4% strain. For each loading step, a three-dimensional scan or "snapshot" of the sample is created, with the displacement locked by a cap-screw. This particular study yielded interesting results: more rod-like trabecular bone from bovine tibiae and whale spine undergoes buckling and bending before failure, whereas more plate-like trabecular bone seems to undergo instantaneous failure. There are innumerable ways to apply this method to understanding the functional significance of trabecular bone type across the craniofacial skeleton, aside from its usefulness in determining mechanical properties.

In addition to improving the accuracy of finite element models, an observation of the intraspecific and interspecific variation of trabecular bone morphometry in the primate craniofacial skeleton provides a unique insight on the adaptation of isolated regions. This study found that subcortical bone regions in the supraorbit consist of highly dense, sagittally oriented plates and that bone orientation is consistent across multiple species. Observations of high anisotropy and a highly consistent tertiary vector orientation support the hypothesis that this region is possibly responsive to strain induced by oral function. However, primary and secondary orientations observed in this region across species supports the hypothesis that bone is possibly well suited for resisting external superoinferiorly and anteroposteriorly directed forces, thusly supporting the facial buttressing hypothesis. Also consistent with our findings is the hypothesis that trabecular bone in this region is adapted to a wide variation of strain orientations applied across the region during mastication and incision (136).

In the fourth chapter of this work, morphological differences at the cellular level are described as they may influence bone's sensitivity to strain. The results of this study determined that osteocytes in the cortical bone of the *Pan* supraorbit are significantly more spherical and oblate compared to those in the *Pan* zygoma, and osteocytes in the more gracile human supraorbit are less spherical and significantly less oblate. These results provide a possible mechanism that would explain systemic differences found in robust species. These results also provide a mechanism for bone adaptation that would allow low strain regions in the craniofacial skeleton to be relatively more responsive to strain. In the future, it is important to characterize differences in trabecular bone

osteocyte morphology in the supraorbit to see if it is also possibly more sensitive to strain, as well as to look for morphological differences that might create differences in sensitivity between trabecular and cortical bone.

Trabecular bone morphometry in the high strained zygoma also differs from post-cranial regions and differs from trabecular bone morphometry in the browridge. Trabecular bone in the zygoma consists of coronally oriented plates in the lateral aspect of the bone, near the anterior root, and more sparse rod-like bone in the medial aspect, near the lateral wall of the nasal aperture. Great interspecific variation was observed, as there was little to no trabecular bone in 4 of the 5 *Pan* specimens in the lower zygomatic region. Furthermore, trabecular morphology observed in the lower human zygoma, unlike in the browridge, is highly consistent with strain orientation observed in the *Pan* finite element models, and trabecular morphometry and patterns of anisotropy are also consistent.

Considering trabecular bone morphometry in both the supraorbit and zygoma regions suggests that the morphology of the high strain zygoma is far more influenced by mechanical loading from biting than the browridge. Osteocytes in the cortical bone of the anterior root of the *Pan* zygoma appear to be adapted to higher levels of strain, as they are characterized by smaller dendritic processes and are more prolate in shape relative to those in the supraorbit- a relationship that resembles that observed between high strain long bone and low strain calvarial bone in mice. Comparing the sphericity and dendritic size of human osteocytes between the zygoma and the long bone will offer

insight into differences between mechanosensitivity in cranial and post cranial regions and is therefore important to an overarching interpretation of craniofacial adaptation.

Understanding variation at the microstructural and cellular level is critical to the interpretation of variations in gross bone structure. The most prolific cell in bone, the osteocyte, is both adaptive to local strains and the primary mechanosensor of bone, responsible for detecting and transmitting strain signals in bone by releasing prostaglandins and nitric oxide (9). In this assessment of the osteocyte network within human and *Pan* low and high strain regions of cortical bone, we found significant differences with translatable implications for region and species-specific differences in the adaptive response of bone. From these results, we have acquired a possible mechanism for systemic differences in bone density between humans and *Pan*. Comparing osteocyte morphology across other primate species would be useful in corroborating these results. As a relatively new and unexplored territory of bone research, little is known about species and location-specific variation in osteocyte morphology and how morphology is affected by local strain patterns. These results demonstrated high variation in cellular morphology as whole. Future studies could evaluate greater numbers of osteocytes across many regions to get a whole picture of the individual variation in cellular morphology in difference species. In conclusion, the results presented here offer a unique insight regarding the significance of the variations in primate craniofacial skeleton and highlight the high degree of variation in morphology between species, between location, and between individuals on both the microscopic and macroscopic level.

REFERENCES

1. Richmond, B. G., Wright, B. W., Grosse, I., Dechow, P. C., Ross, C. F., Spencer, M. A., and Strait, D. S. (2005) Finite element analysis in functional morphology. *Anat Rec A Discov Mol Cell Evol Biol* **283A**, 259-274
2. Strait, D. S., Grosse, I. R., Dechow, P. C., Smith, A. L., Wang, Q., Weber, G. W., Neubauer, S., Slice, D. E., Chalk, J., Richmond, B. G., Lucas, P. W., Spencer, M. A., Schrein, C., Wright, B. W., Byron, C., and Ross, C. F. (2010) The structural rigidity of the cranium of *Australopithecus africanus*: implications for diet, dietary adaptations, and the allometry of feeding biomechanics. *Anat Rec* **293**, 583-593
3. Dechow, P. C., Nail, G. A., Schwartzdabney, C. L., and Ashman, R. B. (1993) Elastic properties of human supraorbital and mandibular bone. *Am J Phys Anthropol* **90**, 291-306
4. Peterson, J., and Dechow, P. C. (2003) Material properties of the human cranial vault and zygoma. *Anat Rec Part A* **274A**, 785-797
5. Peterson, J., Wang, Q., and Dechow, P. C. (2006) Material properties of the dentate maxilla. *Anat Rec A Discov Mol Cell Evol Biol* **288**, 962-972
6. Wang, Q., Strait, D. S., and Dechow, P. C. (2006) A comparison of cortical elastic properties in the craniofacial skeletons of three primate species and its relevance to the study of human evolution. *J Hum Evol* **51**, 375-382
7. Strait, D. S., Wang, Q., Dechow, P. C., Ross, C. F., Richmond, B. G., Spencer, M. A., and Patel, B. A. (2005) Modeling elastic properties in finite-element

analysis: how much precision is needed to produce an accurate model? *Anat Rec A Discov Mol Cell Evol Biol* **283**, 275-287

8. Strait, D. S., Weber, G. W., Neubauer, S., Chalk, J., Richmond, B. G., Lucas, P. W., Spencer, M. A., Schrein, C., Dechow, P. C., Ross, C. F., Grosse, I. R., Wright, B. W., Constantino, P., Wood, B. A., Lawn, B., Hylander, W. L., Wang, Q., Byron, C., Slice, D. E., and Smith, A. L. (2009) The feeding biomechanics and dietary ecology of *Australopithecus africanus*. *Proceedings of the National Academy of Sciences of the United States of America* **106**, 2124-2129

9. Bonucci, E. (2009) The osteocyte: the underestimated conductor of the bone orchestra. *Rendiconti Lincei-Scienze Fisiche E Naturali* **20**, 237-254

10. Kupczik, K., Dobson, C. A., Crompton, R. H., Phillips, R., Oxnard, C. E., Fagan, M. J., and O'Higgins, P. (2009) Masticatory loading and bone adaptation in the supraorbital torus of developing macaques. *Am J Phys Anthropol* **139**, 193-203

11. Strait, D. S., Richmond, B. G., Spencer, M. A., Ross, C. F., Dechow, P. C., and Wood, B. A. (2007) Masticatory biomechanics and its relevance to early hominid phylogeny: An examination of palatal thickness using finite-element analysis. *J Hum Evol* **52**, 585-599

12. Wang, Q., Dechow, P. C., Richmond, B. G., Ross, C. F., Spencer, M. A., Strait, D. S., and Wright, B. W. (2006) Fusion of craniofacial sutures in monkey skulls with special reference to the finite-element analysis. *Am J Phys Anthropol*, 184-185

13. Ashman, R. B., Rho, J. Y., and Turner, C. H. (1989) Anatomical variation of orthotropic elastic moduli of the proximal human tibia. *J Biomech* **22**, 895-900

14. Panagiotopoulou, O., Curtis, N., O'Higgins, P., and Cobb, S. N. (2010) Modelling subcortical bone in finite element analyses: A validation and sensitivity study in the macaque mandible. *J Biomech* **43**, 1603-1611

15. Harrigan, T. P., Jasty, M., Mann, R. W., and Harris, W. H. (1988) Limitations of the continuum assumption in cancellous bone. *J Biomech* **21**, 269-275

16. Ross, C. F., Berthaume, M. A., Dechow, P. C., Iriarte-Diaz, J., Porro, L. B., Richmond, B. G., Spencer, M., and Strait, D. (2011) In vivo bone strain and finite-element modeling of the craniofacial haft in catarrhine primates. *J Anat* **218**, 112-141

17. Endo, B. (1970) Analysis of stresses around the orbit due to masseter and temporalis muscles respectively. *Jounral of the Anthropological Society of Nippon* **78**, 251-266

18. Smith, A. L., Benazzi, S., Ledogar, J. A., Tamvada, K., Pryor Smith, L. C., Weber, G. W., Spencer, M. A., Dechow, P. C., Grosse, I. R., Ross, C. F., Richmond, B. G., Wright, B. W., Wang, Q., Byron, C., Slice, D. E., and Strait, D. S. (2015) Biomechanical implications of intraspecific shape variation in chimpanzee crania: moving toward an integration of geometric morphometrics and finite element analysis. *Anat Rec* **298**, 122-144

19. Smith, A. L., Benazzi, S., Ledogar, J. A., Tamvada, K., Pryor Smith, L. C., Weber, G. W., Spencer, M. A., Lucas, P. W., Michael, S., Shekeban, A., Al-

Fadhalah, K., Almusallam, A. S., Dechow, P. C., Grosse, I. R., Ross, C. F., Madden, R. H., Richmond, B. G., Wright, B. W., Wang, Q., Byron, C., Slice, D. E., Wood, S., Dzialo, C., Berthaume, M. A., van Casteren, A., and Strait, D. S. (2015) The feeding biomechanics and dietary ecology of *Paranthropus boisei*. *Anat Rec* **298**, 145-167

20. Russell, M. D. (1985) The supraorbital torus - A most remarkable peculiarity. *Current Anthropology* **26**, 337-360

21. Lieberman, D. E. (1998) Sphenoid shortening and the evolution of modern human cranial shape. *Nature* **393**, 158-162

22. Tappen, N. C. (1973) Structure of bone in the skulls of Neanderthal fossils. *Am J Phys Anthropol* **38**, 93-97

23. Weidenreich, F. (1946) *Apes, giants and man*, The University of Chicago Press, Chicago, Ill.,

24. Ravosa, M. J. (1991) Interspecific perspective on mechanical and nonmechanical models of primate circumorbital morphology. *Am J Phys Anthropol* **86**, 369-396

25. Picq, P. G., and Hylander, W. L. (1989) Endo stress-analysis of the primate skull and the functional significance of the supraorbital region. *Am J Phys Anthropol* **79**, 393-398

26. Hylander, W. L., and Picq, P. G. (1989) A review of Endo's stress-analysis of the primate skull. *Am J Phys Anthropol* **78**, 243-244

27. Hylander, W. L., Picq, P. G., and Johnson, A. D. (1987) A preliminary stress-analysis of the circumorbital region in *Macaca fascicularis*. *Am J Phys Anthropol* **72**, 214-214

28. Hylander, W. L., Picq, P. G., and Johnson, K. R. (1991) Masticatory-stress hypotheses and the supraorbital region of primates. *Am J Phys Anthropol* **86**, 1-36

29. Endo, B. (1966) Experiemental studies on the mechanical significance of the form of the human facial skeleton. *Journal of the Faculty of Science, University of Tokyo* **3**, 5-106

30. Currey, J. D. (2002) *Bones: Structure and Function*, Princeton University Press, New Jersey

31. Martin, R. B., Burr, D. B., and Sharkey, N. A. (1998) *Skeletal Tissue Mechanics*, Springer, New York

32. Evans, F. G. (1973) *Mechanical properties of bone*, Thomas, Springfield, Ill.,

33. Guo, X. E. (2001) Mechanical properties of cortical bone and cancellous bone tissue. in *Bone Biomechanics Handbook* (Cowin, S. C. ed.), 2nd Ed., CRC Press, Boca Raton. pp

34. Dechow, P. C., Wang, Q., and Peterson, J. (2010) Edentulation alters material properties of cortical bone in the human craniofacial skeleton: functional implications for craniofacial structure in primate evolution. *Anat Rec* **293**, 618-629

35. Wang, Q., and Dechow, P. C. (2006) Elastic properties of external cortical bone in the craniofacial skeleton of the rhesus monkey. *Am J Phys Anthropol* **131**, 402-415

36. Carter, D., and Hayes, W. (1977) The compressive behavior of bone as a two-phase porous structure. *The Journal of Bone and Joint Surgery* **59**, 954-962

37. Rice, J. C., Cowin, S. C., and Bowman, J. A. (1988) On the dependence of the elasticity and strength of cancellous bone on apparent density. *J Biomech* **21**, 155-168

38. Ulrich, D., van Rietbergen, B., Laib, A., and Ruegsegger, P. (1999) The ability of three-dimensional structural indices to reflect mechanical aspects of trabecular bone. *Bone* **25**, 55-60

39. Morgan, E. F., Bayraktar, H. H., and Keaveny, T. M. (2003) Trabecular bone modulus-density relationships depend on anatomic site. *J Biomech* **36**, 897-904

40. Feldkamp, L. A., Goldstein, S. A., Parfitt, A. M., Jesion, G., and Kleerekoper, M. (1989) The direct examination of three-dimensional bone architecture in vitro by computed tomography. *J Bone Miner Res* **4**, 3-11

41. Ruegsegger, P. (2001) Imaging of bone structure. in *Bone Mechanics Handbook* (Cowin, S. C. ed.), CRC Press, Boca Raton. pp

42. Goulet, R. W., Goldstein, S. A., Ciarelli, M. J., Kuhn, J. L., Brown, J. H., and Feldkamp, L. A. (1994) The relationship between the structural and orthogonal compressive properties of trabecular bone. *J Biomech* **27**, 375-389

43. Laib, A., Barou, O., Vico, L., Lafage-Proust, M. H., Alexander, C. E., and Rugsegger, P. (2000) 3D micro-computed tomography of trabecular and cortical bone architecture with application to a rat model of immobilisation osteoporosis. *Medical and Biological Engineering and Computing* **38**, 326-332

44. MacLatchy, L., and Muller, R. (2002) A comparison of the femoral head and neck trabecular architecture of Galago and Perodicticus using micro-computed tomography (mu CT). *J Hum Evol* **43**, 89-105

45. Fajardo, R. J., Muller, R., Ketcham, R. A., and Colbert, M. (2007) Nonhuman anthropoid primate femoral neck trabecular architecture and its relationship to locomotor mode. *Anat Rec* **290**, 422-436

46. Griffin, N. L., D'Aout, K., Ryan, T. M., Richmond, B. G., Ketcham, R. A., and Postnov, A. (2010) Comparative forefoot trabecular bone architecture in extant hominids. *J Hum Evol* **59**, 202-213

47. Ryan, T. M., and Ketcham, R. A. (2005) Angular orientation of trabecular bone in the femoral head and its relationship to hip joint loads in leaping primates. *J Morphol* **265**, 249-263

48. Frost, H. M. (1987) Bone "mass" and the "mechanostat": a proposal. *Anat Rec* **219**, 1-9

49. Rubin, C. T., and Lanyon, L. E. (1984) Regulation of bone-formation by applied dynamic loads. *Journal of Bone and Joint Surgery-American Volume* **66A**, 397-402

50. Turner, C. H. (1999) Torward a mathematical description of bone biology: The principle of cellular accomodation. *Calcified Tissue International* **65**, 466-471

51. Schriefer, J. L., Warden, S. J., Saxon, L. K., Robling, A. G., and Turner, C. H. (2005) Cellular accommodation and the response of bone to mechanical loading. *J Biomech* **38**, 1838-1845

52. Kim, C. H., Takai, E., Zhou, H., von Stechow, D., Muller, R., Dempster, D. W., and Guo, X. E. (2003) Trabecular bone response to mechanical and parathyroid hormone stimulation: the role of mechanical microenvironment. *J Bone Miner Res* **18**, 2116-2125

53. Parfitt, A. M. (1979) Quantum concept of bone remodeling and turnover: implications for the pathogenesis of osteoporosis. *Calcif Tissue Int* **28**, 1-5

54. Hadjidakis, D. J., and Androulakis, II. (2006) Bone remodeling. *Ann N Y Acad Sci* **1092**, 385-396

55. Currey, J. D. (2002) *Bones: Structure and Mechanics*, Princeton University Press

56. Singh, I. (1978) Architecture of cancellous bone. *J Anat* **127**, 305-310

57. Cheng, B., Zhao, S., Luo, J., Sprague, E., Bonewald, L. F., and Jiang, J. X. (2001) Expression of functional gap junctions and regulation by fluid flow in osteocyte-like MLO-Y4 cells. *J Bone Miner Res* **16**, 249-259

58. Bonewald, L. F., and Johnson, M. L. (2008) Osteocytes, mechanosensing and Wnt signaling. *Bone* **42**, 606-615

59. Holmen, S. L., Zylstra, C. R., Mukherjee, A., Sigler, R. E., Faugere, M. C., Bouxsein, M. L., Deng, L., Clemens, T. L., and Williams, B. O. (2005) Essential role of beta-catenin in postnatal bone acquisition. *J Biol Chem* **280**, 21162-21168

60. Day, T. F., Guo, X., Garrett-Beal, L., and Yang, Y. (2005) Wnt/beta-catenin signaling in mesenchymal progenitors controls osteoblast and chondrocyte differentiation during vertebrate skeletogenesis. *Dev Cell* **8**, 739-750

61. Glass, D. A., 2nd, Bialek, P., Ahn, J. D., Starbuck, M., Patel, M. S., Clevers, H., Taketo, M. M., Long, F., McMahon, A. P., Lang, R. A., and Karsenty, G. (2005) Canonical Wnt signaling in differentiated osteoblasts controls osteoclast differentiation. *Dev Cell* **8**, 751-764

62. Kramer, I., Halleux, C., Keller, H., Pegurri, M., Gooi, J. H., Weber, P. B., Feng, J. Q., Bonewald, L. F., and Kneissel, M. (2010) Osteocyte Wnt/β-Catenin signaling is required for normal bone homeostasis. *Molecular and Cellular Biology* **30**, 3071-3085

63. Fisher, L. W., Torchia, D. A., Fohr, B., Young, M. F., and Fedarko, N. S. (2001) Flexible structures of SIBLING proteins, bone sialoprotein, and osteopontin. *Biochem Biophys Res Commun* **280**, 460-465

64. Hirst, K. L., Ibaraki-O'Connor, K., Young, M. F., and Dixon, M. J. (1997) Cloning and expression analysis of the bovine dentin matrix acidic phosphoprotein gene. *Journal of Dental Research* **76**, 754-760

65. Terasawa, M., Shimokawa, R., Terashima, T., Ohya, K., Takagi, Y., and Shimokawa, H. (2004) Expression of dentin matrix protein 1 (DMP1) in nonmineralized tissues. *J Bone Miner Metab* **22**, 430-438

66. George, A., Sabsay, B., Simonian, P. A., and Veis, A. (1993) Characterization of a novel dentin matrix acidic phosphoprotein. Implications for induction of biomineralization. *J Biol Chem* **268**, 12624-12630

67. Qin, C., Brunn, J. C., Cook, R. G., Orkiszewski, R. S., Malone, J. P., Veis, A., and Butler, W. T. (2003) Evidence for the proteolytic processing of dentin matrix protein 1. Identification and characterization of processed fragments and cleavage sites. *J Biol Chem* **278**, 34700-34708

68. Lu, Y., Yuan, B., Qin, C., Cao, Z., Xie, Y., Dallas, S. L., McKee, M. D., Drezner, M. K., Bonewald, L. F., and Feng, J. Q. (2011) The biological function of DMP-1 in osteocyte maturation is mediated by its 57-kDa C-terminal fragment. *J Bone Miner Res* **26**, 331-340

69. Qin, C., D'Souza, R., and Feng, J. Q. (2007) Dentin matrix protein 1 (DMP1): new and important roles for biomineralization and phosphate homeostasis. *Journal of Dental Research* **86**, 1134-1141

70. Feng, J. Q., Huang, H., Lu, Y., Ye, L., Xie, Y., Tsutsui, T. W., Kunieda, T., Castranio, T., Scott, G., Bonewald, L. B., and Mishina, Y. (2003) The dentin matrix protein 1 (Dmp1) is specifically expressed in mineralized, but not soft, tissues during development. *Journal of Dental Research* **82**, 776-780

71. Feng, J. Q., Ward, L. M., Liu, S., Lu, Y., Xie, Y., Yuan, B., Yu, X., Rauch, F., Davis, S. I., Zhang, S., Rios, H., Drezner, M. K., Quarles, L. D., Bonewald, L. F., and White, K. E. (2006) Loss of DMP1 causes rickets and osteomalacia and identifies a role for osteocytes in mineral metabolism. *Nat Genet* **38**, 1310-1315

72. Ling, Y. (2005) DMP1 depletion decreases bone mineralization in vivo: an FTIR imaging analysis. *J Bone Miner Res* **20**, 2169-2177

73. Zhang, R., Lu, Y., Ye, L., Yuan, B., Yu, S., Qin, C., Xie, Y., Gao, T., Drezner, M. K., Bonewald, L. F., and Feng, J. Q. (2011) Unique roles of phosphorus in endochondral bone formation and osteocyte maturation. *J Bone Miner Res* **26**, 1047-1056

74. Gluhak-Heinrich, J., Ye, L., Bonewald, L. F., Feng, J. Q., MacDougall, M., Harris, S. E., and Pavlin, D. (2003) Mechanical loading stimulates dentin matrix protein 1 (DMP1) expression in osteocytes in vivo. *J Bone Miner Res* **18**, 807-817

75. Rodan, G., and Martin, T. (1981) Role of osteoblasts in hormonal control of bone resorption—A hypothesis. *Calcified Tissue International* **33**, 349-351

76. Suda, T., Takahashi, N., Udagawa, N., Jimi, E., Gillespie, M. T., and Martin, T. J. (1999) Modulation of osteoclast differentiation and function by the new members of the tumor necrosis factor receptor and ligand families. *Endocrine Reviews* **20**, 345-357

77. Hikita, A., Yana, I., Wakeyama, H., Nakamura, M., Kadono, Y., Oshima, Y., Nakamura, K., Seiki, M., and Tanaka, S. (2006) Negative regulation of

osteoclastogenesis by ectodomain shedding of receptor activator of NF-kappaB ligand. *J Biol Chem* **281**, 36846-36855

78. You, L., Temiyasathit, S., Lee, P., Kim, C. H., Tummala, P., Yao, W., Kingery, W., Malone, A. M., Kwon, R. Y., and Jacobs, C. R. (2008) Osteocytes as mechanosensors in the inhibition of bone resorption due to mechanical loading. *Bone* **42**, 172-179

79. Burger, E. H. (2002) Experiments of cell mechanosensitivity: Bone cells as mechanical engineers. in *Bone Mechanics Handbook* (Cowin, S. C. ed.), CRC Press, Boca Raton. pp

80. Himeno-Ando, A., Izumi, Y., Yamaguchi, A., and Iimura, T. (2012) Structural differences in the osteocyte network between the calvaria and long bone revealed by three-dimensional fluorescence morphometry, possibly reflecting distinct mechano-adaptations and sensitivities. *Biochemical and Biophysical Research Communications* **417**, 765-770

81. Sugawara, Y., Ando, R., Kamioka, H., Ishihara, Y., Honjo, T., Kawanabe, N., Kurosaka, H., Takano-Yamamoto, T., and Yamashiro, T. (2011) The three-dimensional morphometry and cell-cell communication of the osteocyte network in chick and mouse embryonic calvaria. *Calcif Tissue Int* **88**, 416-424

82. Vatsa, A., Breuls, R. G., Semeins, C. M., Salmon, P. L., Smit, T. H., and Klein-Nulend, J. (2008) Osteocyte morphology in fibula and calvaria- Is there a role for mechanosensing? *Bone* **43**, 452-458

83. Ravosa, M. J. (1988) Browridge development in cercopithecidae - A test of two models. *Am J Phys Anthropol* **76**, 535-555

84. Weidenreich, F. (1943) *The skull of* Sinanthropus pekinensis*; a comparative study on a primitive hominid skull*, Geological Survey of China, Pehpei, Chungking,

85. Biewener, A. A., Fazzalari, N. L., Konieczynski, D. D., and Baudinette, R. V. (1996) Adaptive changes in trabecular architecture in relation to functional strain patterns and disuse. *Bone* **19**, 1-8

86. Cowin, S. C. (2001) *Bone Mechanics Handbook*, 2nd ed., CRC Press, Boca Raton, FL

87. Pearson, O. M., and Lieberman, D. E. (2004) The aging of Wolff's "law": Ontogeny and responses to mechanical loading on cortical bone. *Am J Phys Anthropol*, 63-99

88. Ruff, C., Holt, B., and Trinkaus, E. (2006) Who's afraid of the big bad wolff? "Wolff's law" and bone functional adaptation. *Am J Phys Anthropol* **129**, 484-498

89. Lanyon, L. E. (1974) Experimental support for trajectorial theory of bone-structure. *Journal of Bone and Joint Surgery-British Volume* **B 56**, 160-166

90. Pontzer, H., Lieberman, D. E., Momin, E., Devlin, M. J., Polk, J. D., Hallgrimsson, B., and Cooper, D. M. (2006) Trabecular bone in the bird knee responds with high sensitivity to changes in load orientation. *J Exp Biol* **209**, 57-65

91. Chirchir, H., Kivell, T. L., Ruff, C. B., Hublin, J. J., Carlson, K. J., Zipfel, B., and Richmond, B. G. (2015) Recent origin of low trabecular bone density in modern humans. *Proceedings of the National Academy of Sciences of the United States of America* **112**, 366-371

92. Lanyon, L. E. (1973) Analysis of surface bone strain in the calcaneus of sheep during normal locomotion. Strain analysis of the calcaneus. *J Biomech* **6**, 41-49

93. Cotter, M. M., Simpson, S. W., Latimer, B. M., and Hernandez, C. J. (2009) Trabecular microarchitecture of hominoid thoracic vertebrae. *Anat Rec* **292**, 1098-1106

94. Ryan, T. M., and van Rietbergen, B. (2005) Mechanical significance of femoral head trabecular bone structure in Loris and Galago evaluated using micromechanical finite element models. *Am J Phys Anthropol* **126**, 82-96

95. Ryan, T. M., and Krovitz, G. E. (2006) Trabecular bone ontogeny in the human proximal femur. *J Hum Evol* **51**, 591-602

96. Ryan, T. M., and Ketcham, R. A. (2002) The three-dimensional structure of trabecular bone in the femoral head of strepsirrhine primates. *J Hum Evol* **43**, 1-26

97. Hildebrand, T., Laib, A., Muller, R., Dequeker, J., and Ruegsegger, P. (1999) Direct three-dimensional morphometric analysis of human cancellous bone: microstructural data from spine, femur, iliac crest, and calcaneus. *J Bone Miner Res* **14**, 1167-1174

98. Fajardo, R. J., and Muller, R. (2001) Three-dimensional analysis of nonhuman primate trabecular architecture using micro-computed tomography. *Am J Phys Anthropol* **115**, 327-336

99. Ryan, T., and Ketcham, R. (2002) Analysis of trabecular bone structure in the femoral heads of two Omomyid primates. *Am J Phys Anthropol*, 135-135

100. Maga, M., Kappelman, J., Ryan, T. M., and Ketcham, R. A. (2006) Preliminary observations on the calcaneal trabecular microarchitecture of extant large-bodied hominoids. *Am J Phys Anthropol* **129**, 410-417

101. Ryan, T. M., and Walker, A. (2010) Trabecular bone structure in the humeral and femoral heads of anthropoid primates. *Anat Rec* **293**, 719-729

102. Ryan, T. M., Walker, A., Swiatoniowski, A., and Van Rietbergen, B. (2010) Interlimb variation in trabecular bone architecture in primates. *Am J Phys Anthropol*, 204-204

103. Ryan, T. M., and Shaw, C. N. (2012) Unique suites of trabecular bone features characterize locomotor behavior in human and non-human anthropoid primates. *Plos One* **7**, e41037

104. van Ruijven, L. J., Giesen, E. B. W., Mulder, L., Farella, A., and van Eijden, T. M. G. J. (2005) The effect of bone loss on rod-like and plate-like trabeculae in the cancellous bone of the mandibular condyle. *Bone* **36**, 1078-1085

105. Ryan, T. M., Colbert, M., Ketcham, R. A., and Vinyard, C. J. (2010) Trabecular bone structure in the mandibular condyles of gouging and nongouging platyrrhine primates. *Am J Phys Anthropol* **141**, 583-593

106. Giesen, E. B., Ding, M., Dalstra, M., and van Eijden, T. M. (2001) Mechanical properties of cancellous bone in the human mandibular condyle are anisotropic. *J Biomech* **34**, 799-803

107. Giesen, E. B. W., Ding, M., Dalstra, M., and van Eijden, T. M. G. J. (2004) Changed morphology and mechanical properties of cancellous bone in the mandibular condyles of edentate people. *Journal of Dental Research* **83**, 255-259

108. Chalk, J., Richmond, B. G., Ross, C. F., Strait, D. S., Wright, B. W., Spencer, M. A., Wang, Q., and Dechow, P. C. (2011) A finite element analysis of masticatory stress hypotheses. *Am J Phys Anthropol* **145**, 1-10

109. Dzialo, C., Wood, S. A., Berthaume, M., Smith, A., Dumont, E. R., Benazzi, S., Weber, G. W., Strait, D. S., and Grosse, I. R. (2014) Functional implications of squamosal suture size in *Paranthropus boisei*. *Am J Phys Anthropol* **153**, 260-268

110. Wang, Q., Wood, S. A., Grosse, I. R., Ross, C. F., Zapata, U., Byron, C. D., Wright, B. W., and Strait, D. S. (2012) The role of the sutures in biomechanical dynamic simulation of a macaque cranial finite element model: implications for the evolution of craniofacial form. *Anat Rec* **295**, 278-288

111. Groning, F., Liu, J., Fagan, M. J., and O'Higgins, P. (2011) Why do humans have chins? Testing the mechanical significance of modern human symphyseal morphology with finite element analysis. *Am J Phys Anthropol* **144**, 593-606

112. Kupczik, K., Dobson, C. A., Fagan, M. J., Crompton, R. H., Oxnard, C. E., and O'Higgins, P. (2007) Assessing mechanical function of the zygomatic region in

macaques: validation and sensitivity testing of finite element models. *J Anat* **210**, 41-53

113. Ledogar, J., Smith , A., Benazzi, S., Weber , G., Spencer , M., Carlson, K., McNulty, K., Dechow, P., Grosse, I., Ross, C., Richmond, B., Wright, B., Wang , Q., Byron , C., Slice, D., Carlson, K., de Ruiter, D., Berger, L., Tamvada, K., Pryor Smith, L., Berthaume, M., and Strait, D. The feeding mechanics of *Australopithecus sediba*: an assessment of the MH1 cranium using finite element analysis. Science. Invited contribution to a special issue on *Australopithecus sediba*.

114. Ryan, T., and Shaw, C. (2013) Trabecular bone microstructure scales allometrically in the primate humerus and femur. *Proc R Soc B* **280**

115. Vinyard, C. J., and Taylor, A. B. (2010) A Preliminary analysis of the relationship between jaw-muscle architecture and jaw-muscle electromyography during chewing across primates. *Anat Rec* **293**, 572-582

116. Wright, B. W., Wright, K. A., Chalk, J., Verderane, M. P., Fragaszy, D., Visalberghi, E., Izar, P., Ottoni, E. B., Constantino, P., and Vinyard, C. (2009) Fallback foraging as a way of life: using dietary toughness to compare the fallback signal among capuchins and implications for interpreting morphological variation. *Am J Phys Anthropol* **140**, 687-699

117. Dzialo, C. M. (2014) Investigating the relationship between material property axes and strain orientations in *Cebus apella* crania.

118. Ridler, T. W., and Calvard, S. (1978) Picture thresholding using an iterative selection method. *Ieee Transactions on Systems Man and Cybernetics* **8**, 630-632

119. Ryan, T. M., and Ketcham, R. A. (2002) Femoral head trabecular bone structure in two omomyid primates. *J Hum Evol* **43**, 241-263

120. Trussell, H. J. (1979) Picture thresholding using an iterative selection method - Comments. *Ieee Transactions on Systems Man and Cybernetics* **9**, 311-311

121. Lorensen, W. E., and Cline, H. E. (1987) Marching cubes: A high resolution 3D surface construction algorithm. in *Proceedings of the 14th annual conference on Computer graphics and interactive techniques*, ACM

122. Dechow, P. C., Smith, L. C., Choate, C., and Curtis, B. (2012) Cortical bone density determined with microCT in the chimpanzee and gorilla facial skeletons. *Am J Phys Anthropol* **Supplement 54**, 127

123. Whitehouse, W. J. (1974) Quantitative Morphology of Anisotropic Trabecular Bone. *Journal of Microscopy-Oxford* **101**, 153-168

124. Harrigan, T. P., and Mann, R. W. (1984) Characterization of microstructural anisotropy in orthotropic materials. *Journal of Material Science* **19**, 761-767

125. Hildebrand, T., and Rüegsegger, P. (1997) A new method for the model-independent assessment of thickness in three-dimensional images. *Journal of Microscopy* **185**, 67-75

126. Odgaard, A., and Gundersen, H. J. G. (1993) Quantification of connectivity in cancellous bone, with special emphasis on 3-D reconstructions. *Bone* **14**, 173-182

127. Ketcham, R. A., and Ryan, T. M. (2004) Quantification and visualization of anisotropy in trabecular bone. *Journal of Microscopy* **213**, 158-171

128. Simmons, C. A., and Hipp, J. A. (1997) Method-based differences in the automated analysis of the three-dimensional morphology of trabecular bone. *J. Bone Miner Res* **12**, 942-947

129. Mittra, E., Rubin, C., and Qin, Y.-X. (2005) Interrelationship of trabecular mechanical and microstructural properties in sheep trabecular bone. *J Biomech* **38**, 1229-1237

130. Turner, C. H., Cowin, S. C., Rho, J. Y., Ashman, R. B., and Rice, J. C. (1990) The fabric dependence of the orthotropic elastic constants of cancellous bone. *J Biomech* **23**, 549-561

131. Kabel, J., Odgaard, A., van Rietbergen, B., and Huiskes, R. (1999) Connectivity and the elastic properties of cancellous bone. *Bone* **24**, 115-120

132. Kabel, J., van Rietbergen, B., Odgaard, A., and Huiskes, R. (1999) Constitutive relationships of fabric, density, and elastic properties in cancellous bone architecture. *Bone* **25**, 481-486

133. Ding, M., Odgaard, A., and Hvid, I. (2003) Changes in the three-dimensional microstructure of human tibial cancellous bone in early osteoarthritis. *Journal of Bone & Joint Surgery, British Volume* **85-B**, 906-912

134. Griffin, N. L., D'Août, K., Ryan, T. M., Richmond, B. G., Ketcham, R. A., and Postnov, A. (2010) Comparative forefoot trabecular bone architecture in extant hominids. *J Hum Evol* **59**, 202-213

135. Giesen, E. B. W., and van Eijden, T. M. G. J. (2000) The three-dimensional cancellous bone architecture of the human mandibular condyle. *Journal of Dental Research* **79**, 957-963

136. Carrier, D. R., and Morgan, M. H. (2014) Protective buttressing of the hominin face. *Biological reviews of the Cambridge Philosophical Society*

137. Bacabac, R. G., Mizuno, D., Schmidt, C. F., MacKintosh, F. C., Van Loon, J. J. W. A., Klein-Nulend, J., and Smit, T. H. (2008) Round versus flat: Bone cell morphology, elasticity, and mechanosensing. *J Biomech* **41**, 1590-1598

138. Tanck, E., Homminga, J., van Lenthe, G. H., and Huiskes, R. (2001) Increase in bone volume fraction precedes architectural adaptation in growing bone. *Bone* **28**, 650-654

139. van Ruijven, L. J., Giesen, E. B. W., and van Eijden, T. M. G. J. (2002) Mechanical significance of the trabecular microstructure of the human mandibular condyle. *Journal of Dental Research* **81**, 706-710

140. Aaron, J. E., Makins, N. B., and Sagreiya, K. (1987) The microanatomy of trabecular bone loss in normal aging men and women. *Clin Orthop Relat Res*, 260-271

141. Kneissel, M., Boyde, A., Hahn, M., Teschler-Nicola, M., Kalchhauser, G., and Plenk, H., Jr. (1994) Age- and sex-dependent cancellous bone changes in a 4000y BP population. *Bone* **15**, 539-545

142. Goldstein, S. A., Goulet, R., and McCubbrey, D. (1993) Measurement and significance of three-dimensional architecture to the mechanical integrity of

trabecular bone. *Calcified Tissue International* **53 Suppl 1**, S127-132; discussion S132-123

143. Lublinsky, S., Ozcivici, E., and Judex, S. (2007) An automated algorithm to detect the trabecular-cortical bone interface in micro-computed tomographic images. *Calcified Tissue International* **81**, 285-293

144. Rak, Y. (1983) *The Australopithecine Face*, Academic Press, New York

145. Lieberman, D. (2011) *The Evolution of the Human Head*, Belknap Press of Harvard University Press, Cambridge, Mass.

146. Klein-Nulend, J., van der Plas, A., Semeins, C. M., Ajubi, N. E., Frangos, J. A., Nijweide, P. J., and Burger, E. H. (1995) Sensitivity of osteocytes to biomechanical stress in vitro. *FASEB journal: official publication of the Federation of American Societies for Experimental Biology* **9**, 441-445

147. van Oers, R. F., Wang, H., and Bacabac, R. G. (2015) Osteocyte shape and mechanical loading. *Current Osteoporosis Reports* **13**, 61-66

148. van't Hof, R. J., and Ralston, S. H. (2001) Nitric oxide and bone. *Immunology* **103**, 255-261

149. Klein-Nulend, J., Semeins, C. M., Ajubi, N. E., Nijweide, P. J., and Burger, E. H. (1995) Pulsating fluid flow increases nitric oxide (NO) synthesis by osteocytes but not periosteal fibroblasts--correlation with prostaglandin upregulation. *Biochemical and Biophysical Research Communications* **217**, 640-648

150. Dechow, P. C., Wang, Q., and Peterson, J. (2010) Browridge morphology & hominid evolution: is there any evidence for a mechanical influence? *FASEB J.* **24**, 174.171-

151. Yinshi Ren, Y. L., Jerry Feng. (2014) A novel way for qualitative and quantitative analyses of morphologic changes osteocytes in health and disease. *Journal of Orthopaedic Translation* **2**, 197-198

152. Nakashige, M., Smith, A. L., and Strait, D. S. (2011) Biomechanics of the macaque postorbital septum investigated using finite element analysis: implications for anthropoid evolution. *J Anat* **218**, 142-150

153. Strait, D. S., Constantino, P., Lucas, P. W., Richmond, B. G., Spencer, M. A., Dechow, P. C., Ross, C. F., Grosse, I. R., Wright, B. W., Wood, B. A., Weber, G. W., Wang, Q., Byron, C., Slice, D. E., Chalk, J., Smith, A. L., Smith, L. C., Wood, S., Berthaume, M., Benazzi, S., Dzialo, C., Tamvada, K., and Ledogar, J. A. (2013) Viewpoints: Diet and dietary adaptations in early hominins: The hard food perspective. *Am J Phys Anthropol* **151**, 339-355

154. Strait, D. S., Wang, Q., Dechow, P. C., Ross, C. F., Richmond, B. G., Spencer, M. A., and Patel, B. A. (2005) Modeling elastic properties in finite element analysis: How much precision is needed to produce an accurate model? *Anat Rec Part A* **283A**, 275-287

155. Smith, A. L., Benazzi, S., Ledogar, J. A., Tamvada, K., Smith, L. C. P., Weber, G. W., Spencer, M. A., Lucas, P. W., Michael, S., Shekeban, A., Al-Fadhalah, K., Almusallam, A. S., Dechow, P. C., Grosse, I. R., Ross, C. F., Madden, R. H.,

Richmond, B. G., Wright, B. W., Wang, Q., Byron, C., Slice, D. E., Wood, S., Dzialo, C., Berthaume, M. A., Van Casteren, A., and Strait, D. S. (2015) The Feeding biomechanics and dietary ecology of *Paranthropus boisei*. *Anat Rec* **298**, 145-167

156. Klein-Nulend, J., Bacabac, R. G., and Bakker, A. D. (2012) Mechanical loading and how it affects bone cells: the role of the osteocyte cytoskeleton in maintaining our skeleton. *European Cells & Materials* **24**, 278-291

157. Smith, R. J., and Jungers, W. L. (1997) Body mass in comparative primatology. *J Hum Evol* **32**, 523-559

APPENDIX A

FIGURES

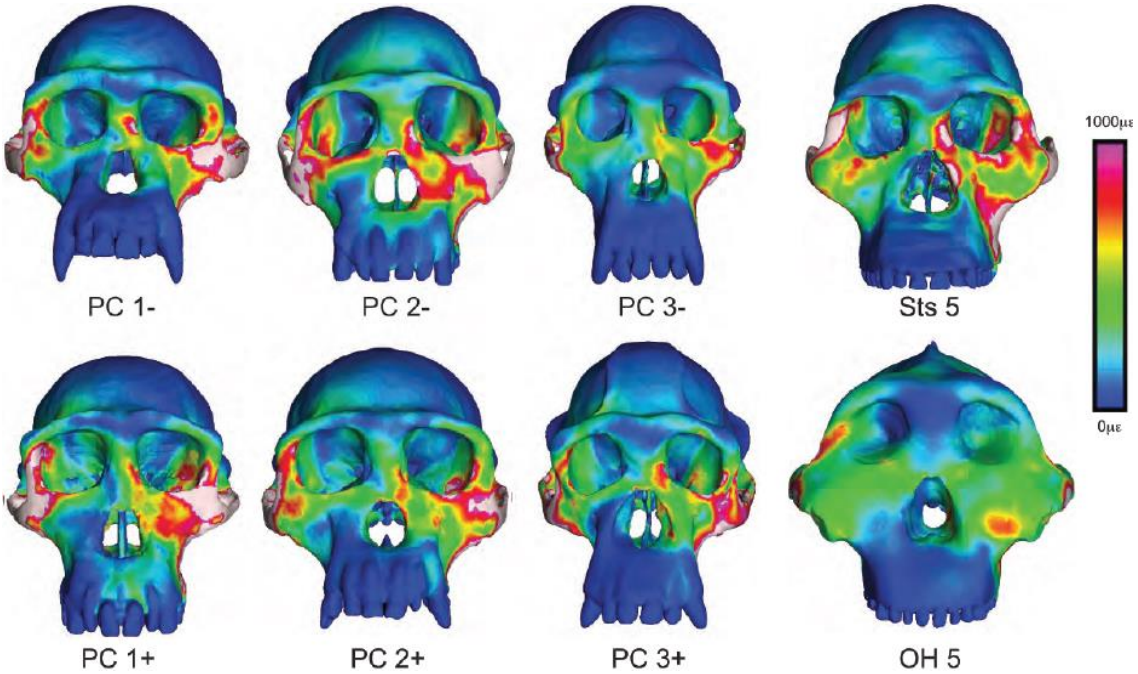

Figure 1-1 Interspecific strain in *Pan.* Intraspecific strain magnitudes in the browridge and zygoma across chimpanzee and interspecific variation in 2 additional hominid crania: *Australopithecus africanus* and *Paranthropus boisei*. Strain in the zygoma is much higher than in the browridge, a difference consistent across individuals and species (155).

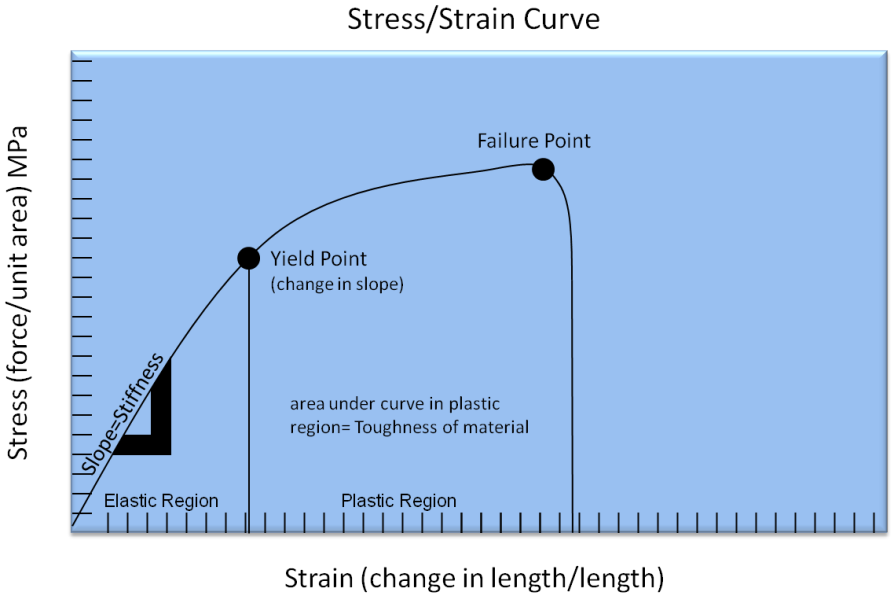

Figure 1-2 The relationship between stress and strain.

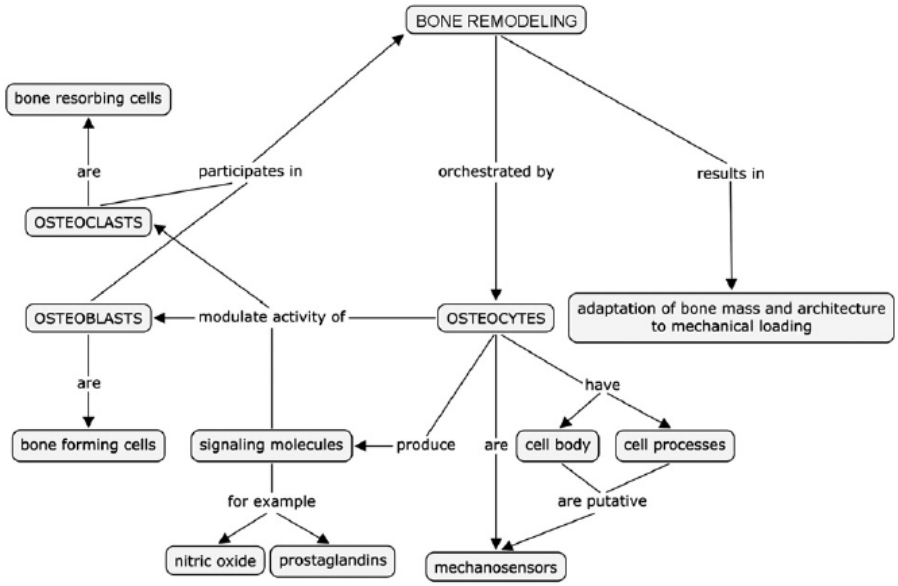

Figure 1-3 The central role of the osteocyte in bone remodeling. (156).

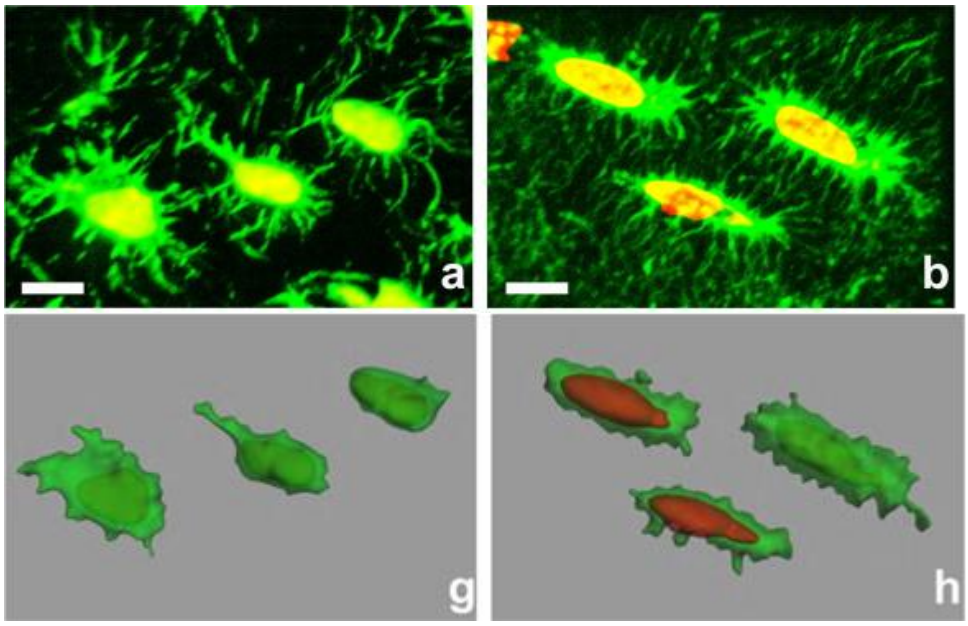

Figure 1-4 Three-dimensional analysis of osteocytes. Osteocytes stained with phalloidin and cyanic nucleic acid dye and visualized using confocal microscopy in '**a**' rat parietal bone and '**b'** rat tibial bone; surface renderings of cell bodies and nuclei of '**g'** rat calvarial bone and '**h'** rat tibial bone(80).

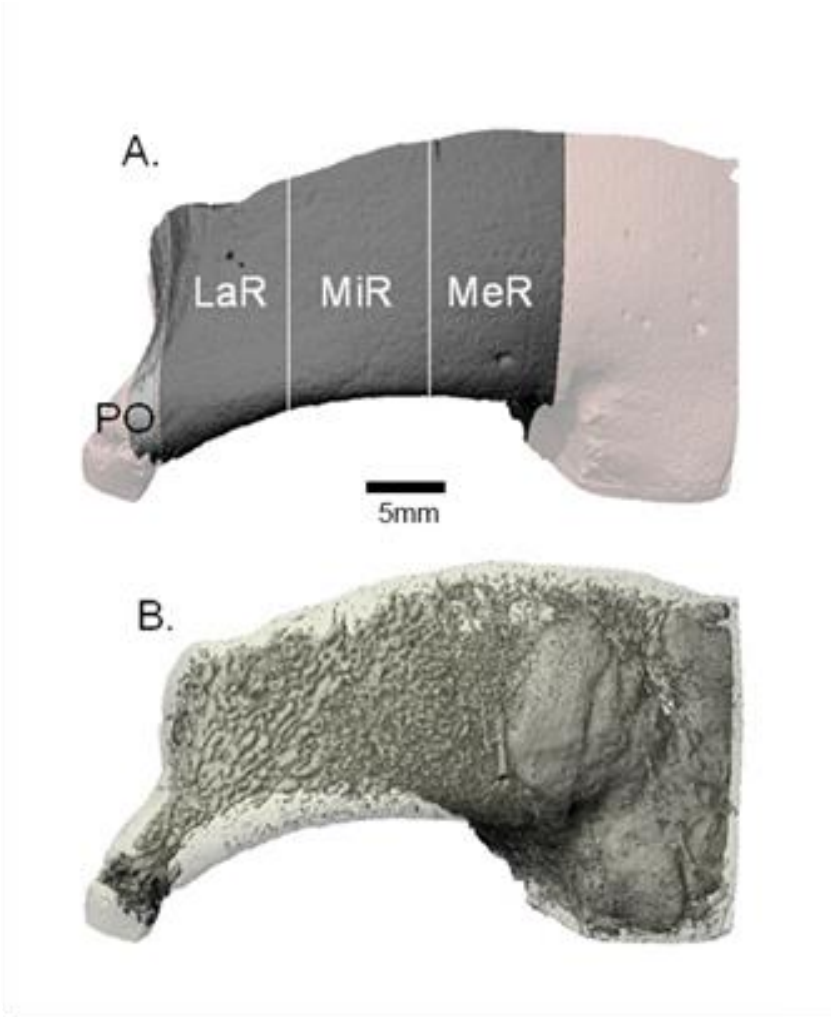

Figure 2-1 Subregions of supraorbital analysis. (A) Human supraorbital bone rendered from a µCT scan. Supraorbital bones were divided into a browridge region (dark grey) and a postorbital region (PO; shown in light grey). The browridge was subdivided into three regions approximately equal in length: a lateral ridge region (LaR), a middle ridge region (MiR), and a medial ridge region (MeR). (B) MicroCT rendering of the same supraorbital sample with bone depicted as transparent and sinus and pores depicted as solids.

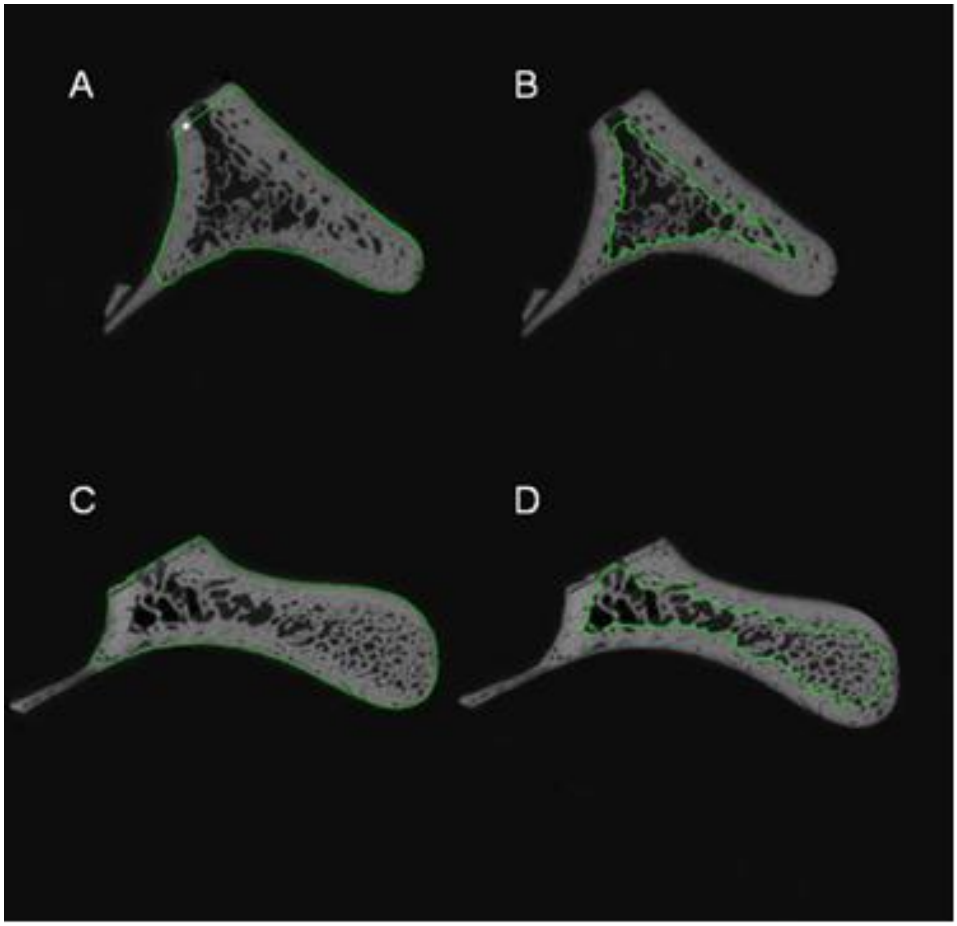

Figure 2-2 Trabecular region of interest in the human and *Pan* browridge. Region of interest contours on the (A) whole human browridge region and (B) the human trabecular region; and (C) whole *Pan* browridge and (D) *Pan* trabecular region.

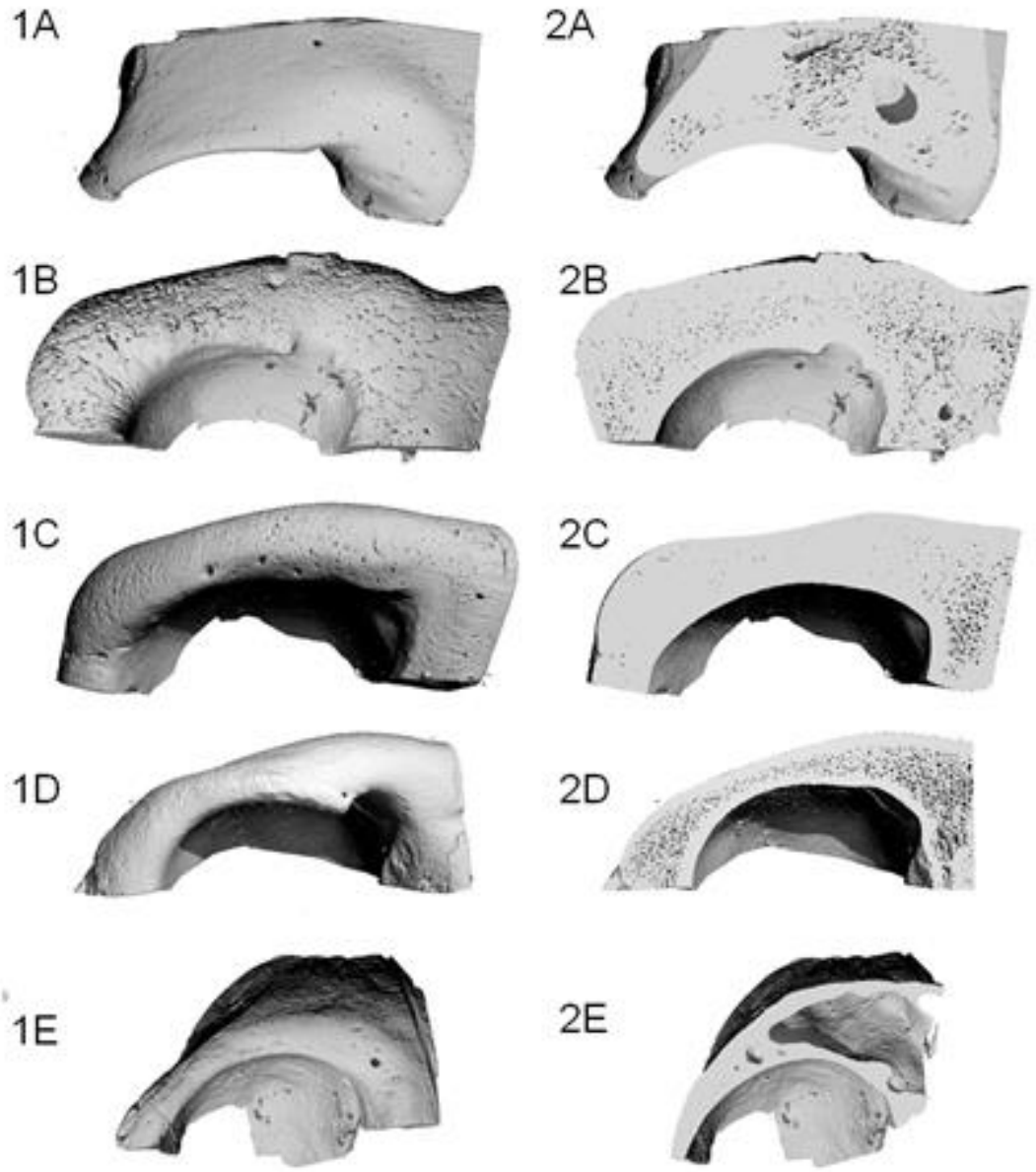

Figure 2-3 µCT renderings of whole extracted browridges. MicroCT rendering of whole extracted browridges from (A) human, (B) *Pan*, (C) *Gorilla*, (D) *Papio*, and (E) *Cebus* specimens. (1) Whole supraorbital bone; (2) whole supraorbital bone with coronal cut plane showing variations in internal bone structure.

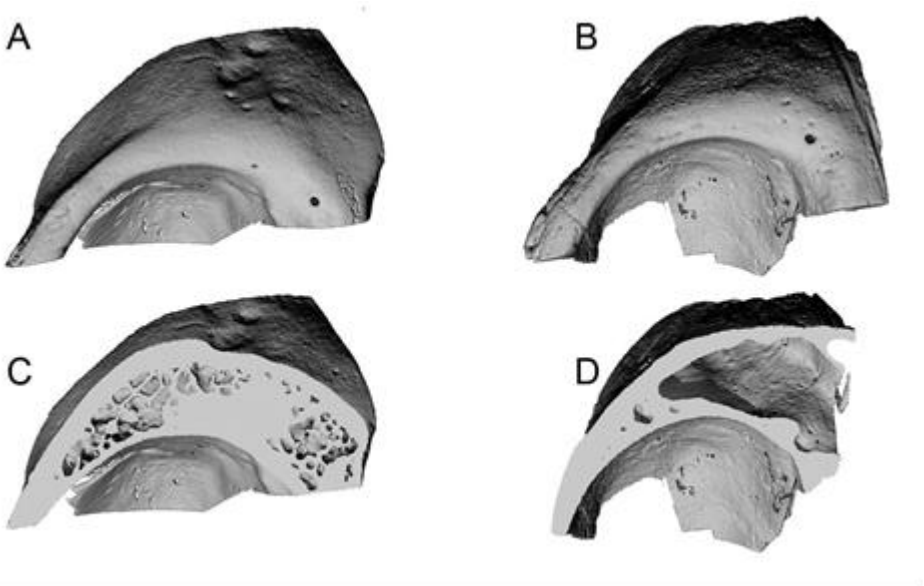

Figure 2-4 µCT renderings of *Cebus* browridges. Renderings showing variation in sinus size and amount of trabecular bone in this species.

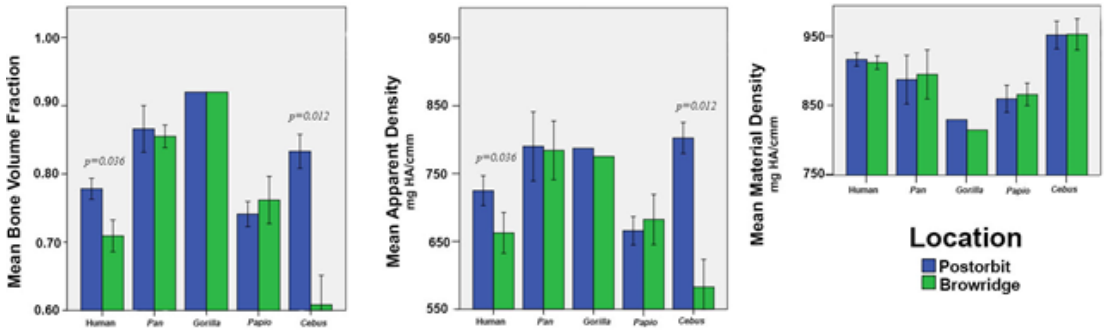

Figure 2-5 Mean BVF, mean apparent density, and mean material density. Bar graphs showing mean BVF, mean apparent density, and mean material density of whole supraorbital bone analysis across species and between postorbital and browridge regions. The only intraspecific differences were found in BVF and apparent density in humans and *Cebus*.

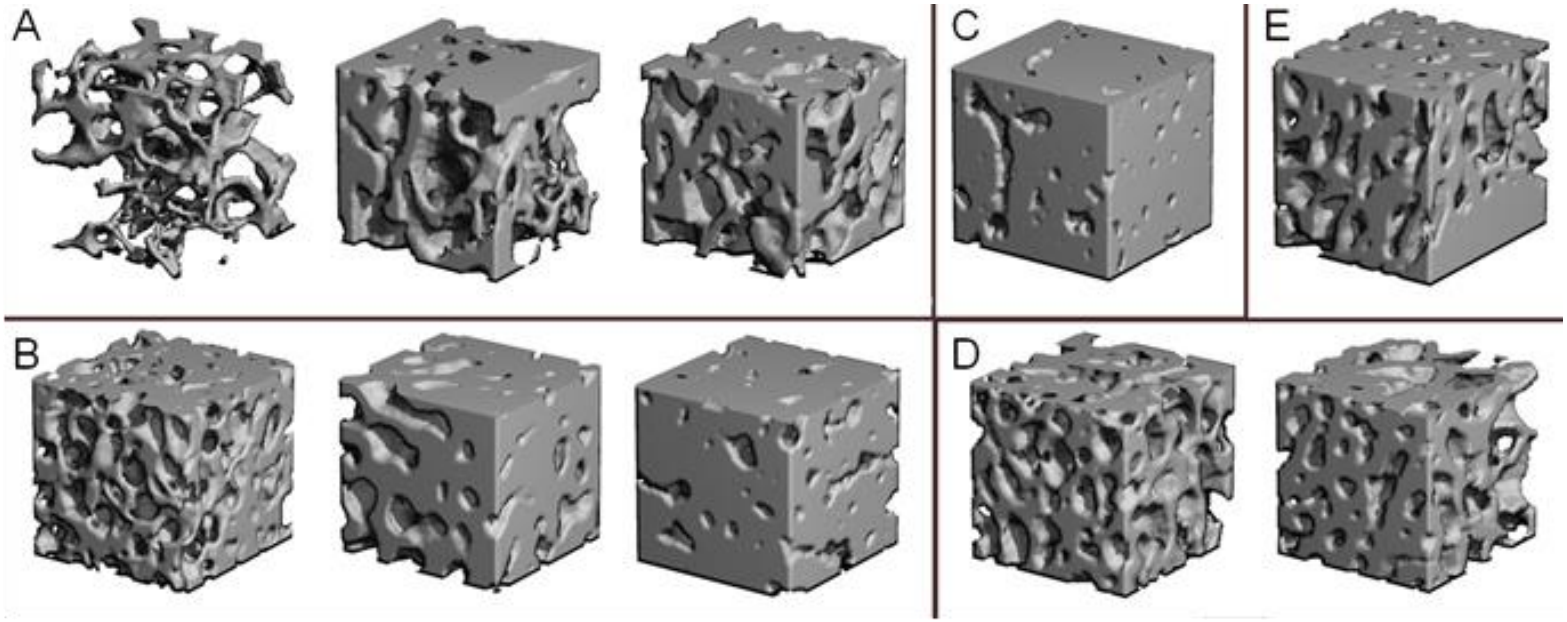

Figure 2-6 µCT renderings of browridge trabecular sub-volumes. Randomly selected regions of trabecular bone approximately 3.7 mm^3: (A) human, (B) *Pan*, (C) *Gorilla*, (D) *Papio*, and (E) *Cebus*. These illustrate the variation in trabecular structure between species and individuals

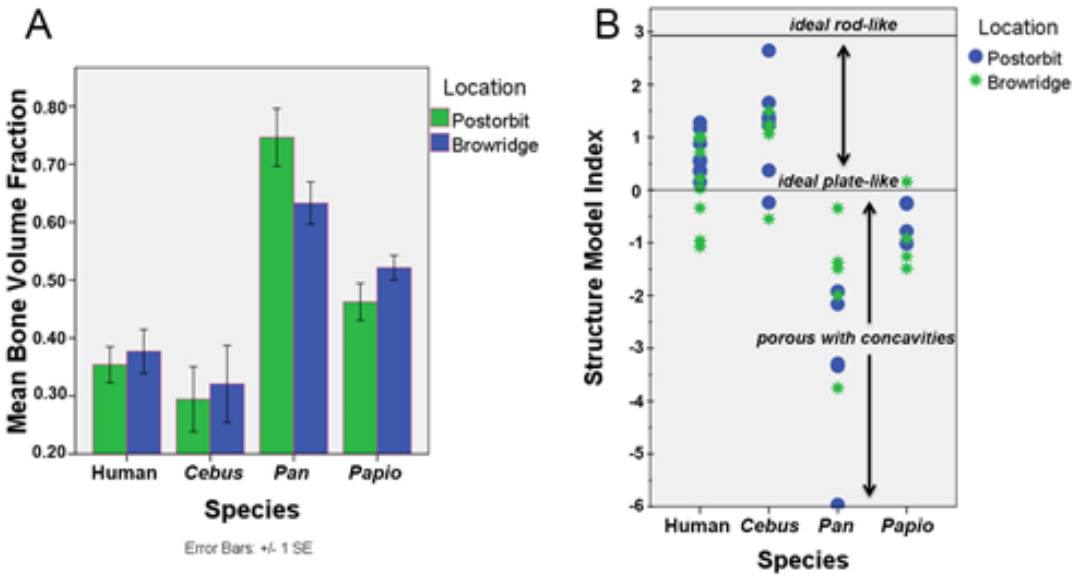

Figure 2-7 Mean BVF and structure model index. (A) Mean BVF of trabecular bone postorbital and browridges across species. (B) Structure model index of individuals in each sample from postorbit and browridge regions. Values close to 3 represent more rod-like trabecular bone, values nears 0 represent more plate-like trabecular bone and values below 0 represent porous bone with concave spaces.

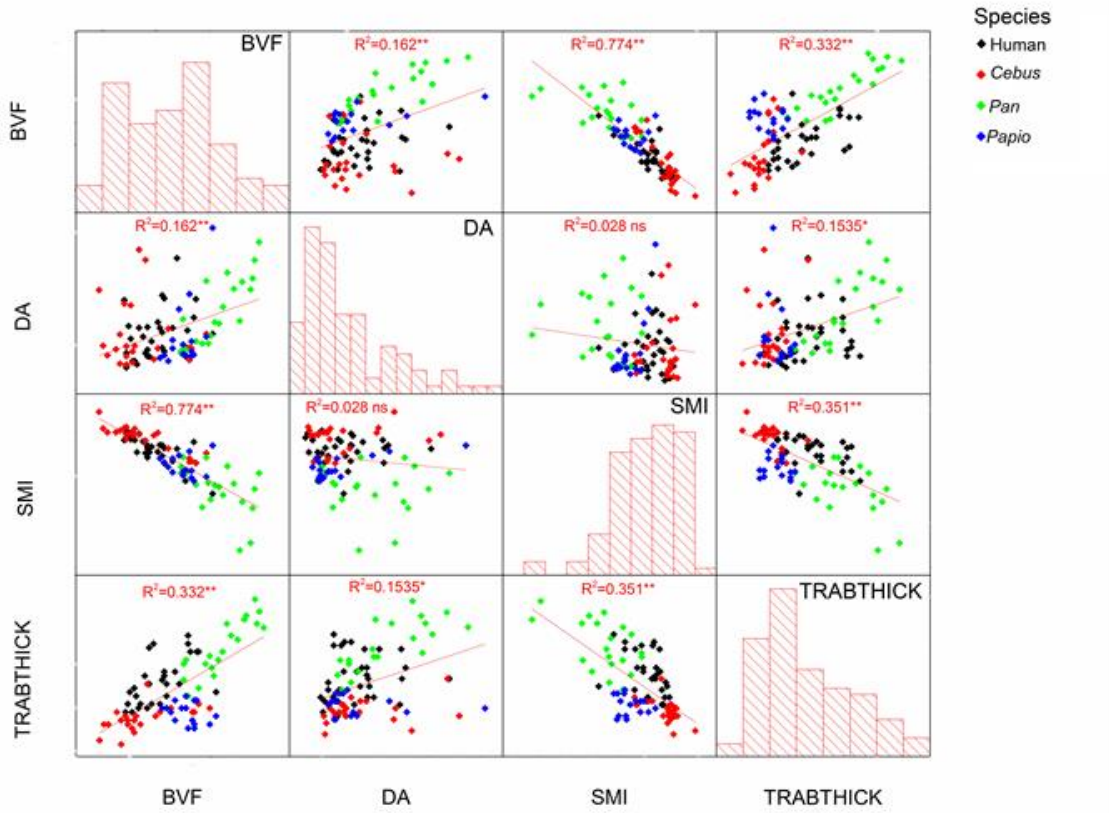

Figure 2-8 Correlation matrix of browridge morphometry. Correlation matrix with Spearman R^2 Values (*p≤0.01; **p≤0.001) and histogram of individual variables.

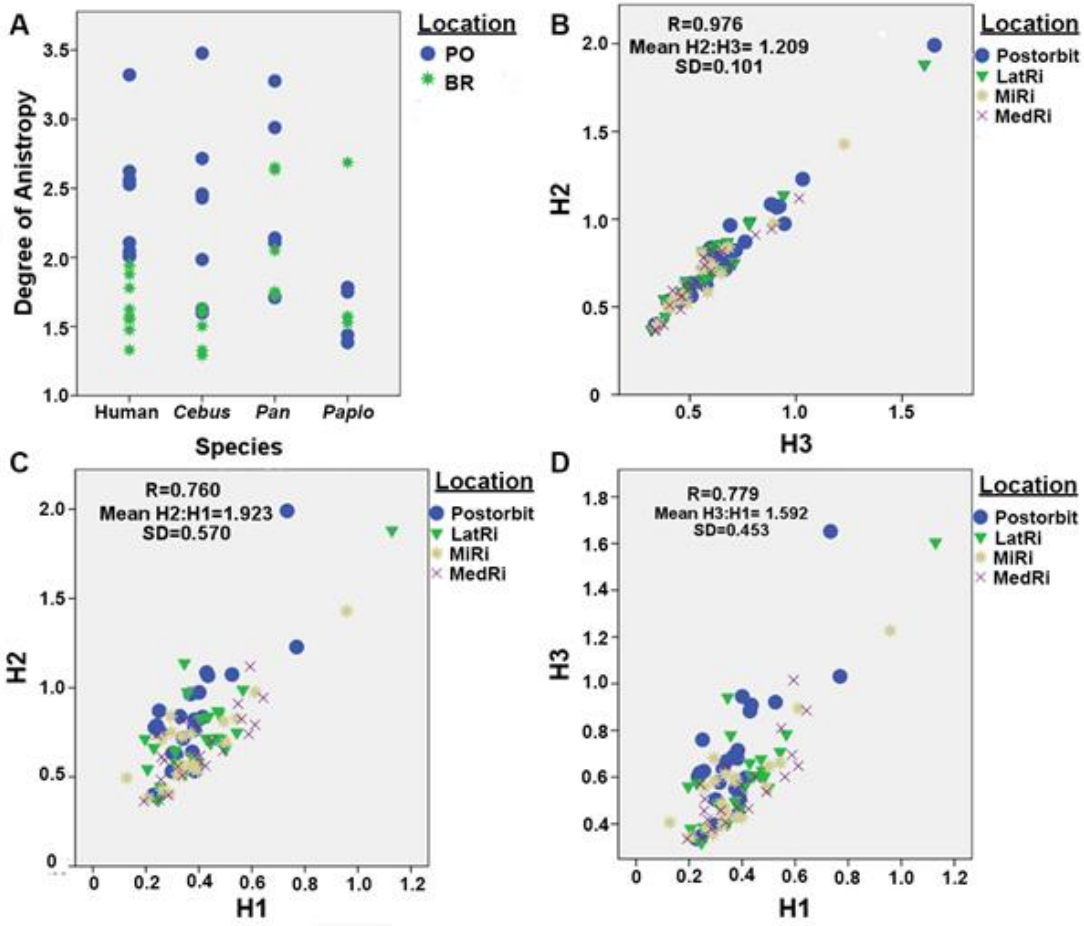

Figure 2-9 Supraorbital degree of anisotropy. (A) Degree of anisotropy across individuals in the browridge and postorbital regions. (B) Ratio of the primary vector of trabecular orientation (H2) to the secondary vector of trabecular orientation. (C) Ratio of primary vector of trabecular orientation (H2) to the tertiary vector of orientation. (D) Ratio of secondary (H3) to tertiary (H1) vectors of trabecular orientation. Close correlation and ratio of H2:H3 suggests that trabecular bone in the supraorbital region is transversely isotropic.

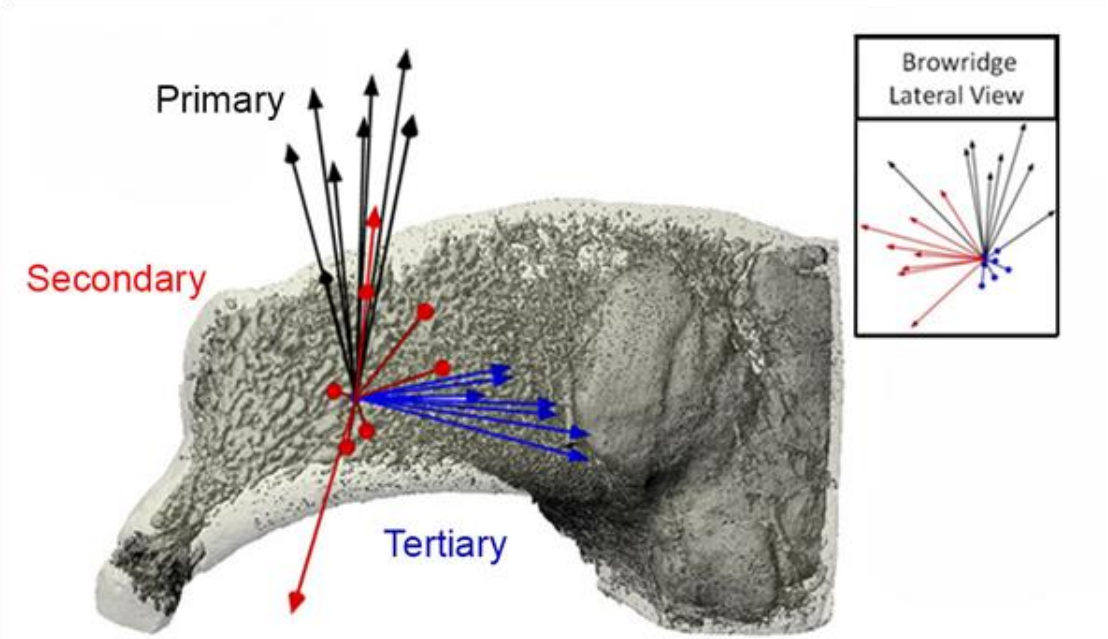

Figure 2-10 Trabecular orientation in the browridge. Frontal view of human primary, secondary, and tertiary vectors of trabecular orientation superimposed on a human browridge. Lateral view of vectors shows variation in the primary and secondary vectors lying in a sagittal plane, and consistency of tertiary vector in the medio-lateral direction.

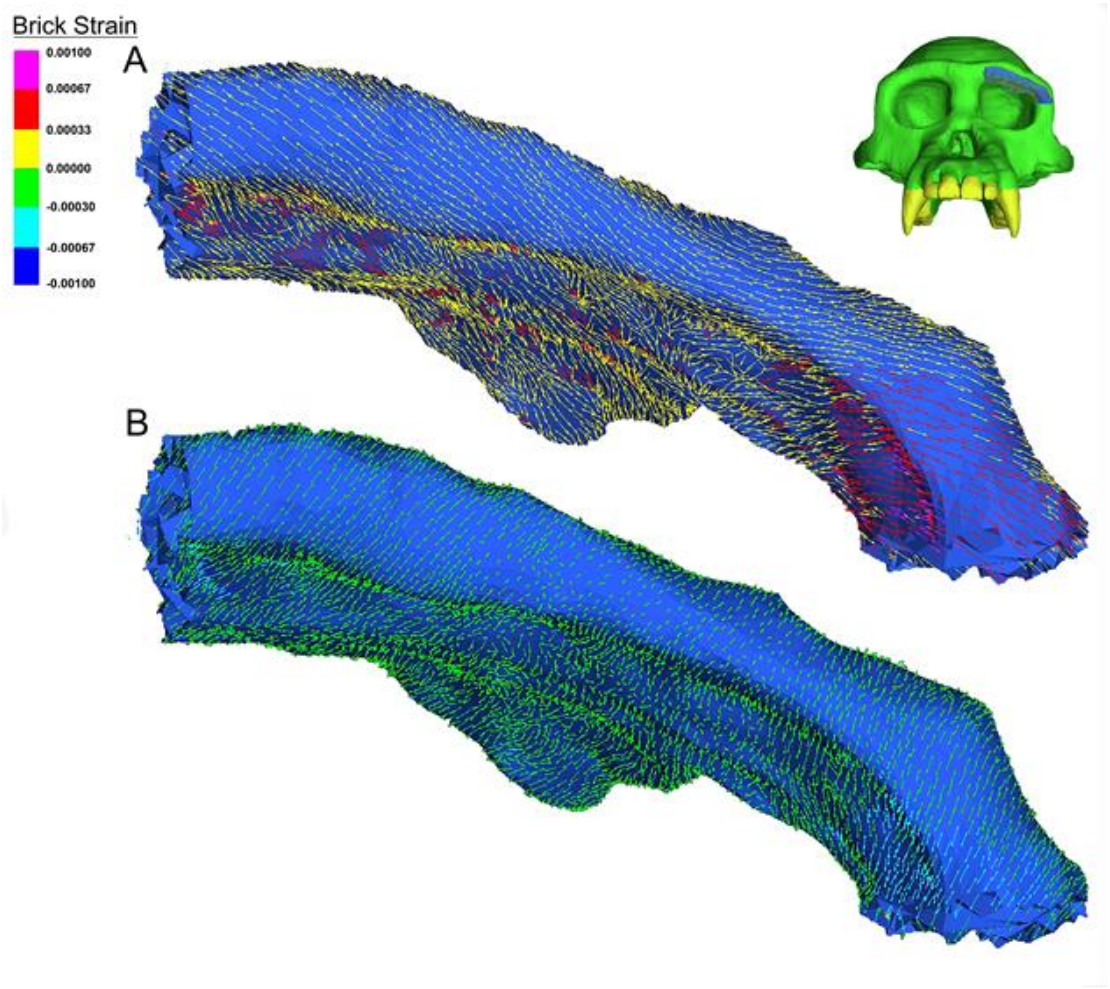

Figure 2-11 Primary and secondary supraorbital strain tensors. (A) Anterior view of left supraorbital trabecular region from the biting side showing primary strain (tension). Strain magnitude in the postorbital region is higher than along the browridge region. (B) Superior view of the left supraorbital trabecular region showing variability in primary strain orientations across the horizontal plane of the trabecular region.

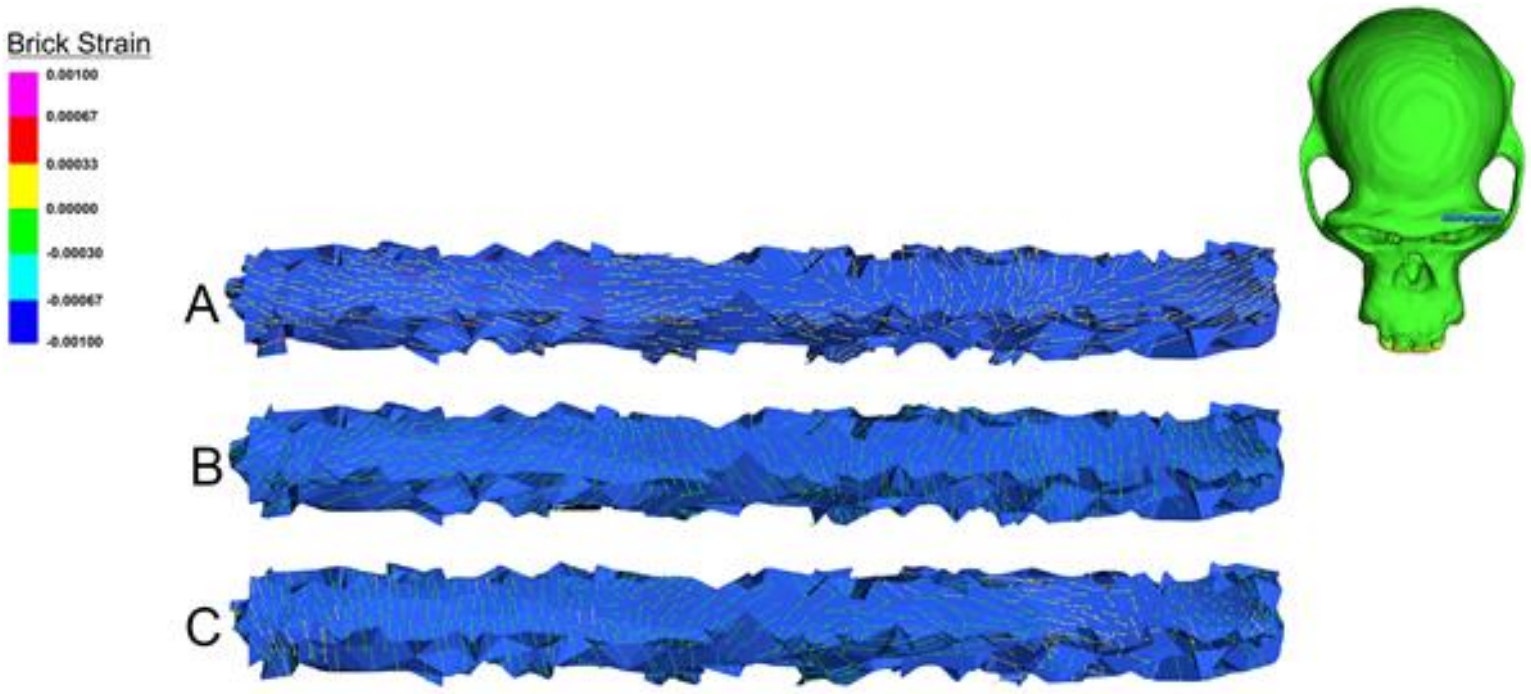

Figure 2-12 Superior view of supraorbital strain vectors. Superior view of an anterior subsection of browridge from the bite side showing (A) primary (tension), (B) tertiary (Compression) and (C) secondary (compression) strain vectors.

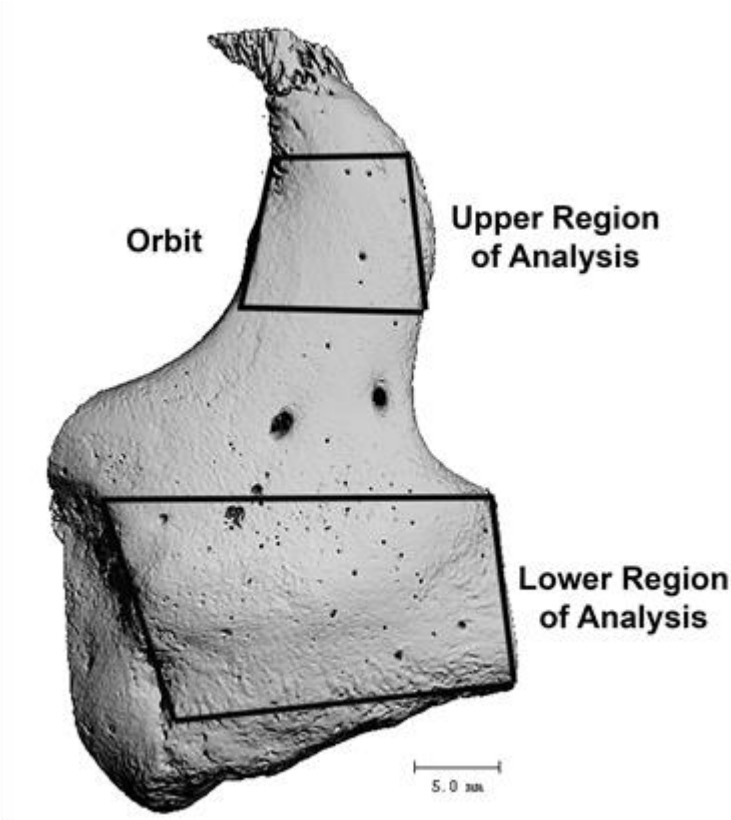

Figure 3-1 µCT rendering of human zygomatic regions of analysis.

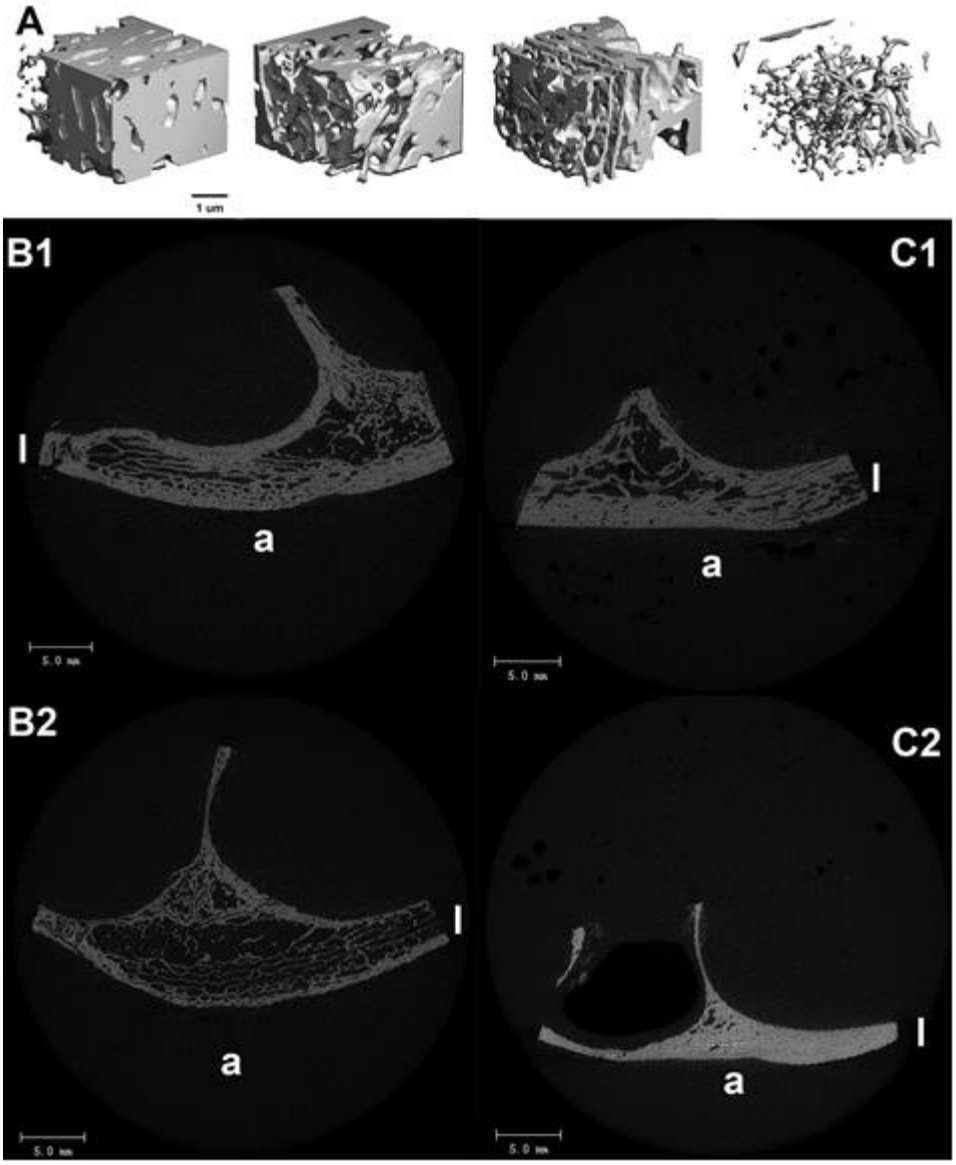

Figure 3-2 Rectangular sub-regions of zygomatic trabecular bone; transverse sections of µCT scans. (A) Rectangular regions measuring approximately 25 mm2 and 10 mm thick of trabecular bone rendered from human lower zygomatic body regions, showing variability in trabecular structure throughout this region. (B) Transverse section of a µCT scan of a human zygomatic body (1, 2) showing plate-like trabecular structure in the lateral end transitioning to more sparse rod-like trabecular bone in the medial region. (C) Transverse section of µCT scan of two *Pan* specimens, with (C1) trabecular bone and without (C2); For (B) and (C) "l" indicates lateral and "a" indicates anterior.

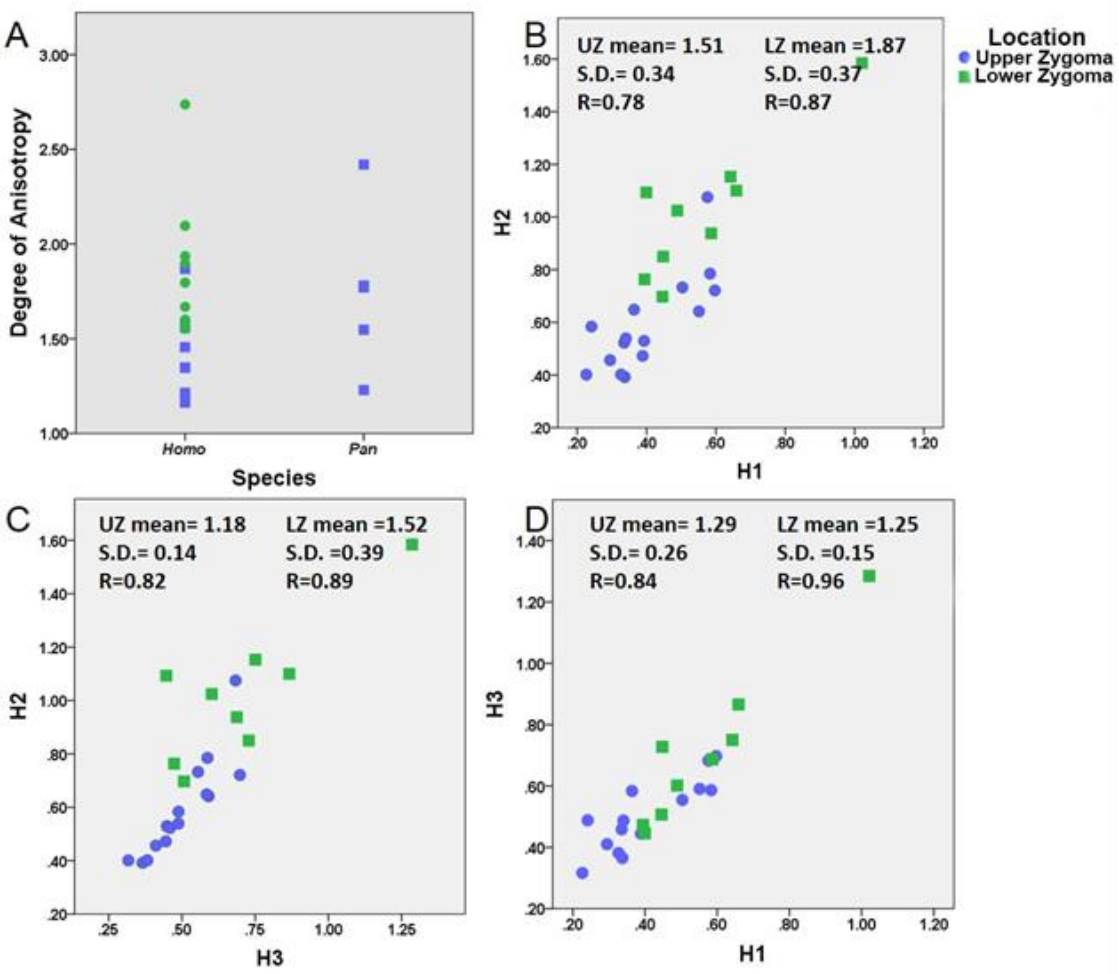

Figure 3-3 Degree of anisotropy in the zygoma. (A) DA across individuals in human and *Pan* upper (UZ) and lower (LZ) regions. (B) Ratio of the primary vector of trabecular orientation (H2) to the tertiary (H1) vector of trabecular orientation. (C) Ratio of primary vector of trabecular orientation (H2) to the secondary (H3) vector of orientation. (D) Ratio of secondary (H3) to tertiary (H1) vectors of trabecular orientation.

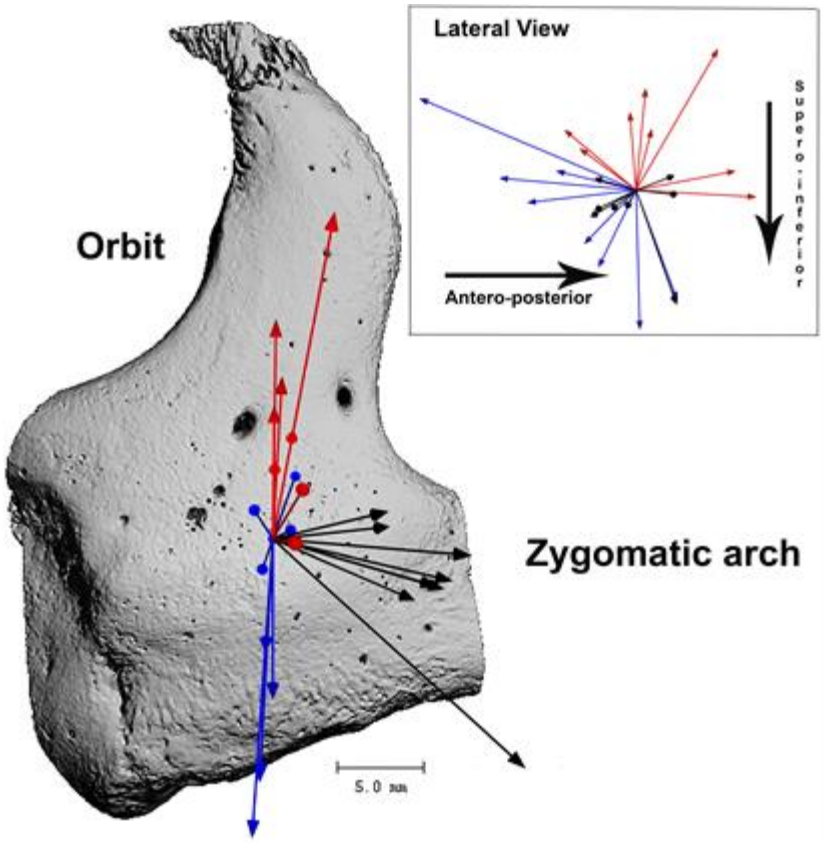

Figure 3-4 Trabecular orientation in the human zygoma. Anterior view primary (black), secondary (red), and tertiary (blue) vectors of trabecular orientation in the human lower zygoma (zygomatic body) superimposed on a µCT rendering of the human zygoma. The lateral perspective shows that secondary and tertiary eigenvectors vary in a sagittal plane, and demonstrate the consistency of primary vector in the medio-lateral direction.

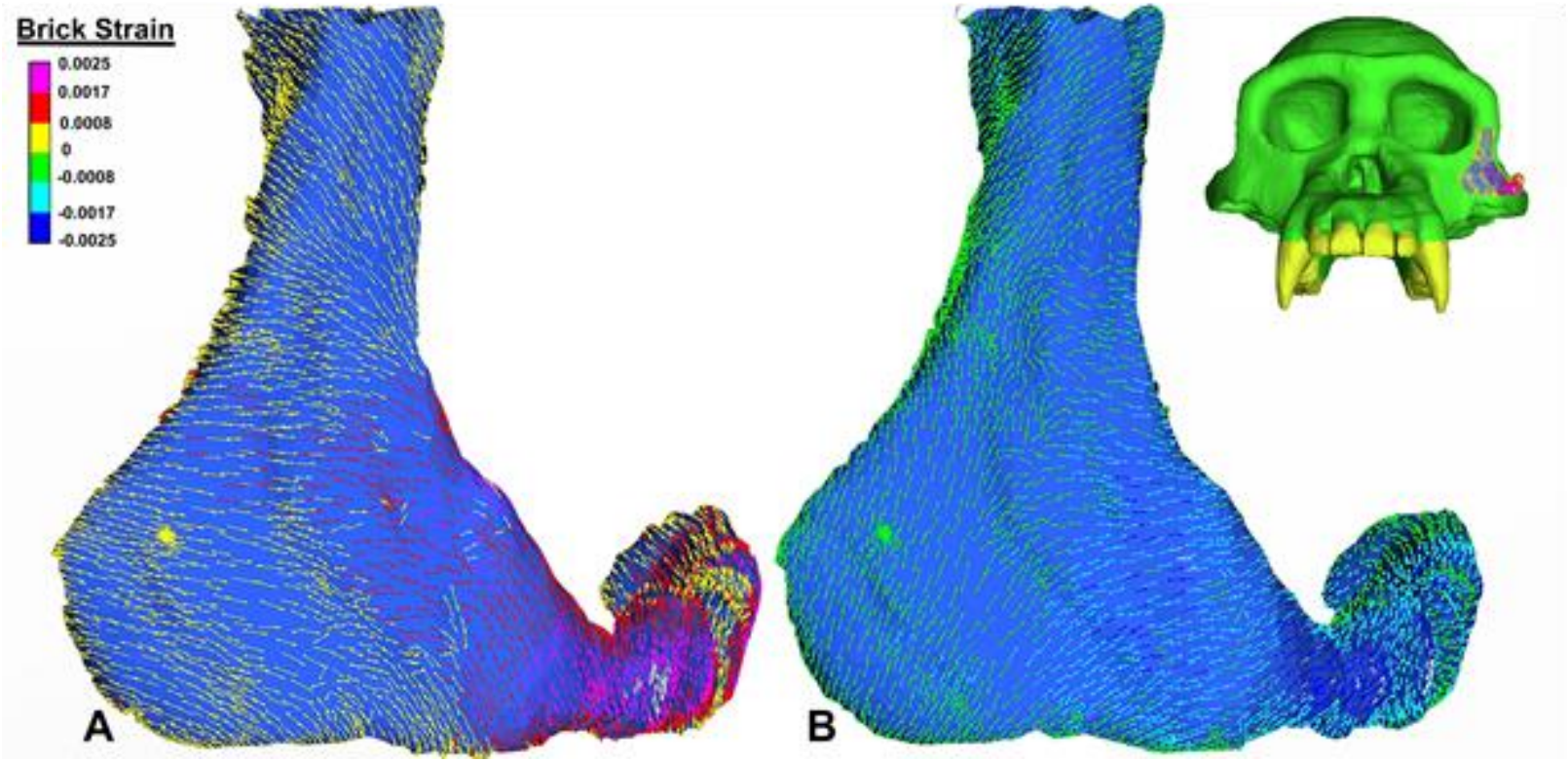

Figure 3-5 Strain tensors in the zygoma. (A) Anterior view of left zygomatic trabecular region from the biting side of a *Pan* finite element model, demonstrating showing primary strain (tension) in the upper and lower zygomatic regions. Strain magnitude in the upper zygomatic or postorbital region is lower than in the lower/ zygomatic body region. (B) Anterior view of the left zygomatic trabecular region showing secondary strain (compression) in upper and lower zygomatic regions.

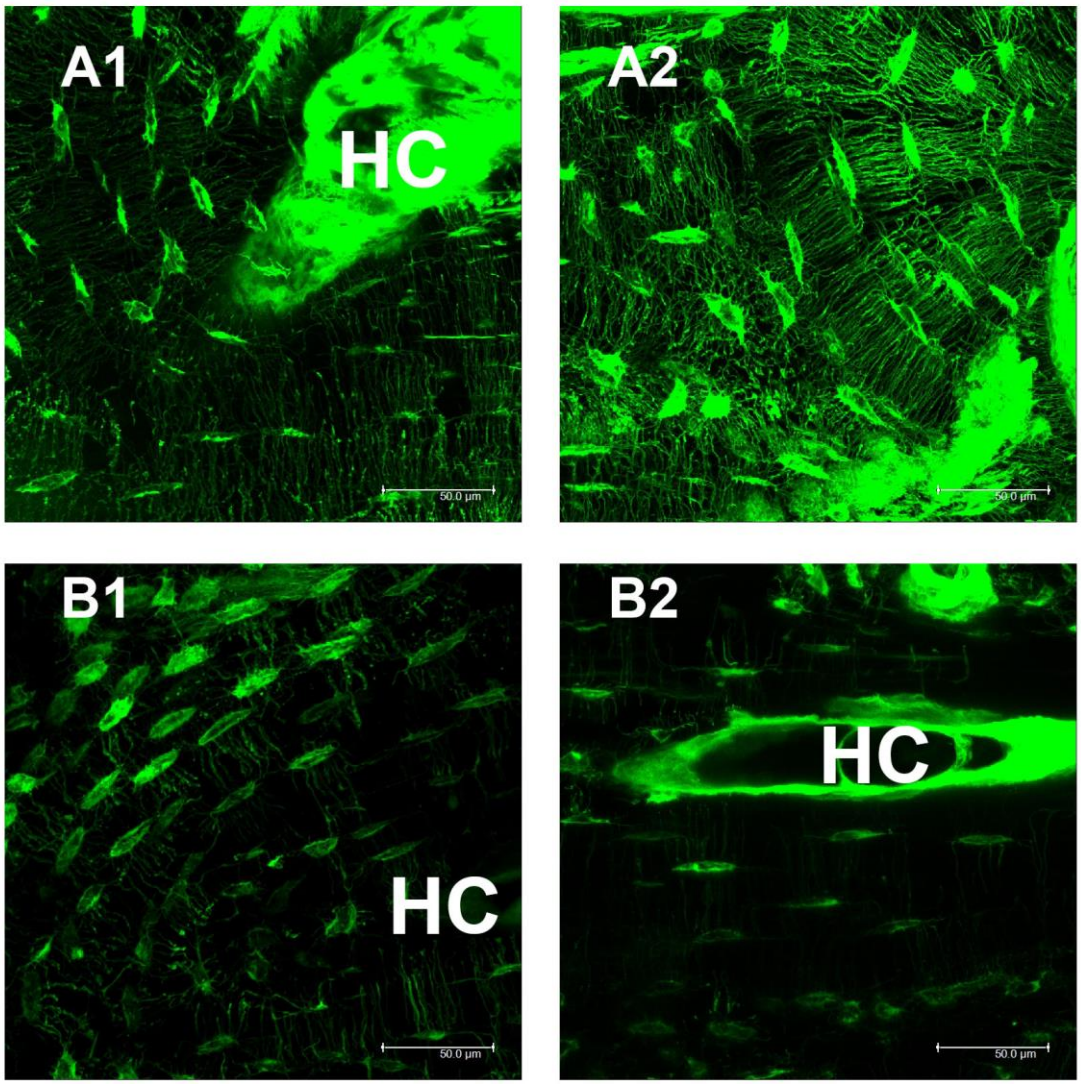

Figure 4-1 Confocal images of human osteocytes. Osteocytes in human individuals **(**A and B) in the supraorbital (1) and zygomatic (2) regions demonstrating the individual variability in bone quality across our sample. Individual A appears to have a greater concentration of osteocytes and osteocytic connections. Haversian Canals are represented by "HC".

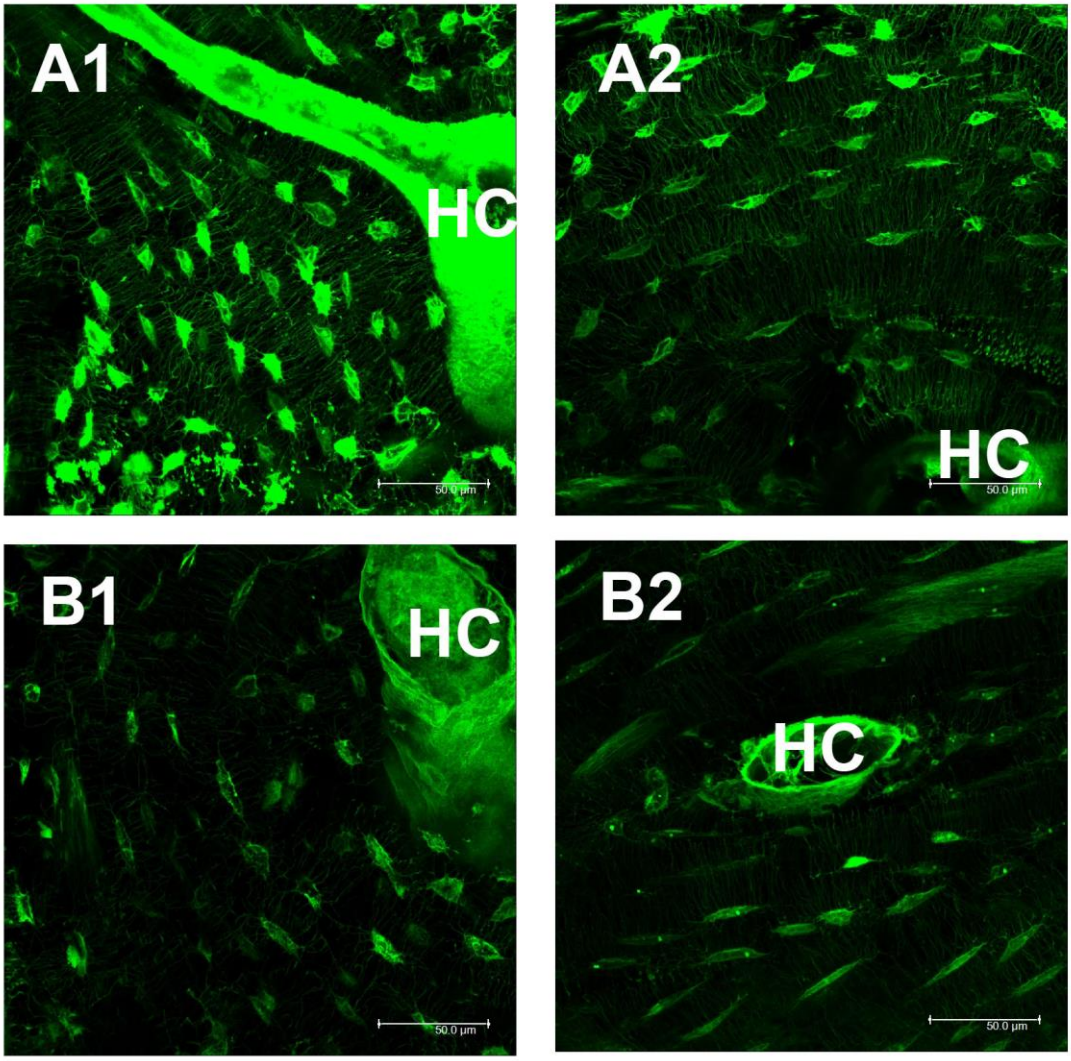

Figure 4-2 Confocal images of *Pan* osteocytes. Stacked confocal images of the *Pan* individuals (A and B) in the supraorbital (1) and zygomatic (2) regions displaying dense, well connected osteocytic networks. Haversian Canals are represented by "HC".

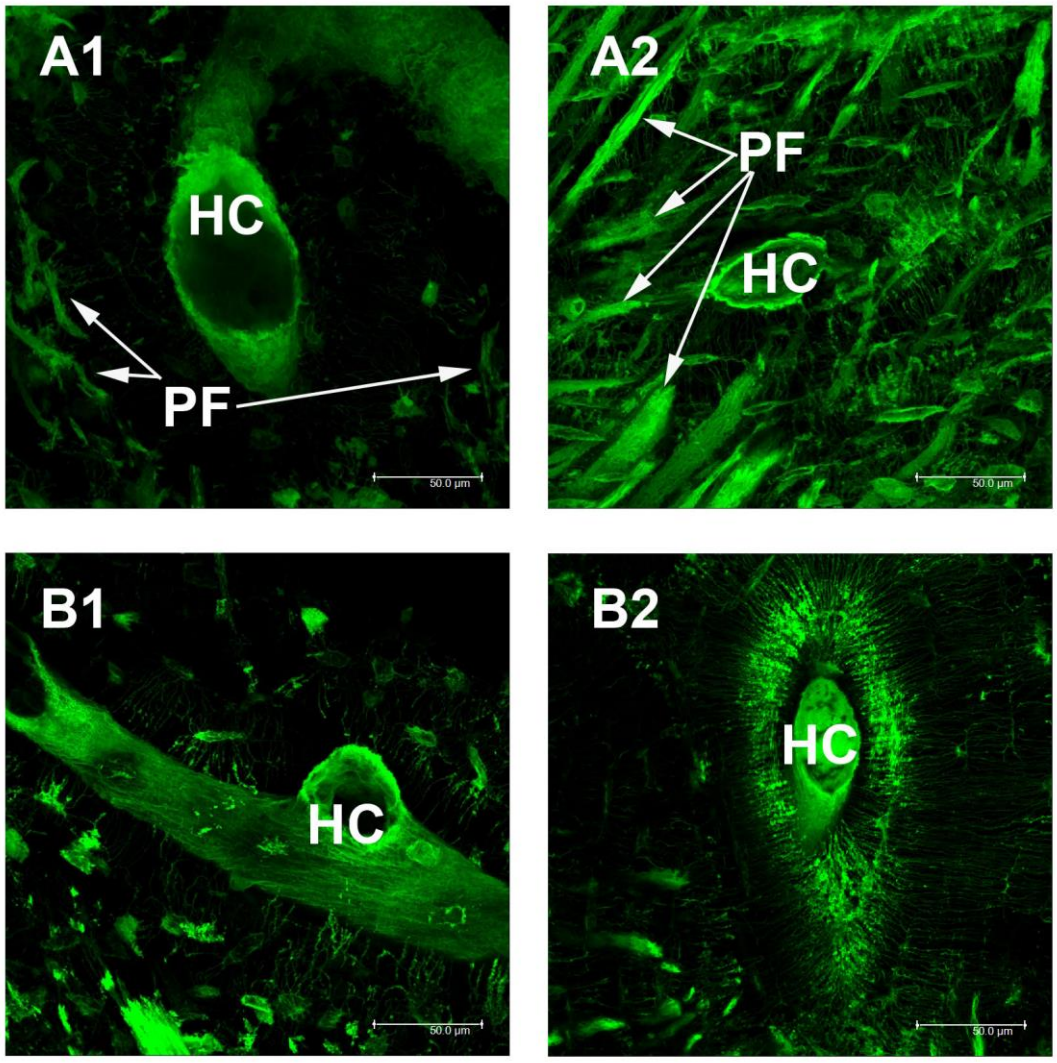

Figure 4-3 Confocal images of *Pan* osteocytes demonstrating periosteal fibers. Osteocytes in supraorbital (1) and zygomatic (2) regions demonstrating the individual variability in bone quality and microanatomy across our sample. Like in humans, some samples contained more sporadically oriented and seemingly less connected osteocytes (A and B) than others, which displayed dense, well connected osteocytic networks. Variations in periosteal fiber (PF) concentrations were also observed (A). Haversian Canals are represented by "HC".

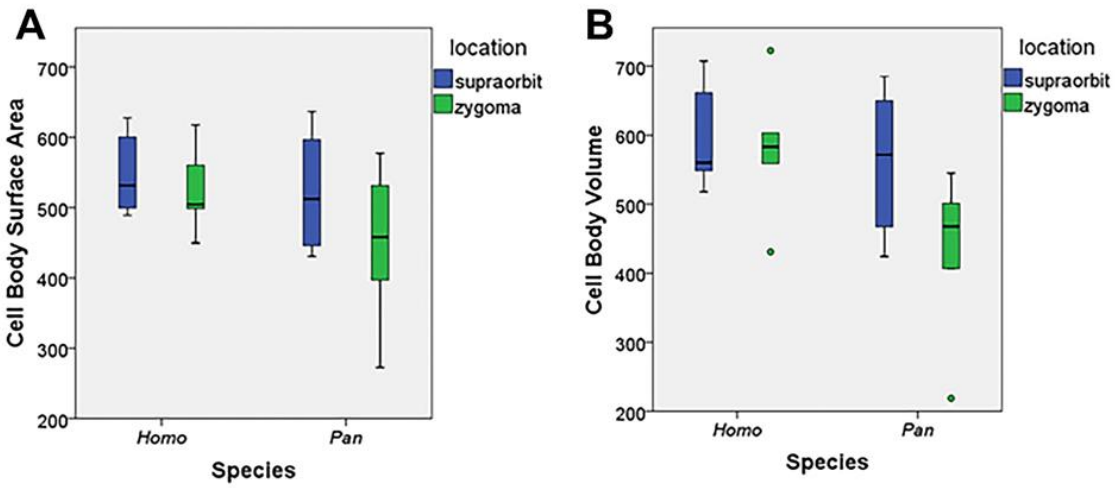

Figure 4-4 Osteocyte cell body surface area and volume. Cell body surface area (A) and volume (B) represented as an average of each individual by region, demonstrates a large variation across individuals.

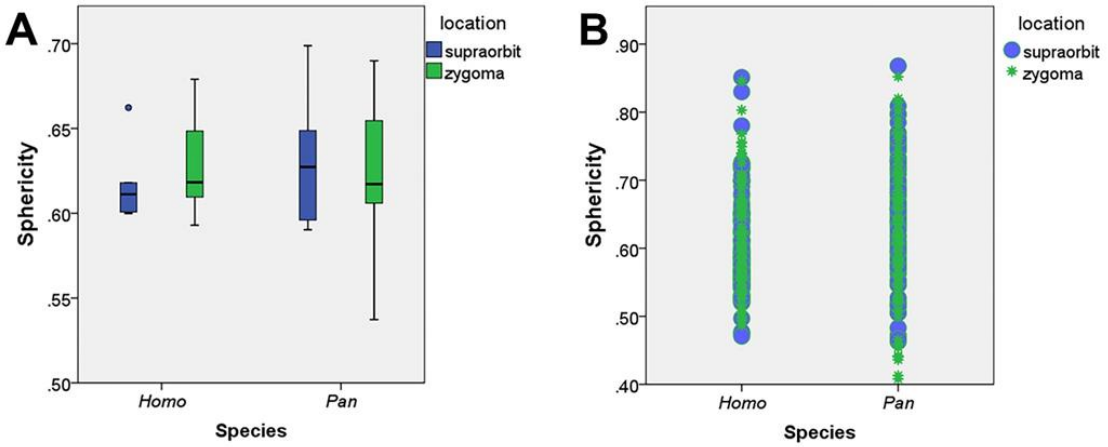

Figure 4-5 Osteocyte degree of sphericity. Sphericity represented as an average of each individual by region shows a large variation in average sphericity by individual in all regions except the human supraorbit. Actual sphericity values for each cell in both species and region show the large spread of individual cell measures across the sample, especially in *Pan*.

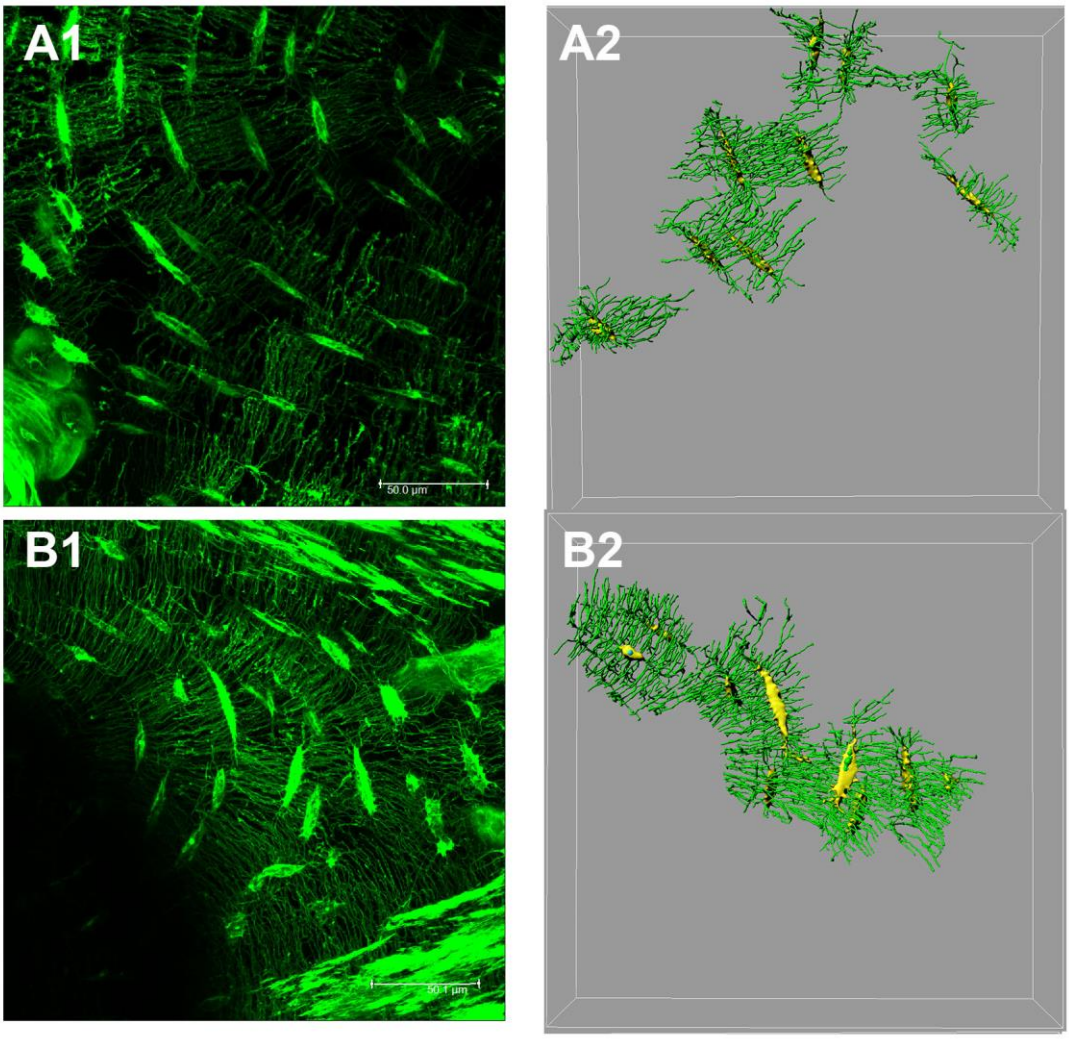

Figure 4-6 Human confocal images alongside cell body and dendrite renderings. Confocal stacks of human supraorbit (A1) and zygoma (B1) and the corresponding cell body and dendrite renderings (2) for 8-9 osteocytes. Confocal Images and Imaris renderings demonstrate the heterogeneity in cell body shape between regions.

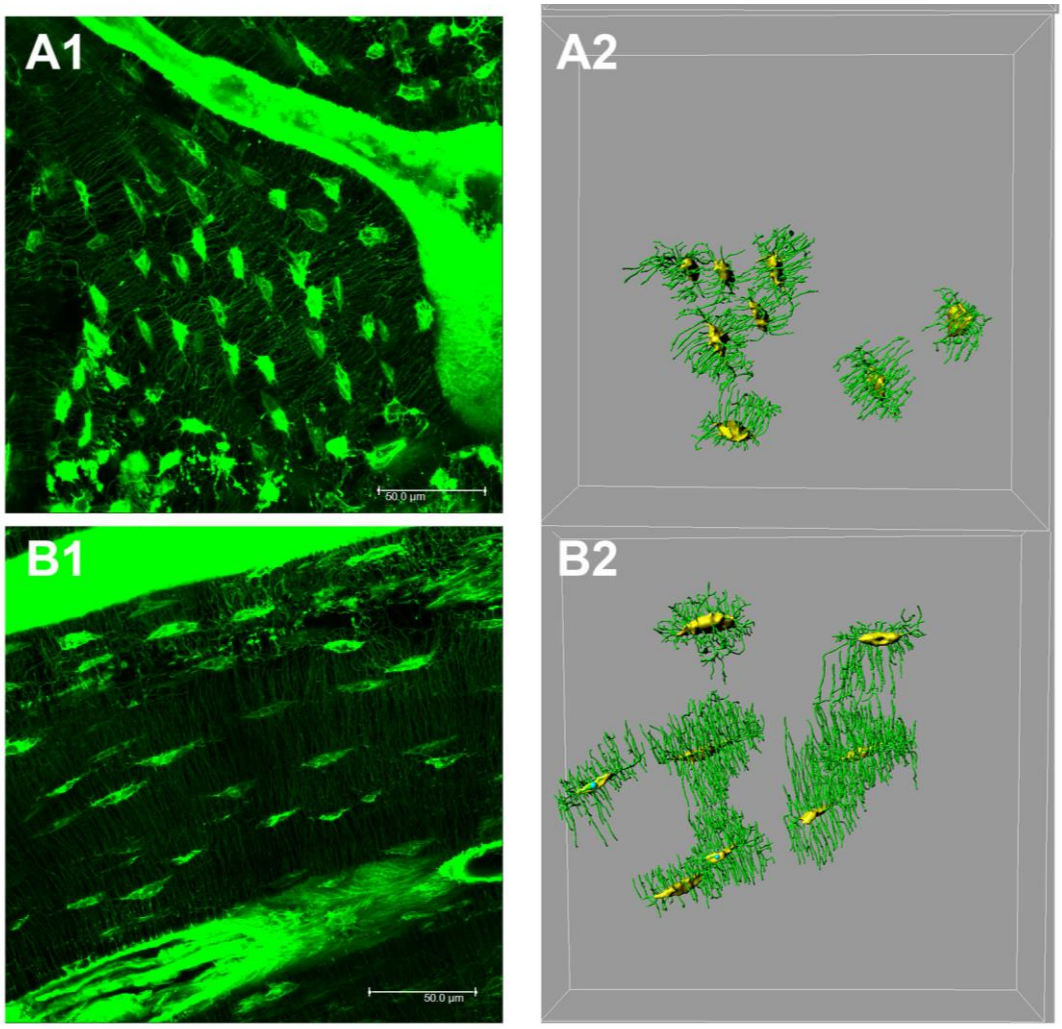

Figure 4-7 *Pan* confocal images alongside cell body and dendrite renderings. Confocal stacks of *Pan* supraorbit (A1) and zygoma (B1) and the corresponding cell body and dendrite renderings (2) for 8-9 osteocytes. Confocal Images and Imaris renderings demonstrate a more oblate cell body shape in the supraorbital region.

APPENDIX B

TABLES

Table 2.1 Species, body mass, and trabecular VOI in the browridge. Species and number of sample for both male and female; estimated body weights and standard deviations of species taken from Smith and Jungers (157); mean total volumes and SDs of mm^3 of trabecular/subcortical bone analyzed by microCT for both whole browridge and postorbital regions male and female. Unavailable (ua)

Species	N			Estimated Body Weight (kg)		Trabecular Browridge VOI volume (mm^3)		Trabecular Post Orbit VOI volume (mm^3)	
	m	fm		m	fm	m	fm	m	fm
Homo sapiens	6	2	Mean	72.1	62.1	1468	765	105	69
			SD	11.4	9.88	559	430	52	2.3
Pan troglodytes	1	3	Mean	60	47.4	1580	921	678	279
			SD	ua	ua	225	36	480	75
Pan paniscus		1	Mean	45.0	33.2	-	265	-	91
			SD	8.4	4.2	-	-	-	-
Gorilla gorilla		1	Mean	169.5	71.5	-	0	-	0
			SD	25.8	ua	-	-	-	-
Papio anubis	2	2	Mean	21.2	11.7	1456	370	251	129
			SD	2.1	1.3	160	197	14	8.4
Cebus albifrons	5	2	Mean	3.26	2.13	163	45	32	5.4
			SD	0.429	0.282	48	0.41	44	2.6

Table 2.2 Bone volume fraction, apparent and material density of whole supraorbital bone regions. Bone volume fraction (rounded to the nearest one hundredth), apparent and material density (rounded to the nearest mg) for whole bone (cortical + trabecular bone) browridge and postorbital regions.

Species	Location	BV/TV		Apparent Density (mg HA/cm^3)		Material Density (mg HA/cm^3)	
		Mean	S.D.	Mean	S.D.	Mean	S.D.
Homo	Post Orbit	0.78	0.04	724	62	916	27
	Browridge	0.71	0.07	663	85	912	28
Pan	Post Orbit	0.87	0.08	790	114	887	79
	Browridge	0.86	0.04	784	97	895	79
Gorilla	Post Orbit	0.92	-	787	-	829	-
	Browridge	0.92	-	775	-	814	-
Papio	Post Orbit	0.74	0.04	666	42	860	39
	Browridge	0.76	0.07	682	74	866	32
Cebus	Post Orbit	0.83	0.08	803	65	952	57
	Browridge	0.61	0.12	583	115	953	64

Table 2.3 Interspecific differences in density. Significance of interspecific differences determined by Mann-Whitney U test, $p \leq 0.05$

Species	Location	BV/TV	APPD	MATD
Homo vs Pan	**PO**			
	BR	0.003		
Homo vs Gorilla	**PO**			
	Br			
Homo vs Papio	**PO**			0.017
	Br			0.042
Homo vs Cebus	**PO**	0.046	0.027	
	Br			
Pan vs Gorilla	**PO**			
	Br			
Pan vs Papio	***PO***	0.027		
	Br			
Pan vs cebus	**PO**			
	BR	0.003	0.013	
Gorilla vs Papio	**PO**			
	BR			
Gorilla vs Cebus	**PO**			
	Br			
Papio vs Cebus	**PO**	0.0142	0.011	0.017
	Br	0.042		

Table 2.4 Trabecular bone morphometry of postorbit and browridge regions. Mean and SD of trabecular bone descriptors rounded to the nearest one hundredth determined by microCT trabecular bone analysis showing PO and whole BR regions.

Species	Location	BVF		DA		Tb.N (mm^3)		Tb.Th (mm^3)		Tb.Sep (mm^3)		SMI		ConnD (mm^3)	
		Mean	S.D.	Mean	S.D.	Mean	S.D.	Mean	S.D.	Mean	*S.D.*	Mean	S.D.	Mean	S.D.
Homo	**PO**	0.35	0.09	2.40	0.46	1.68	0.33	0.30	0.65	0.78	0.18	0.66	0.41	4.36	1.30
	BR	0.38	0.12	1.64	0.21	1.34	0.28	0.26	0.04	0.66	0.17	0.07	0.82	5.15	2.68
Pan	**PO**	0.75	0.11	2.43	0.65	2.43	0.24	0.40	0.06	0.34	0.09	-3.3	1.61	7.19	2.87
	BR	0.63	0.08	2.16	0.45	2.12	0.27	0.36	0.07	0.45	0.09	-1.79	1.25	5.96	2.73
Papio	**PO**	0.46	0.06	1.59	0.21	2.55	0.73	0.20	0.02	0.36	0.10	-0.58	0.39	15.06	10.09
	BR	0.52	0.04	1.84	0.57	2.64	0.76	0.22	0.03	0.35	0.10	-0.88	0.73	15.39	10.86
Cebus	**PO**	0.30	0.15	2.33	1.20	2.13	0.53	0.19	0.03	0.53	0.16	1.20	0.92	7.44	8.33
	BR	0.32	0.15	1.47	0.16	1.62	0.66	0.20	0.01	0.70	0.22	0.88	0.82	17.06	8.45

Table 2.5 Trabecular bone morphometry of postorbit and browridge subregions. Mean and SD of trabecular bone descriptors rounded to nearest one hundredth determined by microCT trabecular bone analysis showing PO and BR subregions.

Species	Location	BVF		DA		Tb.N (mm^3)		Tb.Th (mm^3)		Tb.Sep (mm^3)		SMI		ConnD (mm^3)	
		Mean	S.D	Mean	S.D.	Mean	S.D.	Mean	S.D.	Mean	S.D.	Mean	S.D.	Mean	S.D.
Homo	**PO**	0.35	0.09	2.40	0.46	1.68	0.33	0.30	0.65	0.78	0.18	0.66	0.41	4.36	1.30
	La	0.35	0.07	1.73	0.21	1.33	0.23	0.29	0.06	0.77	0.18	0.35	0.56	4.76	2.11
	Mi	0.39	0.11	1.17	0.38	1.47	0.26	0.29	0.07	0.69	0.14	0.17	0.85	5.44	2.58
	Me	0.42	0.16	1.61	0.36	1.56	0.63	0.30	0.08	0.71	0.29	-0.27	1.34	6.60	5.52
Pan	**PO**	0.75	0.11	2.43	0.65	2.43	0.24	0.40	0.06	0.34	0.09	-3.3	1.61	7.19	2.87
	La	0.73	0.12	2.64	0.70	2.49	0.31	0.38	0.07	0.33	0.10	-2.34	2.02	6.28	2.69
	Mi	0.64	0.13	2.22	0.58	2.25	0.31	0.35	0.08	0.41	0.10	-1.57	1.02	6.62	3.20
	Me	0.59	0.11	2.06	0.66	2.04	0.40	0.35	0.07	0.47	0.17	-1.41	0.78	5.70	2.45
Papio	**PO**	0.46	0.06	1.59	0.21	2.55	0.73	0.20	0.02	0.36	0.10	-0.58	0.39	15.06	10.09
	La	0.51	0.06	1.78	0.57	2.73	0.73	0.21	0.03	0.33	0.10	-0.74	0.77	16.12	10.94
	Mi	0.58	0.07	2.25	1.10	3.11	0.97	0.22	0.03	0.30	0.10	-0.85	0.94	17.48	10.69
	Me	0.50	0.04	1.74	0.42	2.54	0.80	0.21	0.03	0.37	0.11	-0.99	0.64	14.12	10.89
Cebus	**PO**	0.30	0.15	2.33	1.20	2.13	0.53	0.19	0.03	0.53	0.16	1.20	0.92	7.44	8.33
	La	0.29	0.14	1.82	0.67	1.52	0.59	0.21	0.04	0.77	0.22	1.11	0.79	12.32	7.69
	Mi	0.35	0.15	1.50	0.12	1.95	0.63	0.19	0.02	0.58	0.19	0.92	0.76	20.42	10.37
	Me	0.36	0.20	1.63	0.26	2.38	0.77	0.19	0.03	0.49	0.17	0.71	0.87	18.38	13.92

Table 2.6 Interspecific differences of supraorbital trabecular bone morphology.
Interspecific significance of trabecular bone descriptors determined by Mann-Whitney U tests, where $p \leq 0.05$

Species	Location	BV/TV	DA	SMI	ConnD (mm^3)	Tb.N (mm^3)	Tb.Thick (mm^3)	Tb.Sep (mm^3)
Homo vs Pan	**PO**	0.002	ns	0.002	ns	0.002	0.002	0.002
	BR	0.002	0.045	0.006	ns	0.002	ns	0.003
Homo vs Papio	**PO**	ns	0.004	0.004	0.004	0.016	0.016	0.006
	Br	0.016	ns	ns	0.028	0.004	0.028	0.004
Homo vs Cebus	**PO**	ns	ns	ns	ns	ns	0.001	ns
	Br	ns	ns	0.045	0.045	ns	0.019	ns
Pan vs Papio	**PO**	0.016	ns	0.016	ns	ns	0.016	ns
	Br	0.016	ns	ns	ns	ns	0.016	ns
Pan vs Cebus	**PO**	0.003	ns	0.003	ns	ns	0.003	0.030
	Br	0.008	0.008	0.016	ns	ns	0.008	ns
Papio vs Cebus	***PO***	ns	ns	0.006	0.042	ns	ns	ns
	Br	ns	ns	0.032	ns	ns	ns	ns

Table 2.7 Intraspecific differences of supraorbital trabecular bone morphometry. Intraspecific differences of trabecular bone descriptors between PO and BR subregions determined by Wilcoxon Sign test, where $p \leq 0.05$

Species	Location	BV/TV			DA			SMI		
		La	Mi	Me	La	Mi	Me	La	Mi	Me
Homo	**PO**	ns	ns	ns	0.012	0.012	0.012	ns	ns	0.036
Pan		ns	ns	0.043	ns	ns	ns	ns	0.043	0.043
Papio		ns	ns	ns	ns	ns	ns	ns	ns	ns
Cebus		ns	0.043	ns	0.028	0.043	ns	ns	0.043	ns

Table 2.8 Mean angle orientation of supraorbital primary eigenvectors. Mean angle orientations and standard deviations rounded to the nearest degree and Raleigh Test of significance p value of the primary eigenvector H2 from infero-superior, antero-posterior, and medio-lateral axes.

Species	Location	H2-Inferosuperior Axis			H2-Anteroposterior Axis			H2-Mediolateral Axis		
		Mean	S.D	Raleigh Test (p)	Mean	S.D	Raleigh Test (p)	Mean	S.D	Raleigh Test (p)
Homo	**PO**	28	21	0.005	89	36	0.202 ns	96	4	<0.001
	La	27	18	0.002	98	31	0.083 ns	95	7	<0.001
	Mi	22	21	0.005	96	28	0.037	91	10	<0.001
	Me	25	15	<0.001	89	26	0.022	86	13	<0.001
Pan	**PO**	14	10	0.002	95	16	0.016	93	7	0.002
	La	22	21	0.043	109	23	0.069 ns	93	10	0.002
	Mi	23	18	0.024	115	20	0.04	94	8	0.003
	Me	23	20	0.037	109	23	0.006	93	8	0.003
Papio	**PO**	44	24	0.131ns	130	43	0.673 ns	87	8	0.013
	La	52	33	0.366 ns	146	45	0.739ns	92	5	0.009
	Mi	61	26	0.17	156	35	0.43 ns	89	7	0.011
	Me	48	30	0.29 ns	136	51	0.854 ns	92	9	0.015
Cebus	**PO**	24	24	0.026	88	33	0.161 ns	89	8	<0.001
	La	52	33	0.17 ns	146	56	0.865 ns	86	10	<0.001
	Mi	56	12	0.006	7	44	0.66 ns	86	9	0.004
	Me	55	28	0.214 ns	111	39	0.561 ns	85	33	0.384 ns

Table 2.9 Mean angle orientation of supraorbital secondary eigenvectors. Mean angle orientations and standard deviations rounded to the nearest degree and Raleigh Test of significance p value of the secondary eigenvector H from infero-superior, antero-posterior, and medio-lateral axes. Watson Williams F test found a significant difference (p=0.021) of H3 angle from y in the middle ridge region only.

Species	Location	H3-Inferosuperior Axis			H3-Anteroposterior Axis			H3-Mediolateral Axis		
		Mean	S.D	Raleigh Test (p)	Mean	S.D	Raleigh Test (p)	Mean	S.D	Raleigh Test (p)
Homo	**PO**	91	36	0.195 ns	32	18	0.002	83	10	<0.001
	La	82	32	0.104 ns	28	19	0.003	85	9	<0.001
	Mi	85	28	0.042	22	22	0.007	88	10	<0.001
	Me	86	23	0.011	31	12	<0.001	87	23	0.01
Pan	**PO**	85	16	0.015	17	11	0.005	87	10	0.005
	La	71	23	0.068 ns	26	19	0.03	86	10	0.005
	Mi	64	20	0.039	31	16	0.016	87	10	0.001
	Me	71	21	0.049	24	19	0.029	86	9	0.004
Papio	**PO**	57	37	0.507 ns	45	21	0.096 ns	75	8	0.013
	La	45	38	0.542 ns	53	34	0.401ns	80	12	0.023
	Mi	25	34	0.411	61	26	0.178 ns	95	6	0.01
	Me	44	46	0.031	47	32	0.347 ns	91	6	0.01
Cebus	**PO**	93	33	0.147 ns	23	24	0.027	88	7	<0.001
	La	56	61	0.937 ns	50	31	0.12 ns	82	13	<0.001
	Mi	168	48	0.042	58	15	0.013	84	15	0.014
	Me	47	30	0.289 ns	44	21	0.085 ns	92	6	0.01

Table 2.10 Mean angle orientation of supraorbital tertiary eigenvectors. Mean angle orientations and standard deviations rounded to the nearest degree and Raleigh Test of significance p value of the tertiary eigenvector H1 from infero-superior, antero-posterior, and medio-lateral axes.

Species	Location	H1-Infero-superior Axis			H1 –Antero-posterior Axis			H1 –Medio-lateral Axis		
		Mean	S.D	Raleigh Test (p)	Mean	S.D	Raleigh Test (p)	Mean	S.D	Raleigh Test (p)
Homo	PO	85	4	<0.001	95	7	<0.001	10	3	<0.001
	La	90	7	<0.001	95	10	<0.001	12	5	<0.001
	Mi	92	10	<0.001	94	7	<0.001	12	5	<0.001
	Me	95	15	<0.001	94	18	0.002	18	17	<0.001
Pan	PO	85	6	0.002	91	9	0.004	11	5	0.002
	La	86	14	0.002	92	10	0.004	11	4	0.001
	Mi	86	4	0.008	92	11	0.005	12	4	0.001
	Me	87	9	0.004	91	8	0.003	11	4	0.002
Papio	PO	96	16	0.04	95	6	<0.001	18	7	0.011
	La	95	14	0.029	94	5	0.009	13	10	0.016
	Mi	89	8	0.013	92	4	0.008	9	3	0.008
	Me	85	6	0.01	95	4	0.008	10	2	0.007
Cebus	PO	90	9	0.002	90	5	<0.001	8	6	<0.001
	La	89	17	0.029	88	7	<0.001	15	10	<0.001
	Mi	84	13	0.008	93	12	0.007	14	12	0.007
	Me	99	20	0.004	79	20	0.074 ns	11	33	0.372 ns

Table 2.11 Mean angle orientation of supraorbital superoinferior eigenvectors. Mean angle orientations and standard deviations rounded to the nearest degree and Raleigh Test of significance p value of eigenvectors (grouped based on anatomical orientation, specifically nearness to the infero-superior anatomical axis) from infero-superior, antero-posterior, and medio-lateral axes. Watson Williams F test for multiple comparisons found no significant differences between like sites of the same species or different sites among species.

Species	Location	I-S Vector-I-S Axis			I-S Vector –A-P Axis			I-S Vector M-L Axis		
		Mean	S.D	Raleigh Test (p)	Mean	S.D	Raleigh Test (p)	Mean	S.D	Raleigh Test (p)
Homo	**PO**	16	20	0.004	82	23	0.01	93	7.3	<0.001
	La	16	20	0.003	88	24	0.012	94	7.129	<0.001
	Mi	17	12	<0.001	89	19	0.003	89	9.124	<0.001
	Me	24	15	<0.001	79	23	0.009	84	12.131	<0.001
Pan	**PO**	15	11	0.005	95	16	0.016	93	6.661	0.002
	La	17	7	0.002	94	17	0.021	95	3.487	0.001
	Mi	22	6	0.002	100	21	0.042	96	4.262	0.001
	Me	18	6	0.002	95	21	0.034	93	8.102	0.003
Papio	**PO**	27	7	0.012	73	18	0.058 ns	85	12.487	0.024
	La	22	7	0.012	89	17	0.053ns	87	14.613	0.034
	Mi	15	19	0.068ns	80	20	0.076ns	96	4.92	0.01
	Me	11	17	0.046	90	17	0.052 ns	98	4.448	0.009
Cebus	**PO**	9	19	0.006	82	17	0.003	85	6.968	<0.001
	La	17	24	0.025	90	23	0.019	82	13.002	<0.001
	Mi	-12	48	0.757ns	68	31	0.225ns	82	15.417	0.014
	Me	17	34	0.39ns	60	15	0.034	90	3.642	0.008

Table 2.12 Mean angle orientation of supraorbital anteroposterior eigenvectors. Mean angle orientations and standard deviations rounded to the nearest degree and Raleigh Test of significance p value of anatomically grouped eigenvectors; antero-posterior relative to infero-superior, antero-posterior, and medio-lateral axes.

Species	Location	A-P Vector-I-S Axis			A-P Vector –A-P Axis			A-P Vector –M-L Axis		
		Mean	S.D	Raleigh Test (p)	Mean	S.D	Raleigh Test (p)	Mean	S.D	Raleigh Test (p)
Homo	**PO**	81	23	0.009	21	17	0.001	86	10	<0.001
	La	75	19	0.003	18	21	0.005	86	10	<0.001
	Mi	78	16	<0.001	13	19	0.003	86	10	<0.001
	Me	87	23	0.009	25	24	0.013	90	23	0.01
Pan	**PO**	85	16	0.015	17	11	0.005	87	10	0.004
	La	76	10	0.004	12	18	0.026	84	10	0.001
	Mi	70	10	0.004	17	21	0.043	84	10	0.005
	Me	76	9	0.003	10	17	0.022	86	9	0.004
Papio	**PO**	78	19	0.067ns	179	28	0.225 ns	77	6	0.01
	La	82	15	0.037	6	18	0.06 ns	86	6	0.034
	Mi	72	11	0.019	178	23	0.122ns	88	6	0.01
	Me	74	6	0.01	11	15	0.038	85	5	0.009
Cebus	**PO**	82	17	0.003	10	17	0.003	92	6	<0.001
	La	82	21	0.01	5	18	0.029	86	10	<0.001
	Mi	43	27	0.128ns	47	35	0.344ns	87	7	0.003
	Me	75	21	0.089 ns	151	44	0.707ns	84	33	0.374ns

Table 2.13: Mean angle orientation of supraorbital mediolateral eigenvectors. Mean angle orientations and standard deviations rounded to the nearest degree and Raleigh Test of significance p value of anatomically grouped eigenvectors medio-lateral relative to infero-superior, antero-posterior, and medio-lateral axes.

Species	Location	M-L Vector-I-S Axis			M-L Vector –A-P Axis			M-L Vector –M-L Axis		
		Mean	S.D	Raleigh Test (p)	Mean	S.D	Raleigh Test (p)	Mean	S.D	Raleigh Test (p)
Homo	**PO**	85	4	<0.001	95	7	<0.001	10	3	<0.001
	La	90	7	<0.001	95	10	<0.001	12	5	<0.001
	Mi	92	10	<0.001	94	7	<0.001	12	5	<0.001
	Me	95	15	<0.001	94	18	0.002	18	16	<0.001
Pan	**PO**	85	6	0.002	91	9	0.004	11	5	0.002
	La	86	14	0.002	92	10	0.004	11	4	0.001
	Mi	86	4	0.008	92	11	0.005	12	4	0.001
	Me	87	9	0.004	91	8	0.003	11	4	0.002
Papio	**PO**	96	16	0.04	95	6	<0.001	18	7	0.011
	La	95	14	0.029	94	5	0.009	13	10	0.016
	Mi	89	8	0.013	92	4	0.008	9	3	0.008
	Me	88	9	0.01	95	4	0.008	10	2	0.007
Cebus	**PO**	90	9	0.002	90	5	<0.001	8	6	<0.001
	La	89	17	0.029	88	7	<0.001	15	10	<0.001
	Mi	84	13	0.008	93	12	0.007	14	12	0.007
	Me	99	20	0.004	79	20	0.074 ns	11	33	0.372 ns

Table 2.14 Trabecular bone morphometry across the post-cranial skeleton. Mean and standard deviations rounded to the nearest one hundredth from various µCT studies of trabecular bone morphology. * indicates that DA was determined using the star volume distribution method; all other DA values were determined by the Mean Intercept Length Method.

Species (*n*)		**BVF**	**DA**	**thickness**	**SMI**	**Study**
Homo sapiens n=10	Medial tibia	0.21 (0.03)	6.56 (3.94)	0.16 (0.02)	1.31 (0.23)	Ding et al., 2003
	Lateral tibia	0.17 (0.02)	3.82 (6.54)	0.13 (0.06)	1.56 (0.16)	
Papio sp. n=11	Humeral head	0.38 (0.06)	1.78 * (0.54)	0.16 (0.02)	NA	Ryan and Walker, 2010
	Femoral head	0.52 (0.07)	2.52* (1.04)	0.26 (0.09)	NA	
Pan n=18	Humeral head	0.41 (0.04)	1.59* (0.15)	0.17 (0.02)	NA	
	Femoral head	0.57 (0.07)	2.43* (0.76)	0.25 (0.06)	NA	
Ateles paniscus (n=1)	Humeral head	0.29	1.18	1.18	NA	Fajardo and Muller, 2001
	Femoral head	0.46	1.47	0.34	NA	
Papio Anubis (n=1)	Humeral head	0.35	1.28	0.17	NA	
	Femoral head	0.64	1.62	0.40	NA	
Pan n=6	T8	0.37 (0.01)	1.33 (0.04)	0.17 (0.01)	0.43 (0.13)	Cotter et al., 2009
Gorilla n=6		0.37 (0.03)	1.38 (0.04)	0.22 (0.02)	0.16 (0.28)	
Homo n=6		0.28 (0.02)	1.34 (0.07)	0.18 (0.01)	0.71 (0.11)	
Pongo n=6		0.32 (0.01)	1.36 (0.04)	0.21 (0.01)	0.72 (0.10)	
Hylobates n=6		0.39 (0.03)	1.46 (0.03)	0.15 (0.01)	-0.18 (0.36)	
Homo sapiens n=52	Iliac crest	0.16 (0.05)	1.49 (0.18)	0.15 (0.02)	1.15 (0.61)	Hildebrand et al. 1999
	L2	0.08 (0.02)	1.42 (0.16)	0.12 (0.01)	2.13 (0.35)	
	L4	0.09 (0.03)	1.51 (0.16)	0.14 (0.02)	2.12 (0.36)	
	Femoral head	0.26 (0.08)	1.68 (0.18)	0.19 (0.04)	0.41 (0.68)	
	Calcaneus	0.12 (0.04)	1.75 (0.15)	0.13 (0.01)	1.76 (0.36)	
C. jacchus n=5	Mandibular condyle	0.36 (0.07)	5.34 (1.27)	0.09 (0.01)	1.37 (0.48)	Ryan et al., 2010a
S. fuscicollis n=5		0.51 (0.07)	6.26 (1.33)	0.11 (0.03)	0.86 (0.48)	
S. sciureus n=5		0.40 (0.08)	10.29 (7.92)	0.11 (0.02)	0.75 (0.48)	
Homo sapiens n=11	9 condylar regions	0.17 (0.05)	1.51 (0.10)	0.10 (0.02)	NA	Giesen and van Eijden, 2000
Homo sapiens n=13	Dorsal MT1	0.42 (0.04)	6.9* (2.5)	NA	NA	Griffin et al., 2010b
	Plantar MT1	0.30 (0.04)	4.3* (2.5)	NA	NA	
Pan tryglodytes n=9	Dorsal MT1	0.50 (0.07)	3.6 (1.1)	NA	NA	
	Plantar MT1	0.46 (0.03)	2.3 (0.6)	NA	NA	
Pan paniscus n=8	Dorsal MT1	0.51 (0.06)	3.8 (1.2)	NA	NA	
	Plantar MT1	0.45 (0.07)	3.9 (1.2)	NA	NA	
Gorilla gorilla n=8	Dorsal MT1	0.44 (0.05)	4.1 (1.8)	NA	NA	
	Plantar MT1	0.41 (0.05)	3.5 (1.1)	NA	NA	

Table 3.1 Species, body mass, and trabecular VOI in the zygoma. Estimated body weight means and S.D. in kg and trabecular bone volumes in mm^3 are presented by species and number of sample for both male and female (157). "ua": values were unavailable

Species	N			Estimated Body Weight (kg)		Trabecular Upper Zygoma VOI volume (mm^3)		Trabecular Lower Zygoma VOI volume (mm^3)	
	m	fm		m	fm	m	fm	m	fm
Homo Sapiens	6	2	Mean	72.1	62.1	257	341	993	1657
			SD	11.4	9.88	191	151	625	427
Pan troglodytes	1	3	Mean	60	47.4	107	63		
			SD	ua	ua	-	36		
Pan paniscus		1	Mean	45.0	33.2	-	79		
			SD	8.4	4.2	-	-		

Table 3.2. Bone volume fraction, apparent density, and material density of the upper zygoma. Bone volume fraction (to the nearest hundredth), and apparent and material density (to the nearest mg) for whole bone (cortical + trabecular bone) upper zygomatic regions.

Species	Location	BVF		Apparent Density (mg HA/cm^3)		Material Density (mg HA/cm^3)	
		Mean	S.D.	Mean	S.D.	Mean	S.D.
Homo	**Upper Zygoma**	0.83	0.08	819	77	979	27
Pan	**Upper Zygoma**	0.93	0.04	898	69	966	47

Table 3.3 Trabecular bone morphometry of upper and lower zygoma regions. Mean and SD of trabecular bone descriptors rounded (to the nearest hundredth) determined by µCT trabecular bone analysis for upper and lower zygomatic regions in humans and the upper zygomatic region of *Pan*.

Species	Location	BVF		DA		Tb.N (mm^3)		Tb.Th (mm^3)		Tb.Sep (mm^3)		SMI		ConnD (mm^3)		Material Density (mg HA/cm^3)	
		Mean	S.D.	Mean	S.D.	Mean	S.D.	Mean	S.D.	Mean	S.D.	Mean	S.D.	Mean	S.D.	Mean	S.D.
Homo	**Lower**	0.30	0.10	1.87	0.37	1.46	0.34	0.28	0.06	0.72	0.19	1.25	1.03	4.86	1.83	842	40.2
	Upper	0.36	0.13	1.39	0.23	1.43	0.37	0.30	0.08	0.72	0.24	1.08	0.73	15.75	8.80	886	59.7
Pan	**Upper**	0.62	0.12	1.75	0.43	2.11	0.25	0.37	0.08	0.45	0.11	0.22	0.67	14.26	6.39	906	48.8

Table 3.4 Interspecific differences of trabecular bone morphometry between *Homo* and *Pan*. Interspecific significance of trabecular bone descriptors determined by Mann-Whitney U tests, where $p \leq 0.05$.

Species	Location	BVF	DA	SMI	ConnD (mm^3)	Tb.N (mm^3)	Tb.Thick (mm^3)	Tb.Sep (mm^3)	Material Density (mg HA/cm^3)
Homo vs Pan	**Upper Zygoma**	*0.005*	0.099	0.055	0.679	*0.005*	0.055	*0.013*	0.594

Table 3.5 Intraspecific differences of trabecular bone morphometry between zygomatic regions. Intraspecific differences of trabecular bone descriptors between PO and BR subregions determined by Wilcoxon Sign test, where $p \leq 0.05$.

Species	Location	BVF	DA	SMI	ConnD (mm^3)	Tb.N (mm^3)	Tb.Th (mm^3)	Tb.Sep (mm^3)	Material Density (mg HA/cm^3)
Homo	**Upper vs Lower**	0.14	*0.015*	0.77	*0.021*	0.77	0.374	0.95	*0.015*

Table 3.6 Mean angle orientation of zygomatic primary eigenvectors. Mean angle orientations and standard deviations rounded to the nearest degree and Raleigh Test of significance p value of the primary eigenvector H2 from infero-superior, antero-posterior, and medio-lateral axes ($p \leq 0.005$).

Species	Location	H2-Inferosuperior Axis			H2-Anteroposterior Axis			H2-Mediolateral Axis		
		Mean	S.D	*p*	Mean	S.D	*p*	Mean	S.D	*p*
Homo	**LZ**	92	11	<0.001	87	11	<0.001	0	16	<0.001
	UZ	51	35	0.081 ns	94	13	<0.001	134	61	0.89ns
Pan	**UZ**	72	14	0.01	154	41	0.56 ns	76	31	0.22ns

Table 3.7 Mean angle orientation of zygomatic secondary eigenvectors. Mean angle orientations and standard deviations rounded to the nearest degree and Raleigh Test of significance p value of the secondary eigenvector H3 from infero-superior, antero-posterior, and medio-lateral axes ($p \leq 0.005$).

Species	Location	H3-Inferosuperior Axis			H3-Anteroposterior Axis			H3-Mediolateral Axis		
		Mean	S.D	*p*	Mean	S.D	*p*	Mean	S.D	*p*
Homo	**LZ**	122	48	0.62 ns	139	38	0.274	89	10	<0.001
	UZ	106	29	0.018	101	50	0.585 ns	110	40	0.22 ns
Pan	**UZ**	99	9	0.003	88	33	0.29 ns	177	38	0.45 ns

Table 3.8 Mean angle orientation of zygomatic tertiary eigenvectors. Mean angle orientations and standard deviations rounded to the nearest degree and Raleigh Test of significance p value of the tertiary eigenvector H1 from infero-superior, antero-posterior, and medio-lateral axes ($p \leq 0.005$).

Species	**Location**	**H1-Inferosuperior Axis**			**H1-Anteroposterior Axis**			**H1-Mediolateral Axis**		
		Mean	**S.D**	***p***	**Mean**	**S.D**	***p***	**Mean**	**S.D**	***p***
Homo	**LZ**	36	38	0.263	64	42	0.39 ns	92	12	<0.001
	UZ	78	41	0.232ns	28	60	0.85 ns	90	23	0.001
Pan	**UZ**	21	5	0.002	89	18	0.026	99	7	0.002

Table 4.1 Mean BVF, and apparent and material density of cortical bone of the supraorbital and zygomatic regions. Bone Volume Fraction (BVF), Apparent and Material Density (measured in mg hydroxyapatite per mm^3 determined by high-resolution µCT scans.

Species	Location	BVF	Apparent Density	Material Density
Homo	**Supraorbit**	0.96	1002	1048
	Zygoma	0.94	976	1039
Pan	**Supraorbit**	0.89	887	979
	Zygoma	0.91	967	1046

Table 4.2 Mean osteocyte cell body shape and size. Osteocyte cell body surface area in μm^2; ellipsicity: oblate and prolate (to the nearest hundredth); sphericity (to the nearest hundredth); and volume in μm^3 means and standard deviations. *P* values determined by Mann-Whitney U tests showing interspecific significance of osteocyte cell bodies, where $p \leq 0.05$ is significant. *P* values determined by Mann-Whitney U tests showing intraspecific significance of osteocyte cell bodies, where $p \leq 0.05$ is significant.

Species	**Location**	**Surface Area**		**Oblate**		**Prolate**		**Sphericity**		**Volume**	
		Mean	**S.D.**	**Mean**	**S.D.**	**Mean**	**S.D.**	**Mean**	**S.D.**	**Mean**	**S.D.**
Homo	**Supraorbit**	572	192	0.32	0.15	0.38	0.17	0.60	0.07	613	293
	Zygoma	526	231	0.39	0.17	0.36	0.16	0.61	0.08	559	349
Pan	**Supraorbit**	507	184	0.39	0.17	0.43	0.18	0.64	0.09	549	251
	Zygoma	438	210	0.31	0.18	0.44	0.20	0.62	0.10	420	224
Homo vs Pan	**Supraorbit**	***0.015***		***0.005***		0.124		***0.001***		0.153	
	Zygoma	***0.005***		***0.000***		***0.006***		0.290		***0.010***	
Homo	**SO vs Z**	0.091		***0.0021***		0.216		0.313		0.099	
Pan	**SO vs Z**	***0.007***		***0.000***		0.755		0.277		***0.001***	

Table 4.3. Mean dendrite surface area, length, volume and diameter. Mean dendrite surface area (μm^2), length (µm), diameter (µm), volume **(**μm^2), and branching measured as an average of each cell. Interspecific significance of osteocyte dendrites determined by independent samples t-test, where $p \leq 0.05$. Intraspecific significance of osteocyte dendrites determined by independent samples t-test, where $p \leq 0.05$.

Species	Location	Mean Surface Area		Mean Length		Mean Diameter		Mean Volume		Mean Branching	
		Mean	S.D.	Mean	S.D.	Mean	S.D.	Mean	S.D.	Mean	S.D.
Homo	**Supraorbit**	19.7	9.4	5.9	1.6	1.2	0.37	7.0	5.8	17.2	9.3
	Zygoma	17.3	4.9	5.7	0.9	1.1	0.29	5.4	3.0	18.2	9.8
Pan	**Supraorbit**	16.1	3.2	5.7	1.1	1.0	0.12	4.1	1.2	17.1	8.4
	Zygoma	12.2	3.7	4.7	0.9	0.88	0.18	2.9	1.5	29.4	19.0
Homo vs Pan	**Supraorbit**	0.202		0.969		***0.003***		***0.029***		0.872	
	Zygoma	***0.000***		***0.000***		***0.000***		***0.000***		***0.000***	
Homo	**SO vs Z**	0.588		0.654		0.174		0.623		0.591	
Pan	**SO v Z**	***0.000***		***0.000***		***0.000***		***0.000***		***0.000***	